國立交通大學

電機與控制工程學系

碩士論文

實現感應電動車最大加速性能與最高效率之

控制設計與切換策略

The Control Design and Switching Strategy for Maximizing Acceleration and Efficiency of the Induction Machine on Electric Vehicles

研 究 生：郭志瀚

指導教授：徐保羅 博士

中 華 民 國 一 百 零 一 年 七 月

實現感應電動車最大加速性能與最高效率之控制設計與切換策略

The Control Design and Switching Strategy for Maximizing Acceleration and Efficiency of the Induction Machine on Electric Vehicles

研 究 生：郭志瀚　　Student : Chih-Han, Kuo

指導教授：徐保羅 博士　　Advisor : Dr. Pau-Lo Hsu

國立交通大學

電機與控制工程學系

碩士論文

A Thesis

Submitted to Institute of Electrical Control Engineering

College of Electrical and Computer Engineering

National Chiao Tung University

in Partial Fulfillment of the Requirements

for the Degree of Master

in

Electrical Control Engineering

July 2012

Hsinchu, Taiwan, Republic of China

中 華 民 國 一 百 零 一 年 七 月

實現感應電動車最大加速性能與最高效率之控制設計與切換策略

研究生: 郭志瀚　　指導教授: 徐保羅 博士

國立交通大學電控工程研究所

中文摘要

隨著近年來電動車技術以提高效率與扭力性能為目標發展，採用永磁馬達的高功率密度與高扭力密度的表現固然較佳，但感應馬達低成本、高耐用度與廣域操作速度的特性，為永磁馬達所不及之優勢；且在輕型電動車輛之應用上，更能突顯小功率感應馬達在高過負載能力的優勢。但欲達成感應馬達車用動力之高扭力與高效率的訴求，在控制技術上仍屬一大挑戰。因此，本研究致力於發展感應馬達之精密伺服控制，成功以德州儀器TMS320F28335 DSP晶片實現電動車兼具最大扭力與最高效率之自動切換控制策略。

在間接向量控制的實現中，為了達成磁場與扭力的動態控制，需進行感應馬達同步電氣角的估測，其計算乃建立在轉子時間常數(rotor time constant)的基礎上，此參數量測準確與否將影響控制的性能。有鑑於傳統轉子時間常數的量測方式實現困難，本研究發展以加速度為判斷依據的鑑別方法，不僅量測結果具有高準確度，且可直接在車輛上量測而更加容易實現；此外，為了達到單位電流最大扭力(maximum torque per amperage, MTPA)的控制特性，通常是將磁場電流(flux-producing current)與扭力電流(torque-producing current)設置於相同大小，但此方法在電動車的應用上造成了嚴重的磁飽和現象，使扭力輸出不如預期。本研究建立一套實驗標準程序，建立磁場操作電流與車輛加速度的關係，並選用額定激磁操作達成車輛的最大加速性能。

雖然MTPA擁有最大的加速表現，但在等速操作時效率較差。普遍的做法是在車輛加速過程後，藉由調整磁場電流達成效率的提升，但在電流切換時將造成車輛駕駛不平順的現象。本研究提出一套新式的切換控制策略，所定義之滑差因素(slip factor)將根據駕駛情況自動調整，在車輛低速時保有最大加速性能、在高速的情況則有最高的效率輸出，且實驗結果證明此方法在切換過程中具有更平順的電流操作；相較將磁場電流與扭力電流設為相同的方法，本控制策略在加速性、效率與車輛尾速部分可分別改善67%、273.6%與111.8%。因此，本研究成功實現了更適合電動車控制、且兼具高扭力效能及低耗電效率的感應馬達控制策略。

關鍵字: 電動車、感應馬達、最大扭力、效率、轉子時間常數、滑差因素。

The Control Design and Switching Strategy for Maximizing Acceleration and Efficiency of the Induction Machine on Electric Vehicles

Student: Chih-Han, Kuo Advisor: Dr. Pau-Lo, Hsu

Institute of Electrical Control Engineering
National Chiao Tung University

Abstract

As the environmental crises become more significant, electric vehicles have drawn more attentions and have been rapidly developed in recent years. Even though permenant magnetic motors (PM) are usually preferred due to their inherent characteritics of high torque and power density, induction motors (IM) behave better on the aspects of cost, reliability, and with a wider operational speed range. Particularly, IMs dominate PMs with higher overload capability on applications of low-powered electric vehicle. However, control techniques of IMs are still chanllenging to meet high-torque and high-efficiency vehicle performance. Therefore, this study is dedicated to developing a DSP-based precise servo control with maximizing torque and efficiency for the IM implemented on electric vehicles, and the developed automatic control strategy is successfully implemented on the TMS320F28335 DSP microcontroller.

The indirect vector control is commonly exploited for high performance servo control of the IM. To achieve control of the flux and torque, precise synchronous angle estimation based on the rotor time constant is crucial for stator current decoupling, and thus control performance is highly dependent on the accuracy of parameters. Due to the fact that conventional identification approaches are suffered from difficulty of implementation, an acceleration-based identification process which can be directly performed on the vehicle with satisfactory accuracy is developed in this thesis. In addition, the maximum torque per amperage (MTPA) operation is considerably important to provide desirable acceleration of the vehicle. It has been already recognized that by dividing the stator current equally into the flux-producing component and the torque-producing component, the MTPA can be thus obtained.

Nevertheless, such arrangement causes severe flux saturation and the desirable operation is usually lost. In this Thesis, a standard experimental process is developed to find proper setting of the flux-producing current so that the maximum acceleration can be fulfilled.

Despite of the maximum acceleration performance of the electric vehicle obtained by the MTPA operation, its operating efficiency is still comparatively low. In general, the efficiency can be improved by adjusting the flux-producing current. A novel switching control strategy where the defined slip factor can be automatically adjusted according to driving conditions is developed for achieving both the maximum acceleration and the highest efficiency, and experimental results show that it is more suitable to traction control of the electric vehicle because of its smooth operating performance. It has been also verified that all the acceleration, efficiency coefficient, and final vehicle speed can be improved by 67%, 273.6%, and 111.8%, respectively, when the system is fed by the maximum stator current compared with those of the conventional control approach by applying equal *d*-*q* current command.

Keywords: electric vehicle, induction motor, maximum torque per amperage, efficiency, rotor time constant identification, slip factor.

Acknowledgement

首先，我要由衷地感謝指導教授徐保羅老師在我這兩年研究生活的耐心指導與建議，不論在研究或為人處事上培養我嚴謹的邏輯、正確的態度與問題解決的能力，皆使我獲益良多，並順利地完成碩士學位。此外，感謝口試委員陳鴻祺老師與葉賜旭老師對於本論文寶貴的建議與指正，使本論文更加完善。

感謝在實驗室裡陪伴在我身邊的學長、同學與學弟們：博士班賴建良學長、黃煒生學長、謝鎮州學長與碩士班廖子期學長、葉釗甫學長、蔡政宏學長、林軒正學長、黃思翰學長平時給我的指導與幫助；信佑、振文、誌緯、晟傑、琮昇在學業上的討論與指教，以及一同度過研究所的時光，不論是研究上的切磋砥礪或生活上的經驗分享，都是我碩士班生活不可或缺的美好回憶；另外，也非常感謝實驗室助理慧霖，總是熱心地協助我們辦理各項事務，讓我們得以心無旁騖地進行研究。在此特別感謝振文與誌緯，在研究與實驗上大力地幫忙，獻上我最誠摯的感謝。

最後，我要感謝關心我的父母、妹妹以及女友題帆，長久以來在生活上的陪伴與支持，讓我在遭遇挫折與難關時能更有信心與動力去克服，而得以完成碩士學位。再次感謝求學歷程中所有幫助我、支持我與鼓勵我的師長與朋友，願將此喜悅與榮耀與你們一同分享。

Contents

List of Figures

List of Tables

Chapter 1

Introduction

1.1 Motivation and Purposes

As the environmental quality is severely deteriorated by air pollution emitted from urban transportation as well as crude oil of the earth will be soon exhausted, electric vehicles have become major solutions for these crises and have been rapidly developed in recent years [1]-[2]. Among all components, the propulsion systems including electric machines and drives, are keys to electric vehicle design [3, 8].

It has been widely investigated in literatures [4]-[7] to indicate that the most commonly used types of machines are direct current motors (DCMs), permenant magnetic motors (PMs), and induction motors (IMs). Comparisons of their performance are listed in Table 1-1 [5]. Desite of fast response and control simplicity, DCMs have drawbacks such as low efficiency, low reliability, and frequent requests of maintenance due to the presence of machanical commutators and brushes, and thus their applications for electric vehicle are limited. Thanks to the recent development of electronics and control technologies, it is increasingly practical to introduce PMs and IMs to replace DCMs in traction applications. In fact, they are more attractive and desirable with high reliability and maintenance-free operations, which are prime considerations for electric propulsion sysytems.

Table 1-1 Performance comparison of different motors [5]

	DCMs	IMs	PMs
Power density	◎◎	⊙	⊕⊕
Efficiency	◎	⊕	⊕⊕
Costs	⊕	⊕⊕	◎
Reliability	◎	⊕	⊙
Technical maturity	⊕	⊕	⊙

⊕⊕ : Excellent
⊕ : Good
⊙ : Neutral
◎ : Bad
◎◎ : Unsatisfactory

The merits of the PMs are mainly in the inherent characteristics of high torque and power density. However, they are suffered from a limited speed operation range, lower overload capacity, and higher cost. Magnet corrosion and demagnetization are also potential problems for these motors. On the other hand, IMs are robust and capable of a wide speed range operation with reasonable cost in spite of comparatively low efficiency. As far as the current circumstances of electric machine selections for electric vehicles are concerned, PMs are chiefly preferred for their high torque and power density while IMs are mostly applied to high-power traction application as shown in Fig. 1-1 [22]-[23]. Yet, as the production of rare-earth metals uesd for manufacturing of permenant magnets becomes less in the future, the importance of IMs will increase in traction applications [24]-[25]. Therefore, a 0.75-kW IM is selected to propel an experimental electric vehicle in this Thesis, and the design of the traction control implemented on the DSP microcontroller to drive the electric machine and vehicle will be studied.

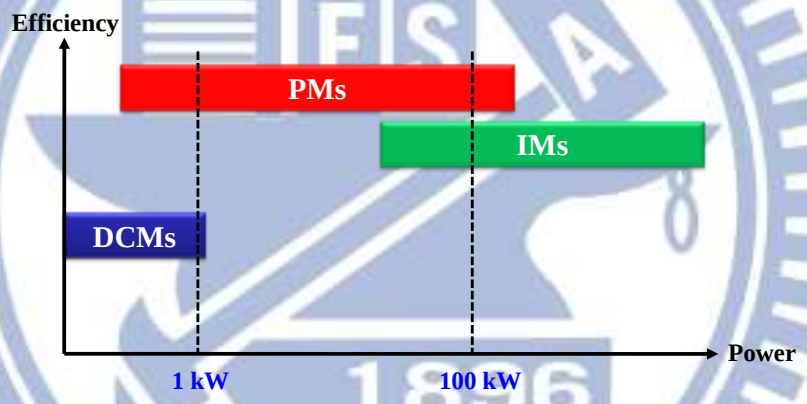

Fig. 1-1 Current circumstances of electric machine selections for electric vehicles [22]

The field-oriented control or vector control scheme, which can obtain high dynamic performance servo control of IMs, has become an industrial standard for electric vehicle traction control [9]. It employs coordinate trasformation according to the position of the rotor flux linkage in order to realize independent dynamic control of the flux and torque of the machine. Based on the approach accessing the flux angle or the synchronous angle, vector control can be classified as the direct method and the indirect method [10]-[11]. In the former one, Hall sensors or flux sensing coils should be applied for the measurement. However, installing sensors around the air-gap is not preferred owing to the noise, armature reaction, space limitation, etc. A more reasonable way to identify the flux angle is via electical equations with voltage and current measurements. Nevertheless, it is still not reliable since the integration involved in the computation is difficult to implement with the fact that DC offsets are

inevitably present in voltage and current signals, especially at low rotational speed of the machine.

The indirect method, on the other hand, obtains the flux angle by exploiting the slip frequency calculated from the IM dynamic model and the motor shaft speed measured from encoders or resolvers. Such a method has become dominant in commercialized IM drive systems because performance of the instantaneous torque control is reliable from the start-up to the maximum speed of the machine. However, it is still challenging with pure indirect vector control to fulfill main requirements of traction performance such as large output torque and high operating efficiency for IM control [4, 15].

Hence, it is strongly motivated in this study to design and implement a DSP-based precise servo control of an IM which can maximize torque and efficiency and obtain smooth driving operation for an electric vehicle, as illustrated in Fig. 1-2. With such work, we expect that IMs become much more competitive in low-power traction applications.

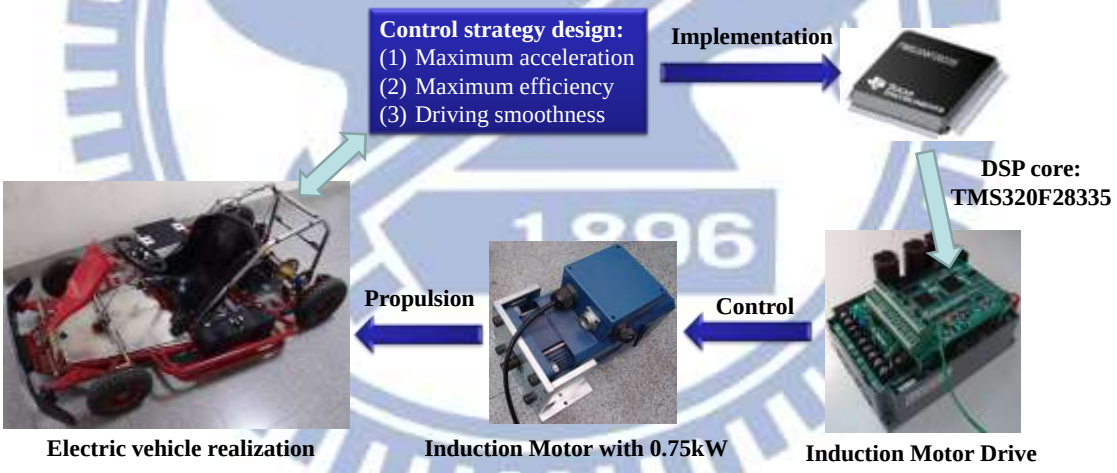

Fig. 1-2 Illustration of research in this Thesis

1.2 Problem Statements

1. The key parameter of the IM involved in the implementation of servo control scheme is unknown

   In order to obtain dynamic control of the flux and torque in the indirect vector control method, the rotor time constant is taken for the calculation of the slip frequency, on which the synchronous angle estimation is based. Thus, the decoupling of the stator current into flux and torque components is dependent on the rotor time constant [26]-[28]. Unfortunately, this parameter may not be accurately provided by the machine manufacturer. Without knowledge of the rotor time constant, the indirect vector control is unable to be implemented so that dynamic servo control of IM cannot be obtained.

2. Significant rolling resistance of the vehicle causes unsatisfactory acceleration

   Total weight of the system that includes the driver and the vehicle is approximately 145 kg, and it leads to the 0.75-kW IM overloaded during the start-up period. If it is not properly operated, the generated torque will not be sufficient to provide satisfactory acceleration. Particularly, when the vehicle is driven on an inclined road, it may fail to complete uphill climbing and thus get trapped on the way or even slide backwards. To overcome this problem, the maximum torque per amperage (MTPA) control is to be introduced.

3. Operating efficiency and vehicle speed are limited with the MTPA operation

   Although the torque can be maximally developed with the MTPA operation, it poses limitation on both operating efficiency and final speed of the vehicle due to strong excitation of the rotor flux linkage. When driven along a given route and distance, the vehicle with MTPA operation will consume more energy and take a longer time to complete the driving test.

4. Switching between operations results in uncomfortable driving experience

   A control strategy by which operations can be adjusted according to driving requirements is encouraged to obtain both the MTPA and high efficiency operations. It can be achieved by altering operating flux of IM. However, it may cause unsteady driving operations with abrupt changes of the vehicle speed. Such phenomenon is undesirable for the real vehicle driving.

1.3 Proposed Approaches

1. An acceleration-based identification process directly performed on the vehicle is developed to accurately obtain the rotor time constant

   In general, the rotor time constant can be identified by a traditional identification approach including the no-load and locked-rotor tests [12]. However, extra instruments are required for power measurement and rotor locking in the process, and it is too difficult to realize them directly on the vehicle. On the other hand, we develop an alternative approach based on the acceleration information to obtain the rotor time constant in this study. The proposed identification process benefits from reasonable accuracy and simplicity of implementation on the vehicle.

2. Rated flux excitation is adopted for providing the MTPA operation

   Basically, the MTPA operation indicates that the maximum torque can be produced at a given supplied stator phase current. It has been already recognized that by dividing the stator current equally into the flux-producing component and the torque-producing component, the MTPA operation can thus be obtained [13]. Yet, it is not suitable to the application in this study since severe flux saturation occurs and the desirable MTPA operation is lost. Another common suggestion is that the rotor flux linkage is excited at its rated level [10, 14]. The determination of the operating flux current corresponding to the rated rotor flux linkage is first derived based on the IM dynamic model. Then, a standard experimental process used for testing vehicle acceleration is established for the verification. Results show that the MTPA operation can be obtained by the rated flux excitation.

3. The standard experimental process testing efficiency is employed to find the highest efficieny (HE) operation

   By regulating the rotor flux linkage at an appropriate level, the highest operating efficiency of the IM can be obtained [16]-[17]. We utilize the developed experimental process to test efficiency with different settings of the flux current. It is verified from the experimental results that the HE operation can be obtained by operating the IM at a smaller flux level.

4. A smooth switching strategy based on the proposed slip factor adjustment (γ-adjustment) is designed to achieve both the MTPA and the HE operation

   As previously described, both operating efficiency and final speed of the

vehicle is limited with MTPA operation. Apparently, it is unfavorable to always be regulated at this operation for traction applications of IM. Firstly, we propose a novel control method by adjusting the defined slip factor γ, and both the MTPA as well as the HE operation can thus be obtained. Then, a switching strategy with which the MTPA operation is applied at a low speed for the maximum acceleration while the HE operation is applied to the high speed for improved operating efficiency and vehicle speed is designed based on the γ-adjustment. It has also been proved that the designed strategy can obtain smooth driving operations, and thus it is more suitable to traction control of electric vehicles.

1.4 Organization of the Thesis

The thesis is arranged as follows. Chapter 1 describes main purposes and goals of the research as well as general review of technical development. Research problems and their corresponding solutions are stated in this chapter as well; Chapter 2 examines relevant technical background, including modeling, analysis, and dynamic control of an induction machine. Then, the experimental system applied in the research is introduced; Chapter 3 presents the servo control of the induction machine used for the traction application. Rotor time constant identification, maximum torque per amperage control, and operating efficiency are involved in the investigation; Chapter 4 demonstrates an automatic switching strategy fulfilling both requirements of the maximum acceleration and the highest operating efficiency. Novel γ-adjustment control method developed for smooth driving performance is also described and verified in this chapter. Finally, achievements and contributions of the thesis are summarized in Chapter 5.

Chapter 2

Technical Background and System Structure

Although operating principles of an induction machine are similar to those of a transformer, its analysis and modeling become more complicated due to rotation of the secondary winding, i.e. the rotor of the machine. This is primarily because the inductances vary at different rotor position, and the electrical differential equations are time-varying as long as the rotor rotates. Theory of the reference frame transformation has been developed to transform the time-varing equations into the time-invariant ones to simplify the mathematical analysis of an induction motor. Then, high performance vector control was formulated for servo control of an induction motor based on its dynamic model. In this chapter, technical background with respect to modeling, analysis, and dynamic control of an induction machine will be introduced, followed by the system layout of the experimental electric vehicle driven with a single induction motor.

2.1 Transformation of Reference Frame

The illustration of a three-phase *a*-*b*-*c* axis, a stationary refernce frame *d*-*q* axis (superscripted as s), and a rotating reference frame *d*-*q* axis (superscripted as ω) with arbitraty speed, ω, is shown in Fig. 2-1.

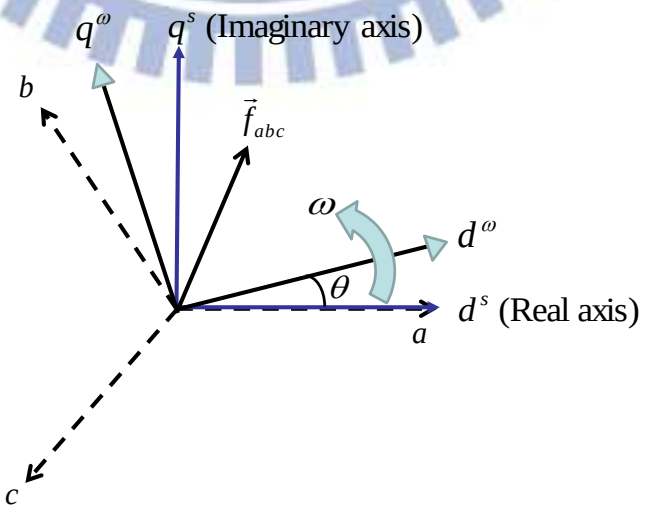

Fig. 2-1 Relationship between reference frames

An arbitrary space vector in the three-phase system can be defined as

$$\vec{f}_{abc} = \frac{2}{3}(f_{as} + f_{bs}e^{j2/3\pi} + f_{cs}e^{-j2/3\pi}) \tag{2-1}$$

Refered to the stationary reference frame, it can expressed as

$$\vec{f}_{dq}^{\,s} = f_{ds}^{s} + jf_{qs}^{s} = \vec{f}_{abc} \tag{2-2}$$

Thus, the transformation matrix converting a variable in the three-phase axis into the stationary frame can be derived as

$$\mathbf{C} = \frac{2}{3}\begin{bmatrix} 1 & \cos(-\frac{2}{3}\pi) & \cos\frac{2}{3}\pi \\ 0 & -\sin(-\frac{2}{3}\pi) & -\sin\frac{2}{3}\pi \end{bmatrix} = \frac{2}{3}\begin{bmatrix} 1 & -\frac{1}{2} & -\frac{1}{2} \\ 0 & \frac{\sqrt{3}}{2} & -\frac{\sqrt{3}}{2} \end{bmatrix} \tag{2-3}$$

such that

$$\begin{bmatrix} f_{ds}^{s} \\ f_{qs}^{s} \end{bmatrix} = \mathbf{C}\begin{bmatrix} f_{as} \\ f_{bs} \\ f_{cs} \end{bmatrix} \tag{2-4}$$

Since the instantaneous angle between the *d* axis of the rotating reference frame and the stationary real axis is θ as illustrated in Fig. 2-1, the variable in the equation (2-1) can be further referred to the rotating reference frame as

$$\vec{f}_{dq}^{\,\omega} = f_{ds}^{\omega} + jf_{qs}^{\omega} = \vec{f}_{dq}^{\,s}e^{-j\theta} \tag{2-5}$$

Then, the relationship of its components expressed in these two reference frames are given by

$$\begin{bmatrix} f_{ds}^{\omega} \\ f_{qs}^{\omega} \end{bmatrix} = \mathbf{P}\begin{bmatrix} f_{ds}^{\omega} \\ f_{qs}^{\omega} \end{bmatrix} \tag{2-6}$$

where **P** is the transformation matrix, which can be represented as

$$\mathbf{P} = \begin{bmatrix} \cos\theta & \sin\theta \\ -\sin\theta & \cos\theta \end{bmatrix} \tag{2-7}$$

2.2 Dynamic Characersitics of an Induction Machine

Three-phase axis of the stator (*as-bs-cs*) and rotor (*ar-br-cr*) of an induction motor is shown in Fig. 2-2. The *ar-br-cr* axis rotates with electrical speed, ω_r, as mechanical rotation speed is ω_m of the rotor shaft. If the number of magnetic poles of

the machine is P, the relationship between the mechanical speed and the electrical speed is given by

$$\omega_r = \frac{P}{2}\omega_m \tag{2-8}$$

as derived from

$$\theta_r = \frac{P}{2}\theta_m \tag{2-9}$$

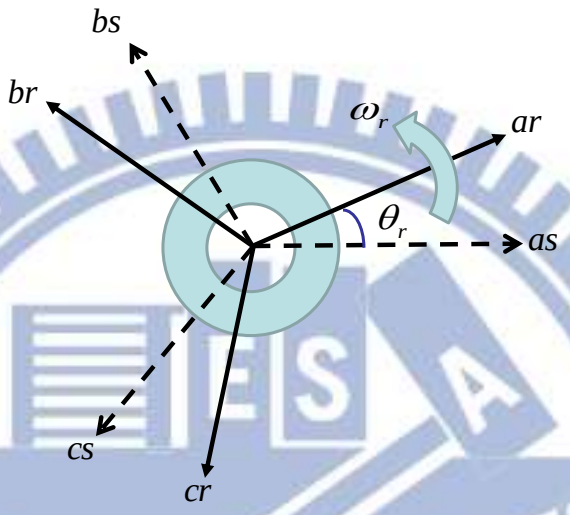

Fig. 2-2 Three-phase axis of the stator and rotor

Therefore, the stator and rotor electical equations can be written in vector form as

$$\mathbf{V}_{abcs} = R_s\mathbf{I}_{abcs} + p\boldsymbol{\lambda}_{abcs} \tag{2-10}$$

$$\mathbf{V}_{abcr} = R_r\mathbf{I}_{abcr} + p\boldsymbol{\lambda}_{abcr} \tag{2-11}$$

where p stands for a differential operator, R_s is the stator winding resistance, R_r is the rotor winding resistance referred to the stator side, and each vector term is given by

$$\mathbf{V}_{abcs} = \begin{bmatrix} V_{as} & V_{bs} & V_{cs} \end{bmatrix}^T \tag{2-12}$$

$$\mathbf{I}_{abcs} = \begin{bmatrix} i_{as} & i_{bs} & i_{cs} \end{bmatrix}^T \tag{2-13}$$

$$\boldsymbol{\lambda}_{abcs} = \begin{bmatrix} \lambda_{as} & \lambda_{bs} & \lambda_{cs} \end{bmatrix}^T \tag{2-14}$$

$$\mathbf{V}_{abcr} = \begin{bmatrix} V_{ar} & V_{br} & V_{cr} \end{bmatrix}^T \tag{2-15}$$

$$\mathbf{I}_{abcr} = \begin{bmatrix} i_{ar} & i_{br} & i_{cr} \end{bmatrix}^T \tag{2-16}$$

$$\boldsymbol{\lambda}_{abcr} = \begin{bmatrix} \lambda_{ar} & \lambda_{br} & \lambda_{cr} \end{bmatrix}^T \tag{2-17}$$

The flux linkages for the stator and rotor can be expressed as

$$\begin{bmatrix} \boldsymbol{\lambda}_{abcs} \\ \boldsymbol{\lambda}_{abcr} \end{bmatrix} = \begin{bmatrix} \mathbf{L}_s & \mathbf{L}_{sr} \\ \mathbf{L}_{sr}^T & \mathbf{L}_r \end{bmatrix} \begin{bmatrix} \mathbf{I}_{abcs} \\ \mathbf{I}_{abcr} \end{bmatrix} \tag{2-18}$$

where

$$\mathbf{L}_s = \begin{bmatrix} L_{ls}+L_{ms} & -\frac{1}{2}L_{ms} & -\frac{1}{2}L_{ms} \\ -\frac{1}{2}L_{ms} & L_{ls}+L_{ms} & -\frac{1}{2}L_{ms} \\ -\frac{1}{2}L_{ms} & -\frac{1}{2}L_{ms} & L_{ls}+L_{ms} \end{bmatrix} \tag{2-19}$$

$$\mathbf{L}_r = \begin{bmatrix} L_{lr}+L_{mr} & -\frac{1}{2}L_{mr} & -\frac{1}{2}L_{mr} \\ -\frac{1}{2}L_{mr} & L_{lr}+L_{mr} & -\frac{1}{2}L_{mr} \\ -\frac{1}{2}L_{mr} & -\frac{1}{2}L_{mr} & L_{lr}+L_{mr} \end{bmatrix} \tag{2-20}$$

$$\mathbf{L}_{sr} = L_{sr} \begin{bmatrix} \cos\theta_r & \cos(\theta_r+\frac{2\pi}{3}) & \cos(\theta_r-\frac{2\pi}{3}) \\ \cos(\theta_r-\frac{2\pi}{3}) & \cos\theta_r & \cos(\theta_r+\frac{2\pi}{3}) \\ \cos(\theta_r+\frac{2\pi}{3}) & \cos(\theta_r-\frac{2\pi}{3}) & \cos\theta_r \end{bmatrix} \tag{2-21}$$

In the equation (2-19) ~ (2-21), L_{ls} is the leakage inductance of the stator winding, L_{lr} stands for the leakage inductance of the rotor winding, and L_{ms} and L_{mr} is the mutual inductance of the stator and the rotor, respectively. L_{sr} means the mutual inductance between the *a*-phase stator winding and the *a*-phase rotor winding when θ_r is zero. As seen from (2-10) ~ (2-21), the equations describing the dynamic characteritics of the induction motor are time-varying. Obviously, it is considerably difficult to solve such sophisticated differential equations analytically. However, if the coordinate transformation by which the three-phase variables are transformed into *d-q* variables as described in Section 2.1, electrical equations with time-invariant form can be obtained, and thus the induction machine becomes simple to analyze. The deduction from time-varying equations to time-invariant ones in detail is described in [10].

The *d-q* stator and rotor voltage equations at reference frame with arbitrary rotational speed can be expressed as

$$V_{ds}^{\omega} = R_s i_{ds}^{\omega} + p\lambda_{ds}^{\omega} - \omega\lambda_{qs}^{\omega} \tag{2-22}$$

$$V_{qs}^{\omega} = R_s i_{qs}^{\omega} + p\lambda_{qs}^{\omega} + \omega\lambda_{ds}^{\omega} \tag{2-23}$$

$$V_{dr}^{\omega} = R_r i_{dr}^{\omega} + p\lambda_{dr}^{\omega} - (\omega - \omega_r)\lambda_{qr}^{\omega} \tag{2-24}$$

$$V_{qr}^{\omega} = R_r i_{qr}^{\omega} + p\lambda_{qr}^{\omega} + (\omega - \omega_r)\lambda_{dr}^{\omega} \tag{2-25}$$

where the electrical speed of the rotor's rotation is ω_r. Particularly, the rotor voltage is zero in the case of squirrel-cage induction motor, i.e. singly-fed induction motor, since the rotor is short-circuited by the end ring. As a consequence, (2-24) and (2-25) become

$$0 = R_r i_{dr}^{\omega} + p\lambda_{dr}^{\omega} - (\omega - \omega_r)\lambda_{qr}^{\omega} \tag{2-26}$$

$$0 = R_r i_{qr}^{\omega} + p\lambda_{qr}^{\omega} + (\omega - \omega_r)\lambda_{dr}^{\omega} \tag{2-27}$$

The flux linkage of the stator and rotor can also be represented in terms of *d-q* variables as

$$\lambda_{ds}^{\omega} = L_s i_{ds}^{\omega} + L_m i_{dr}^{\omega} \tag{2-28}$$

$$\lambda_{qs}^{\omega} = L_s i_{qs}^{\omega} + L_m i_{qr}^{\omega} \tag{2-29}$$

$$\lambda_{dr}^{\omega} = L_m i_{ds}^{\omega} + L_r i_{dr}^{\omega} \tag{2-30}$$

$$\lambda_{qr}^{\omega} = L_m i_{qs}^{\omega} + L_r i_{qr}^{\omega} \tag{2-31}$$

where $L_m = \frac{3}{2} L_{ms}$, $L_s = L_m + L_{ls}$, $L_r = L_m + L_{lr}$. Finally, the electromagnetic torque can be represented as

$$T_e = \frac{3}{2}\frac{P}{2}\frac{L_m}{L_r}(\lambda_{dr}^{\omega} i_{qs}^{\omega} - \lambda_{qr}^{\omega} i_{ds}^{\omega}) \tag{2-32}$$

Based on the equation (2-22)-(2-31), the equivalent circuit of the squirrel-cage induction machine at an arbitrary speed rotating *d-q* reference frame can be depicted as Fig. 2-3.

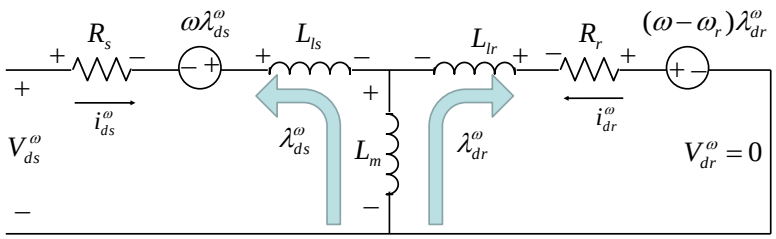

(a) *d*-axis

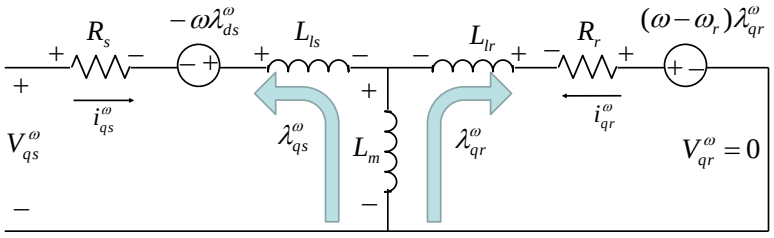

(b) *q*-axis

Fig. 2-3 Equivalent circuit of the squirrel-cage induction motor

2.3 Indirect Vector Control

2.3.1 Principles of indirect vector control

The electrical equations at the synchronously rotating *d-q* reference frame can be derived by subsituting $\omega = \omega_e$ in (2-22), (2-23), (2-26), and (2-27), and all the superscipts, ω, in the equations are omitted for expression at the synchronous reference frame. Then, the dynamic charateristics at the synchronous reference frame can be expressed as

$$V_{ds} = R_s i_{ds} + p\lambda_{ds} - \omega_e \lambda_{qs} \tag{2-33}$$

$$V_{qs} = R_s i_{qs} + p\lambda_{qs} + \omega_e \lambda_{ds} \tag{2-34}$$

$$0 = R_r i_{dr} + p\lambda_{dr} - (\omega_e - \omega_r)\lambda_{qr} \tag{2-35}$$

$$0 = R_r i_{qr} + p\lambda_{qr} + (\omega_e - \omega_r)\lambda_{dr} \tag{2-36}$$

where the flux linkage terms are given by

$$\lambda_{ds} = L_s i_{ds} + L_m i_{dr} \tag{2-37}$$

$$\lambda_{qs} = L_s i_{qs} + L_m i_{qr} \tag{2-38}$$

$$\lambda_{dr} = L_m i_{ds} + L_r i_{dr} \tag{2-39}$$

$$\lambda_{qr} = L_m i_{qs} + L_r i_{qr} \tag{2-40}$$

Indirect vector control is performed based on the assumption that the rotor flux linkage only exists on the *d* axis. In other words,

$$\lambda_{qr}^{e} = 0 = p\lambda_{qr}^{e} \tag{2-41}$$

By substituting (2-41) into (2-35), (2-36), and (2-40), we can obtain the following equations respectively.

$$i_{dr} = -\frac{p\lambda_{dr}}{R_r} \tag{2-42}$$

$$\omega_{slip} \equiv \omega_e - \omega_r = -\frac{R_r i_{qr}}{\lambda_{dr}} \tag{2-43}$$

$$i_{qr} = -\frac{L_m}{L_r} i_{qs} \tag{2-44}$$

The rotor flux linkage in s-domain can be derived by substituting (2-42) into (2-39) with Laplace transform as

$$\lambda_{dr} = \frac{L_m i_{ds}}{1+\tau_r s} \tag{2-45}$$

where $\tau_r = L_r / R_r$ denotes the rotor time constant. Then, we subsitute (2-44) and (2-45) into (2-43), the slip angular frequency can be expressed in terms of the *d*-axis current and the *q*-axis current as

$$\omega_{slip} = \frac{1+\tau_r s}{\tau_r} \frac{i_{qs}}{i_{ds}} \tag{2-46}$$

Finally, the electromagnetic torque can be simplified with the absent *q*-axis rotor flux linkage as

$$T_e = \frac{3}{2}\frac{P}{2}\frac{L_m}{L_r}\lambda_{dr} i_{qs} \tag{2-47}$$

Hence, the torque is directly proportional to the *q*-axis current under the condition that the rotor flux linkage is constant. Furthermore, the rotor flux linkage is excited solely by the *d*-axis current as seen from (2-45). Therefore, the *d*-axis current is also named as the flux-producing current and the *q*-axis current is called the torque-producing current. Obviously, the behavior of the indiect vector-controlled induction motor is quite similar to that of a separately excited DC machine, and thus the dynamic response of the induction machine can be controlled.

2.3.2 Implementation of indirect vector control

In order to implement the described control process, the knowledge of angular position of the rotor flux linkage is essential since the *d* axis is supposed to be aligned with it so that the stator phase current can be divided into the flux-producing and torque-producing components as illustrated in Fig. 2-4. The angular position of the rotor flux, i.e. the synchronous angle, can be estimated indirectly by integrating the

calculated electrical angular frequency as

$$\hat{\theta}_e = \int_0^t \hat{\omega}_e d\tau = \int_0^t (\hat{\omega}_r + \hat{\omega}_{slip}) d\tau \tag{2-48}$$

Obviously, the slip frequency is involved and summed with the angular rotor shaft speed in electrical angle, $\hat{\omega}_r$. Thus, the rotor time constant of the machine must be known, and the performance is highly dependent on this parameter. The control block diagram of indirect vector control of an induction motor is shown in Fig. 2-5.

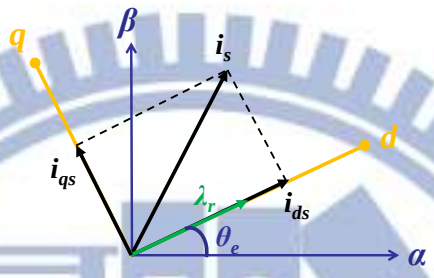

Fig. 2-4 Illustration of stator current decoupling

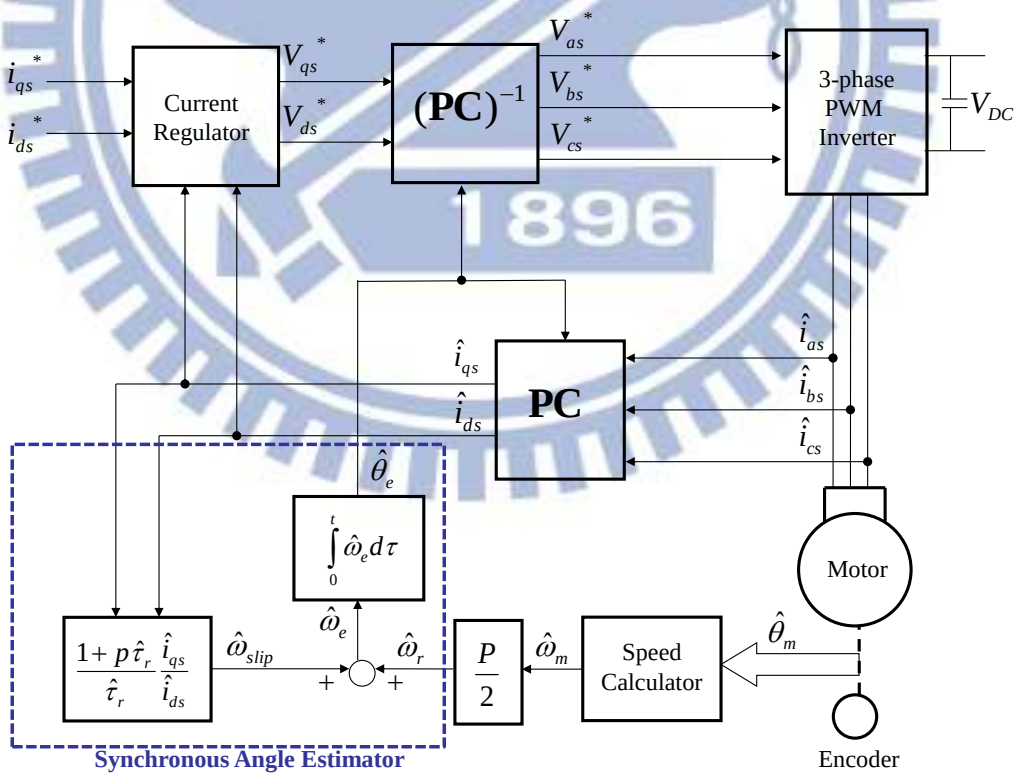

Fig. 2-5 Block diagram of indirect vector control

As seen from Fig. 2-5, a current-regulated pulse width modulation (PWM) inverter is applied to control the *d-q* components current of the motor. In particular, the block with the notation **PC** is the coordinate transformation from the three-phase system to the synchronous reference frame, employing the transformation matrix which is the multiplication of **P** and **C** as presented in (2-3) and (2-7). On the other hand, the block with the notation $(\mathbf{PC})^{-1}$ indicates the inverse coordinate transformation transforming the variables in the synchronous reference frame back to those in the three-phase coordinate. Finally, the synchronous angle estimator, which is composed of the slip frequency estimation and the integration of the synchronously rotating speed, is responsible for providing the synchronous angle for the coordinate transformation.

2.3.3 Dynamic model of an indirect vector-controlled induction motor

The *d-q* stator voltage can be expressed in terms of the stator current and rotor flux linkage based on the rotor flux linkage orientation of the vector control as

$$V_{ds} = R_s i_{ds} + \sigma L_s \frac{di_{ds}}{dt} + \frac{L_m}{L_r}\frac{d\lambda_{dr}}{dt} - \omega_e \sigma L_s i_{qs} \tag{2-49}$$

$$V_{qs} = R_s i_{qs} + \sigma L_s \frac{di_{qs}}{dt} + \frac{L_m}{L_r}\omega_e \lambda_{dr} + \omega_e \sigma L_s i_{ds} \tag{2-50}$$

where $\sigma = 1 - \frac{L_m^2}{L_s L_r}$ stands for the total leakage factor. In (2-50), the terms

$$\frac{L_m}{L_r}\omega_e \lambda_{dr} + \omega_e \sigma L_s i_{ds} = \omega_e (\frac{L_m}{L_r}\lambda_{dr} + \sigma L_s i_{ds}) \tag{2-51}$$

$$= \omega_e (\frac{L_m}{L_r}\lambda_{dr} + \sigma L_s \frac{\lambda_{dr}}{L_m}) \tag{2-52}$$

$$= \omega_e (\frac{L_s}{L_m})\lambda_{dr}$$

$$= (\frac{P}{2}\omega_m + \omega_{slip})(\frac{L_s}{L_m})\lambda_{dr}$$

$$= \frac{P}{2}\omega_m (\frac{L_s}{L_m})\lambda_{dr} + \omega_{slip}(\frac{L_s}{L_m})\lambda_{dr} \tag{2-53}$$

If the variation of the flux linkage is sufficiently slow compared with the rotor time constant, it can be obtained by substituting p=0 in (2-45) as

$$\lambda_{dr} = L_m i_{ds} \tag{2-54}$$

for deriving (2-52) from (2-51). Similarly, the slip frequency can be written as

$$\omega_{slip} = \frac{1}{\tau_r}\frac{i_{qs}}{i_{ds}} \tag{2-55}$$

Therefore, the equation (2-56) can be derived by substituting (2-55) into (2-53) as

$$\frac{L_m}{L_r}\omega_e\lambda_{dr} + \omega_e\sigma L_s i_{ds} = \frac{P}{2}\frac{L_s}{L_m}\omega_m\lambda_{dr} + \frac{L_s}{L_r}R_r i_{qs} \tag{2-56}$$

Substitute (2-56) into (2-50) and take the Laplace transform on the both side of the equal sign, and we can derive

$$\begin{aligned} i_{qs} &= \frac{1}{\sigma L_s s + R_s}(V_{qs} - \frac{L_m}{L_r}\omega_e\lambda_{dr} - \omega_e\sigma L_s i_{ds}) \\ &= \frac{1}{\sigma L_s s + R_s}(V_{qs} - \frac{P}{2}\frac{L_s}{L_m}\omega_m\lambda_{dr} - \frac{L_s}{L_r}R_r i_{qs}) \\ &= \frac{1}{\sigma L_s s + (R_s + \frac{L_s}{L_r}R_r)}(V_{qs} - \frac{P}{2}\frac{L_s}{L_m}\omega_m\lambda_{dr}) \end{aligned} \tag{2-57}$$

where the term $\frac{P}{2}\frac{L_s}{L_m}\omega_m\lambda_{dr}$ indicates the back electromagnetic force (back-emf), V_b.

In general, the machanical dynamics of an induction motor can be expressed as

$$T_e - T_L = J\frac{d\omega_m}{dt} + B\omega_m \tag{2-58}$$

where T_L is the applied mechanical load, J stands for the inertia, and B indicates the viscous friction coefficient. Thus, based on (2-47), (2-57), and (2-58) the dynamic model of the indirect vector-controlled induction motor can be depicted as Fig. 2-6.

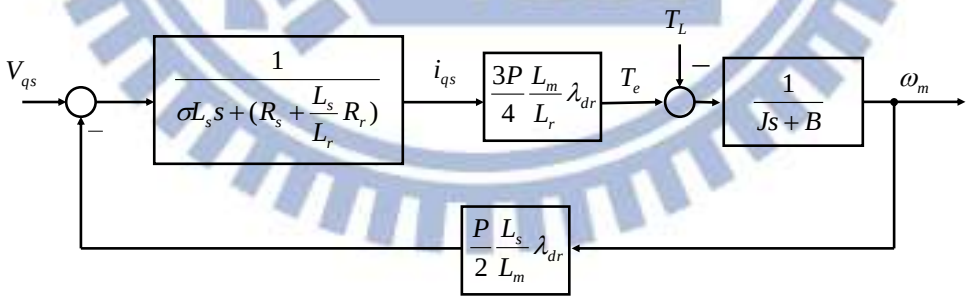

Fig. 2-6 Dynamic model of the indirect vector-controlled induction motor

The torque and back-emf constant of the induction motor can be defined as K_t and K_e, respectively, such that

$$T_e = K_t i_{qs}, K_t = \frac{3P}{4}\frac{L_m}{L_r}\lambda_{dr} \tag{2-59}$$

$$V_b = K_e\omega_m, K_e = \frac{P}{2}\frac{L_s}{L_m}\lambda_{dr} \tag{2-60}$$

Consequently, performance of the induction machine is determined by the condition of the rotor flux linkage. It is also the major concern of this study and it will be discussed and verified in detail in next chapter.

2.4 Operation Region of an Induction Machine

2.4.1 Voltage and current constraints on induction machine control

Due to components and input voltage of the power inverter, the electric power delivering to the machine is limited by the voltage and current ratings. Even though the inverter has sufficiently large ratings, the machine itself has constraints owing to insulation and thermal limit. In control of the induction machine, both the voltage and current constraints must be considered.

The maximum phase voltage of the motor, V_{smax}, is determined by the DC-bus voltage of the inverter while the maximum current flowing into the machine, I_{smax}, is limited by the thermal rating of the inverter or the machine itself. Thus, the following two constraints must be hold:

$$V_{ds}^2 + V_{qs}^2 = V_s^2 \le V_{\text{smax}} \tag{2-61}$$

$$i_{ds}^2 + i_{qs}^2 = i_s^2 \le I_{\text{smax}} \tag{2-62}$$

The equations (2-49) and (2-50) can be simplified as (2-61) and (2-62) under the steady-state operation.

$$V_{ds} = R_s i_{ds} - \omega_e \sigma L_s i_{qs} \tag{2-63}$$

$$V_{qs} = R_s i_{qs} + \omega_e L_s i_{ds} \tag{2-64}$$

A further simplification can be obtained by neglecting the voltage drop over the stator resistance as

$$V_{ds} \approx -\omega_e \sigma L_s i_{qs} \tag{2-65}$$

$$V_{qs} \approx \omega_e L_s i_{ds} \tag{2-66}$$

By substituting (2-63) and (2-64) into the voltage constraint shown in (2-61), an ineqality representing an ellipse in the synchronous reference current plane can be obtained as follows.

$$\frac{i_{ds}^2}{(\frac{V_{s\max}}{\omega_e L_s})^2}+\frac{i_{qs}^2}{(\frac{V_{s\max}}{\omega_e \sigma L_s})^2}\le 1 \tag{2-67}$$

Since σ is typically equal to 0.1, the major axis lies on the i_{qs}-axis while the minor axis lies on the i_{ds}-axis. Fig. 2-7 illustrates ellipses of the voltage constraint at different operation speed.

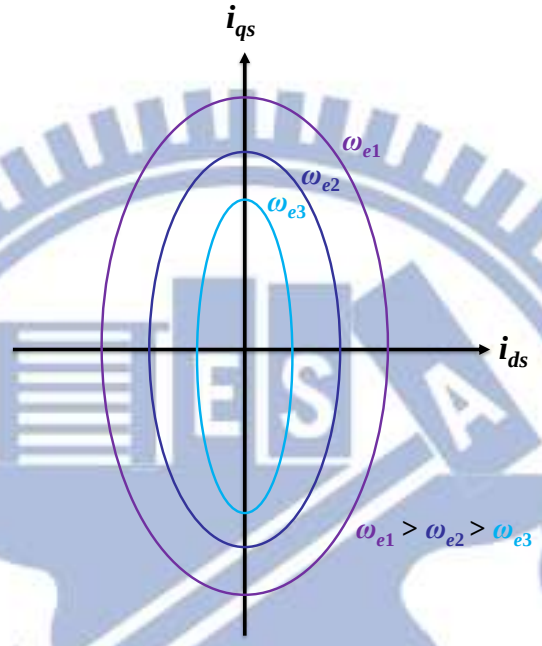

Fig. 2-7 Voltage constraint ellipses at different operation speed

Similarly, we can depict a current constriant circle in the current plane with a radius equal to the maximum current based on (2-62) as shown in Fig. 2-8.

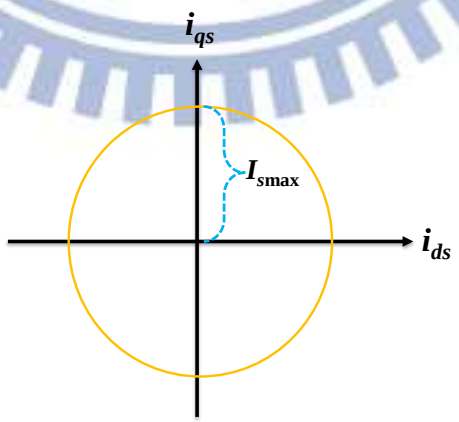

Fig. 2-8 Circle of current constraint

The torque shown in (2-47) can be derived as

$$T_e = \frac{3}{2}\frac{P}{2}\frac{L_m^2}{L_r} i_{ds} i_{qs} \tag{2-68}$$

Hence, the developed torque of the induction machine can also be plotted in the current plane and it appears as a parabolic curve. The illustration is shown in Fig. 2-9.

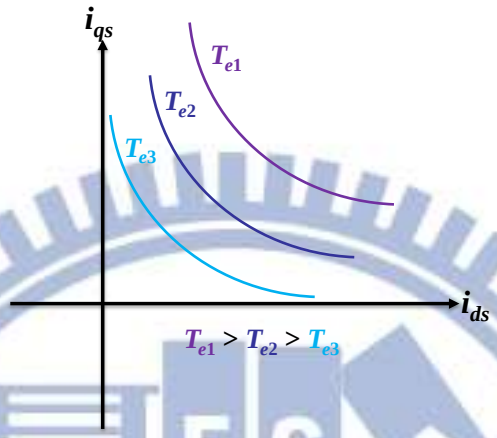

Fig. 2-9 Parabolic curves of torque

Because (2-62) and (2-67) must be simultaneously satisfied, possible operating point lies in the cross secrion of the voltage constraint ellipse and the current constraint circle, as the shaded area shown in Fig. 2-10. The torque at a specific operation point is determined by the product of the *d*-axis and *q*-axis components current.

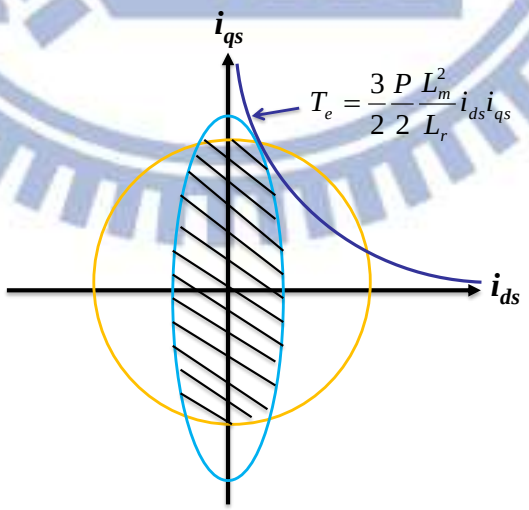

Fig. 2-10 Possible operation points considering both voltage and current constraint

2.4.2 Capability curve of an induction machine

The operation region of an induction machine can be basically categorized into three regions. The first region, indicating the frequency from zero to the base frequency, is called the constant torque region. In this region, the maximum torque is limited by the maximum stator current, which is determined by I_{smax}. At the base frequency, the terminal voltage of the motor reaches the voltage limit.

As the frequecy continues to increase, the voltage ellipse will shrink and the second region is obtained. Thus, the stator current vector moves along the current constraint circle from A to C as shown in Fig. 2-11. The torque in this region is inversely proportional to the speed and the output power of the motor, given by $P_m = T_e \cdot \omega_m$, is maintained as a constant. Hence, the second region is also called as the constant power region.

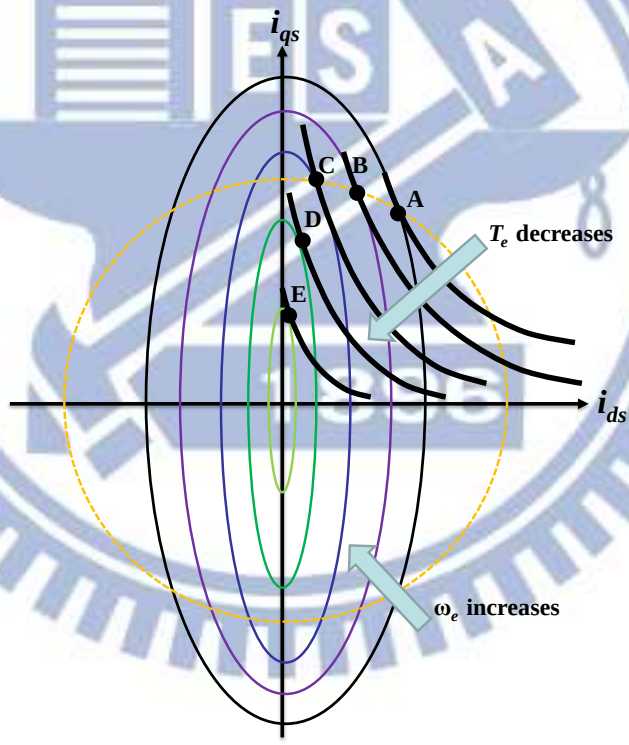

Fig. 2-11 Locus of voltage ellipse, current circle, and torque in different operation regions

If the operating frequency further increases above point C, the volatge ellipse will shrink inside the current limit circle to enter the third region, and there is no crossing point between the ellipse and the circle as E and F shown in Fig. 2-11. In this case, the operation is completely limited by the voltage constriant. Since the current

also decreases as the frequency increases, the torque decreases inversely proportional to the square of ω_e. This region is called as the characteritic region of the induction motor.

The torque, stator volatge, and stator current can be plotted versus the electrical frequency to specify these three operation region as shown in Fig. 2-12. The curve is also known as the capability curve or the characteristic curve of the induction machine.

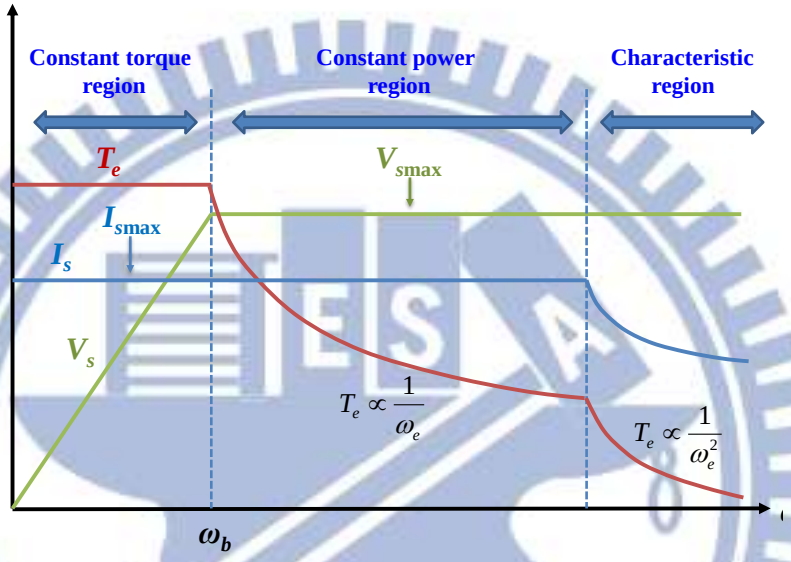

Fig. 2-12 Capability Curve of an induction motor

2.5 System Structure

2.5.1 Mechanical layout of the electric vehicle

The overall mechanical scheme of the electric vehicle adopted in this study is shown in Fig. 2-13. The components corresponding to the number marked in Fig. 2-13 are described as below.

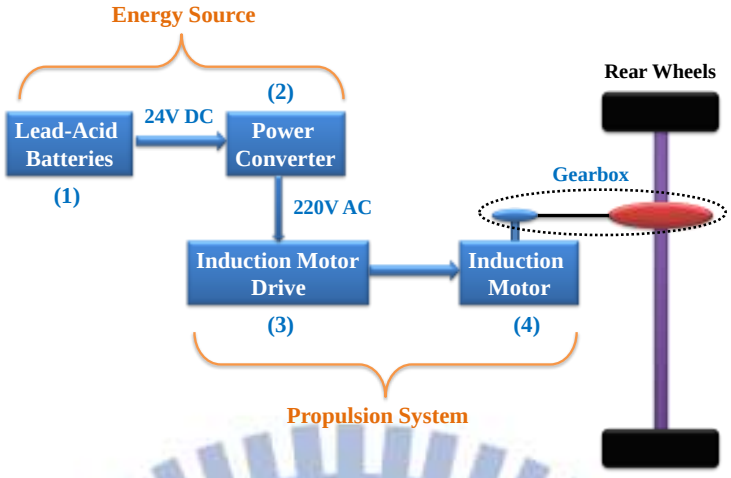

(a) Illustration of mechanical structure of the experimental electric vehicle

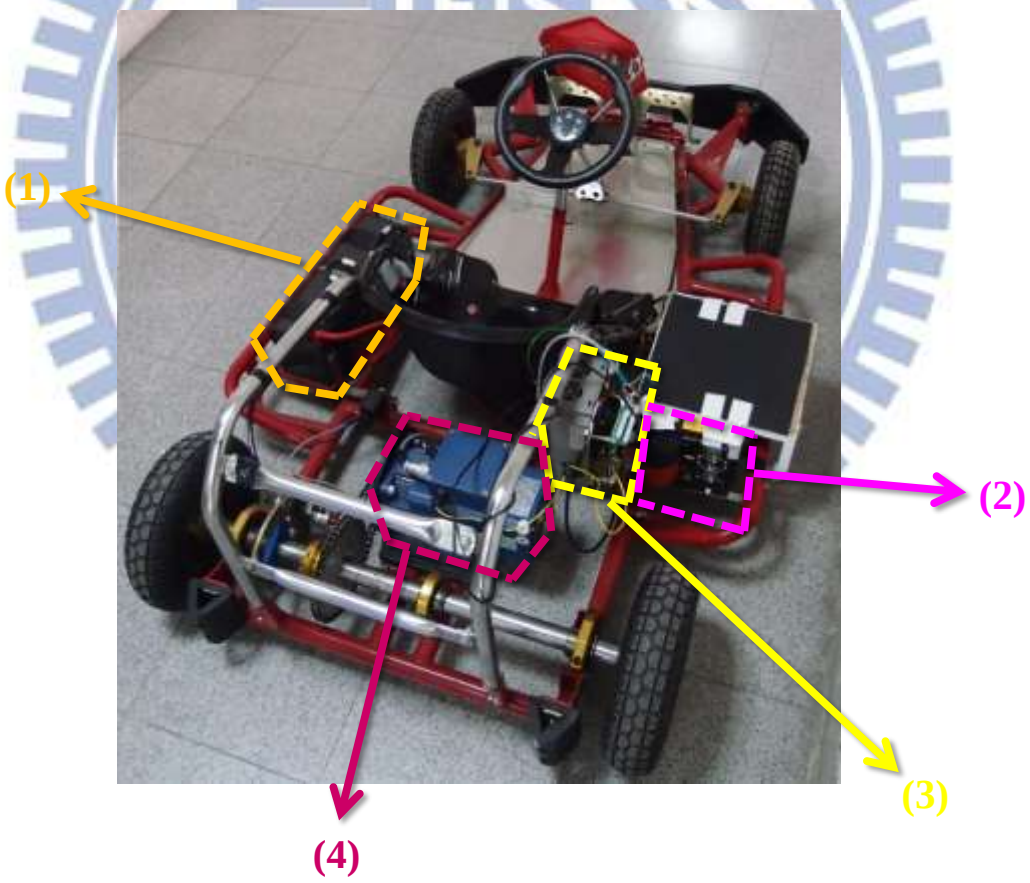

(b) The experimental electric vehicle

Fig. 2-13 Overall structure of the experimental electric vehicle

(1) Lead-acid batteries

Energy source is provided by two lead-acid batteries in series connection manufactured by Tinshfom Coporation. The voltage is 24V in total as shown in Fig. 2-14. The datasheet of the battery is listed in Table 2-1.

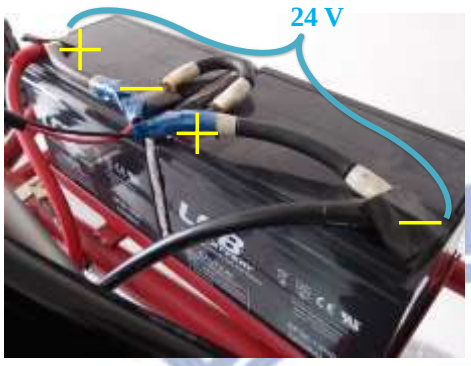

Fig. 2-14 The lead-acid batteries

Table 2-1 Datasheet of the lead-acid battery

Type	SP38-12NE
Nominal voltage	12 V
Nominal capacity	38 Ah
Dimension	197×130×159 mm
Weight	11.65 kg

(2) Power converter

The power converter of type SP3000W manufactured by SunHam Coporation, as shown in Fig. 2-15, is responsible for converting 24V DC into 220V AC. Its datasheet is listed in Table 2-2. The converted AC is then fed into the induction motor drive.

Fig. 2-15 The power converter

Table 2-2 Datasheet of the power converter

Input voltage	DC 20~30 V
Maximum input current	125 A
Output voltage	AC 220 V
Output frequency	60 Hz
Output power	3000
Efficiency	> 85 %
Dimension	360×169×152 mm
Weight	7 kg

(3) Induction motor drive

The induction motor drive is composed of a power stage module and a control system module, as shown in Fig. 2-16. Basically, the power stage module can be divided into two parts: a three-phase bridge rectifier and a three-phase inverter. The former one rectifies AC input to a DC, providing electromotive force for the DC-bus. Then, three legs of IGBTs (Insulated Gate Bipolar Transistor) are

controlled by the control system module to generate proper AC for the motor. The illustration of the induction motor drive is shown in Fig. 2-17.

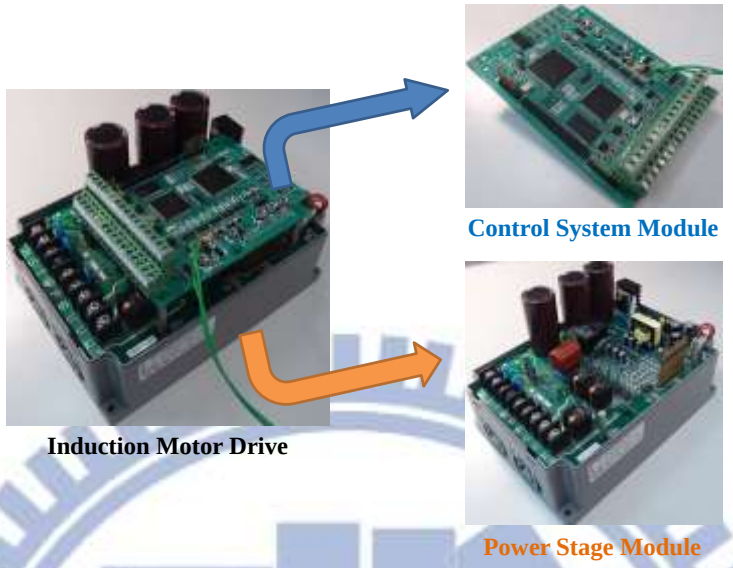

Fig. 2-16 The induction motor drive

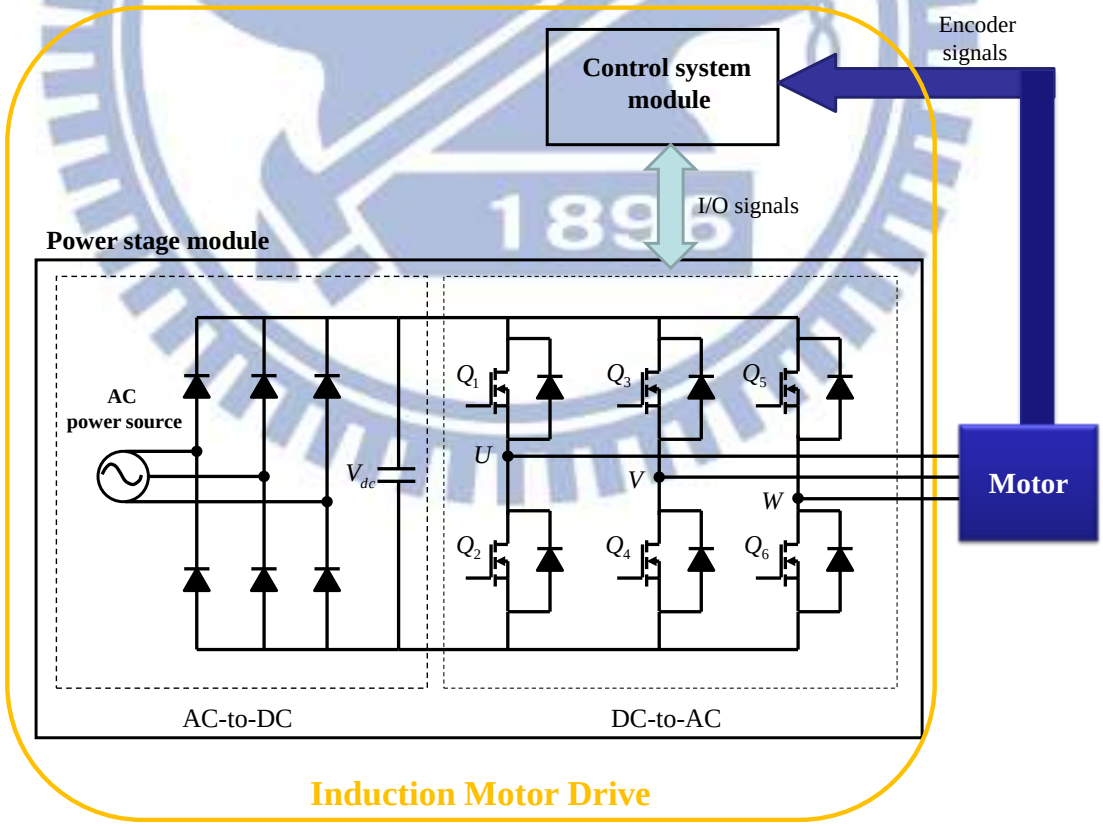

Fig. 2-17 Illustration of the induction motor drive

The power stage module is manufactured by Long-Shenq Electronic Corporation, whose product type is LS800-22K2-TD, while the control system module is developed by Syntec Incorporation. The DSP controller of type TMS320F28335 manufactured by the Texas Instruments is the processing core. Its detailed features and functions can be found in [18].

(4) Induction machine

A three-phase squirrel-cage induction motor with 0.75 kW as shown in Fig. 2-18 is applied to the propulsion of the vehicle. Its nameplate is shown in Table 2-3.

Fig. 2-18 The 0.75-kW induction motor adopted in this study

Table 2-3 Nameplate of the induction machine

Manufacturer	Cheng-Chang Machine Eletronic Corporation	
Type	SVM-80SS	
Rated power	0.75 kW	
Rated frequency	51.5 Hz	
Rated slip	45 rpm	
Rated speed	1500 rpm	
Rated torque	4.7 N-m	
Rated line Voltage	Y connection	380 V
	Δ connection	220 V
Rated line Current	Y connection	1.9 A
	Δ connection	3.3 A
Weight	13.56 kg	
Encoder resolution	1024 pulses per revolution (ppr)	

The mechanical power is transmitted from the induction motor to the rear wheels with a gear ratio at 10:52, as shown in Fig. 2-19. Because the diameter of the rear wheel is around 35 cm, the speed of the vehicle in km/hr, *V*, at given motor rotational

speed in rpm, n_{motor}, can be approximated as

$$V = \frac{n_{\text{motor}}}{5.2} \times 60 \times \frac{0.35\pi}{1000} \approx 0.0127 n_{\text{motor}} \tag{2-69}$$

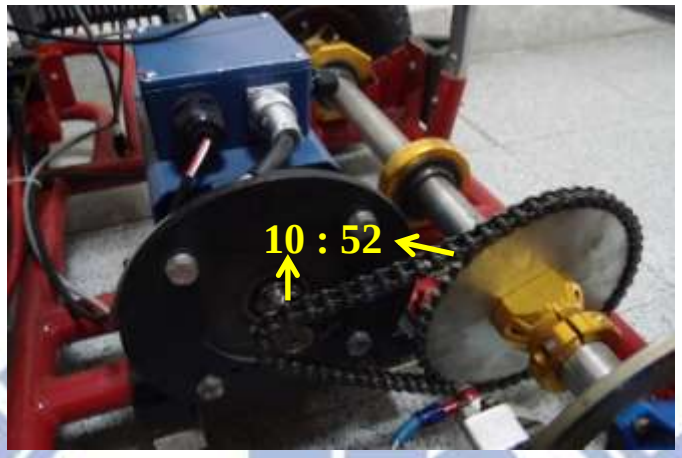

Fig. 2-19 Gear ratio 10:52 of the gearbox

A variable resistor with 50Ω is connected to the acceleration pedal with a set of mechanical devices as shown in Fig. 2-20(a) such that by stepping on the pedal the resistance of the resistor can be adjusted. We then simply read the voltage across the terminal b and c in the control program so that the demand of the driver can be tranferred into the stator phase current command, and Fig. 2-20(b) illustrates the operation.

Finally, a plate on the shaft of rear wheels is firmly vised by the device shown in Fig. 2-21 so that the vehicle can be stopped by stepping on the braking pedal.

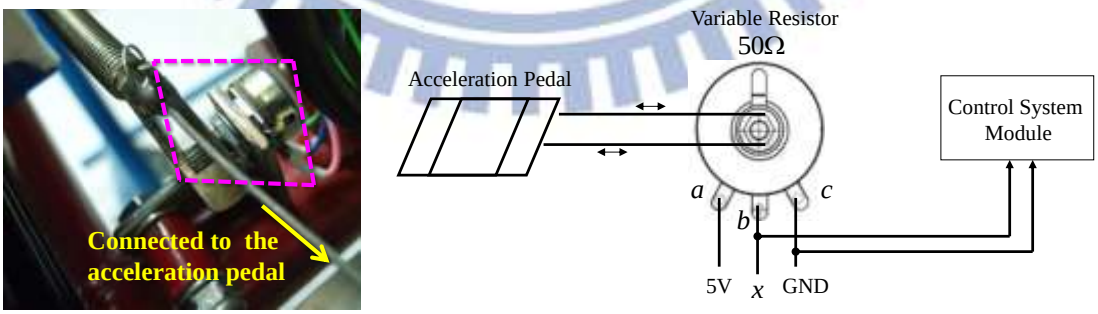

(a) The variable resistor (b) Illustration of the accelerator system

Fig. 2-20 Mechanism of the accelerator

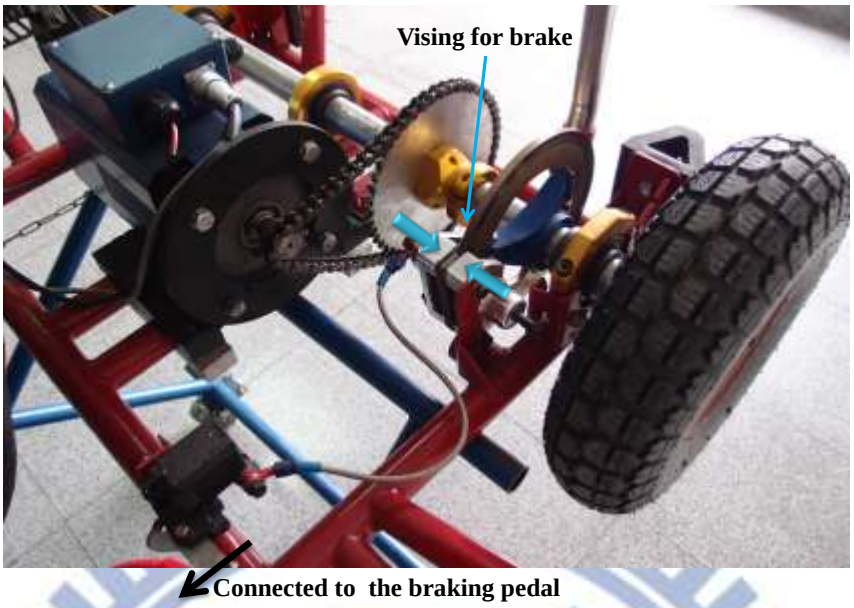

Fig. 2-21 The braking mechanism

2.5.2 Control program of the system

The indirect vector control is exploited as the traction control of the electric vehicle in this study, which is fully digitized and implemented on the DSP controller. The block diagram of the control scheme is shown in Fig. 2-22.

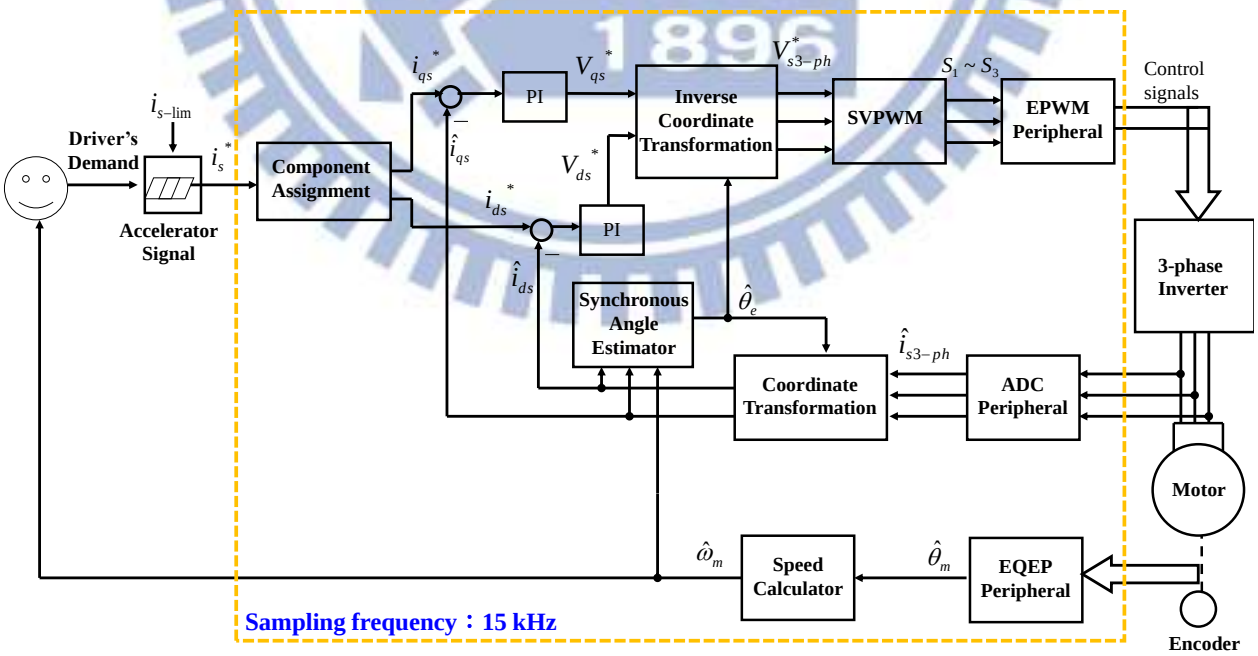

Fig. 2-22 Control scheme implemented on the DSP controller

As illustrated in Fig. 2-22, the driver's demand is transferred into the stator current command followed by the component assignment, which is functional as dividing the given stator current command into *d*-*q* current commands. The *d*-axis current command is normally selected as a constant value. Then, the *q*-axis current command is determined by

$$i_{qs}^{*} = \sqrt{i_{s}^{*2} - i_{ds}^{*2}} \tag{2-70}$$

Particularly, a switch connected to 5V-source is used for specifying forward or backward driving. The vehicle is operated at forward driving mode when the switch is off, and the *q*-axis current command is set as (2-70). When the switch is on, the *q*-axis current command is set as negative for reverse rotation of the machine. Since the maximum stator current is determined by the thermal rating of the motor and the inverter as discussed in Section 2.4.1, the stator current command is limited by $i_{s\text{-lim}}$, 2.576 pu (1 pu stands for 3.3 A in the system).

Two PI controllers are presented for current regulation, generating *d*-*q* voltage commands. Then, transformation between the three-phase system and the synchronous reference frame is managed by the blocks of coordinate transformation and inverse coordinate transformation, which is based on the estimated synchronous angle provided by the synchronous angle estimator, as discussed in Section 2.3.2. Finally, to generate appropriate control signals according to the three-phase voltage commands for the inverter, the space vector pulse width modulation (SVPWM) approach is applied. The flow chart of the control program is illustrated in Fig. 2-23, and the sampling frequency of the system is 15 kHz.

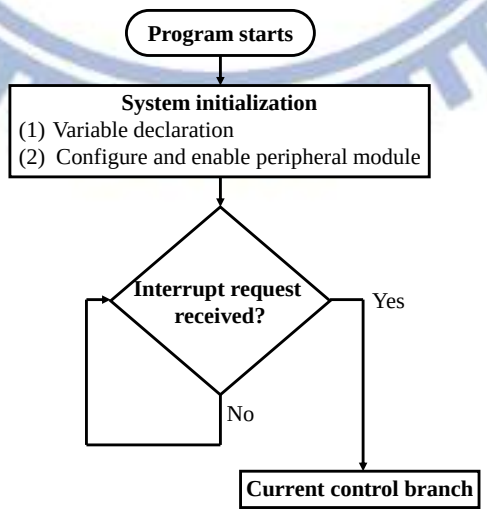

(a) Main program

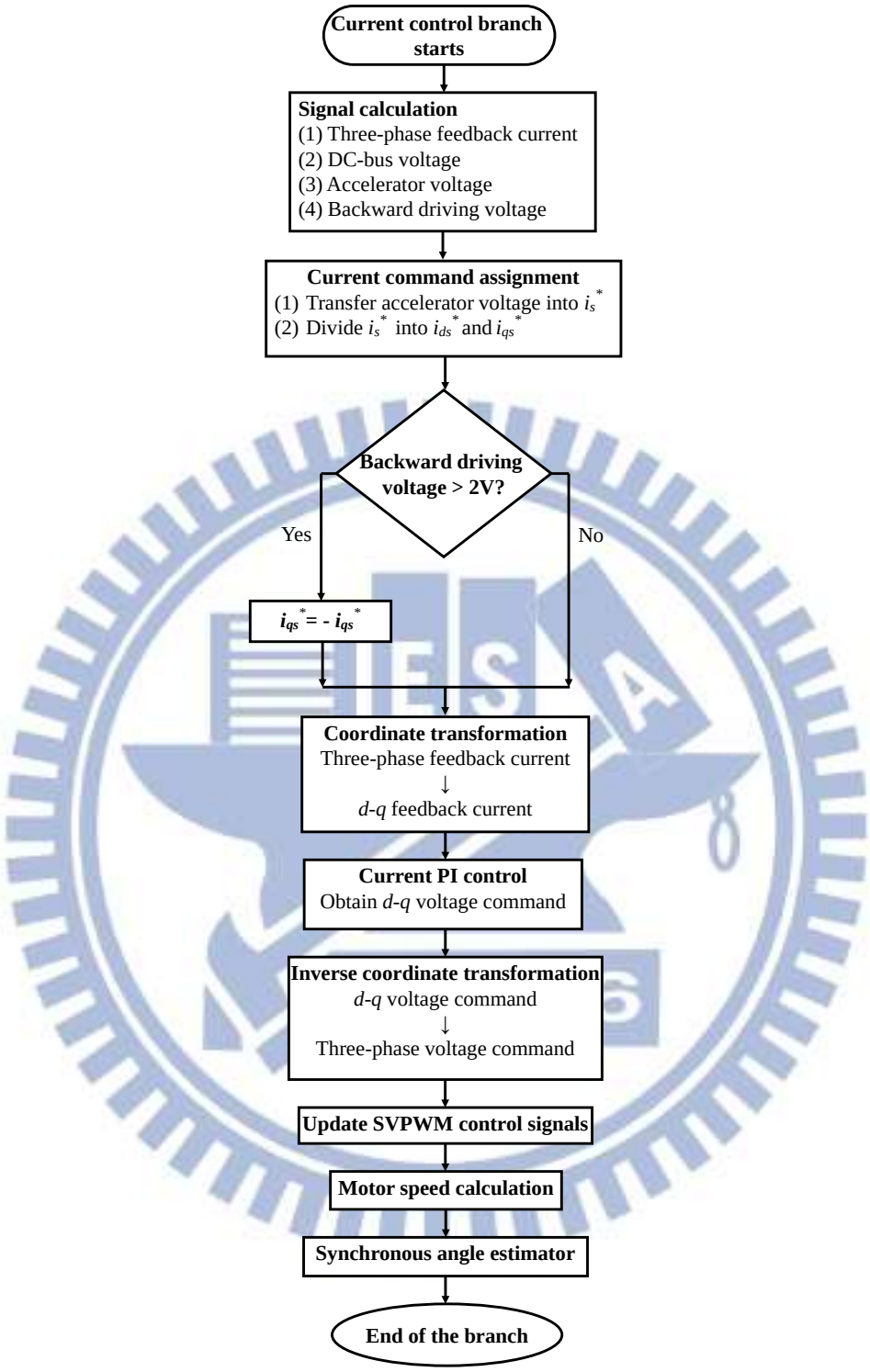

(b) Current control branch

Fig. 2-23 Flow chart of the control program

There are three processing modules, i.e. EPWM, ADC, and EQEP peripherals, of the DSP controller that play an important role in the control scheme. Their functions and relevant configurations are briefly described as below.

(1) EPWM (Enhanced Pulse Width Modulation) peripheral module [19]

Fig. 2-24 shows the block diagrams of seven submodules in the EPWM peripheral. The main tasks of this peripheral in the system are:

- Generate an interrupt for the current control branch.
- Trigger a start-of-conversion for ADC module.
- Determine proper PWM control signals for the inverter.

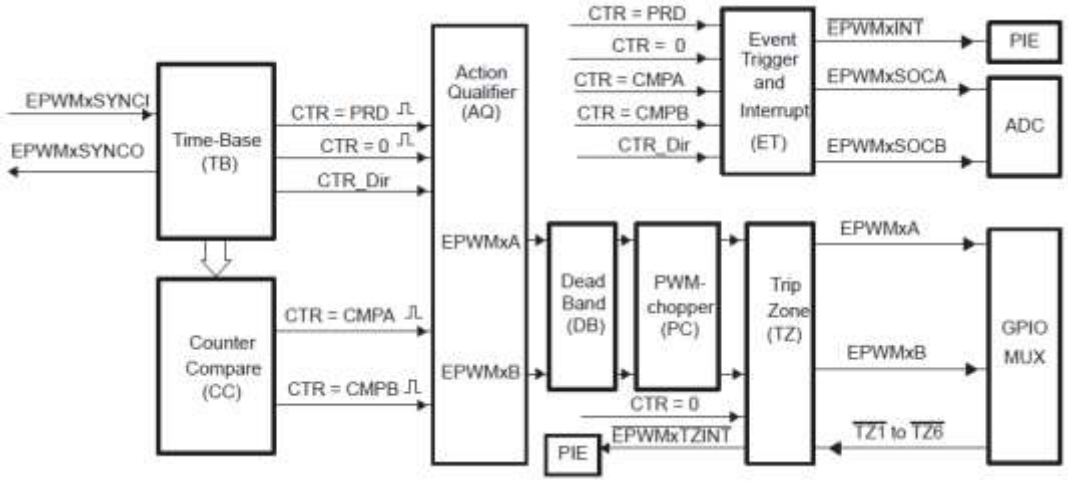

Fig. 2-24 Block diagram of the EPWM peripheral module

Some important functions of applied submodules are summarized as follows:

i. TB submodule

- Configure the rate of the time-base clock (TBCLK).
- Specify the time-base counter (TBCTR) period and the counter mode.
- Generate two events:
  - ✧ CTR = PRD: Time-base counter equal to the specified period (TBPRD).
  - ✧ CTR = 0: Time-base counter equal to zero.

ii. CC submodule

- Generate two events based on programmable time stamps using the CMPA and CMPB registers:
  - ✧ CTR = CMPA: Time-base counter equal to the CMPA register.
  - ✧ CTR = CMPB: Time-base counter equal to the CMPB register.

iii. AQ submodule

- Qualify and generate actions (set, clear, and toggle) based on the following events:
  - ✧ CTR = PRD

- ✧ CTR = 0
- ✧ CTR = CMPA
- ✧ CTR = CMPB

- Provide independent control of events when the time-base counter is increasing and decreasing.

iv. DB submodule

- Add programmable delay to rising edges (RED) of the control signal.
- Add programmable delay to falling edges (FED) of the control signal.

v. ET submodule

- Receive four events generated by the TB and CC submodules, i.e.
  - ✧ CTR = PRD
  - ✧ CTR = 0
  - ✧ CTR = CMPA
  - ✧ CTR = CMPB
- Issue interrupt requests and start of conversion of ADC based on the prescaling logic at
  - ✧ Every event
  - ✧ Every second event
  - ✧ Every third event

The settings of the EPWM periphral in the system are summarized as follows:

- The time-base clock rate is configured at 150 MHz.
- The counter mode is set as up-down-count mode.
- TBPRD is set as 5000.
- The interrupt for current control branch is triggered and serviced at every event where TBCTR = 0
- The start-of-conversion of ADC is triggered when TBCTR = TBPRD.
- Set the EPWMxA signal to high level when TBCTR = CMPA and the counter is increasing, and clear the EPWMxA signal when TBCTR = CMPA and the counter is decreasing.

The switches at the upper and lower leg cannot be simultaneously on, or they will be destroyed by incredibly large current due to short circuit. Ideally, the control signals for switches at upper and lower leg can be arranged as shown in Fig. 2-25. However, a short reaction time period exists after the switches receive

signals in practice as shown in Fig.2-26(a). Therefore, a so-called dead-time must be inserted between edges of control signals for upper and lower legs for prevention of simultaneous conduction as shown in Fig.2-26(b).

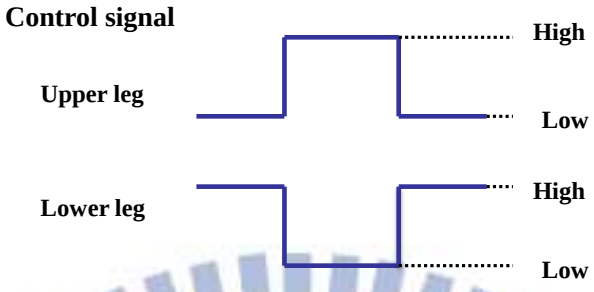

Fig. 2-25 Control signals for ideal switches

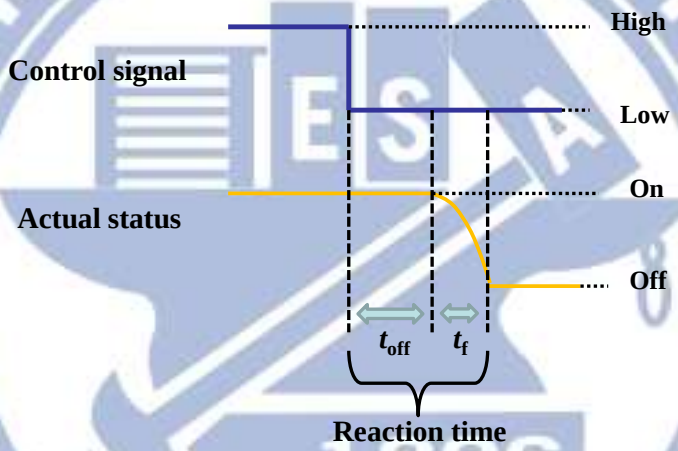

(a) Actual response when switches receive a control signal

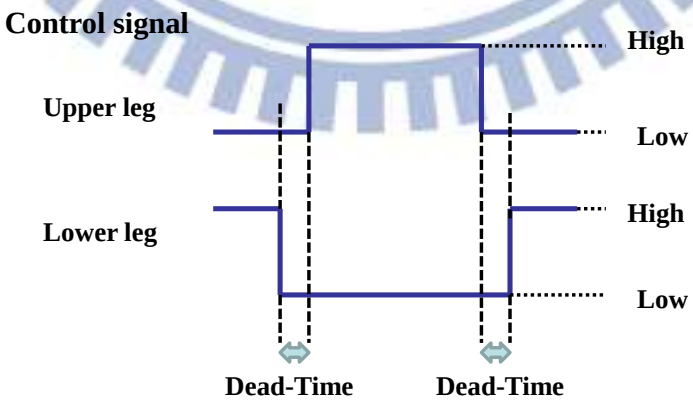

(b) A control signal added with the dead-time

Fig. 2-26 Illustration of control signals of power switches

The dead-time can be determined by characteritics of the power switches as shown in Table 2-4 taken from the datasheet. Accordingly, we set the dead-time as 1.5 μs, which is a bit larger than the turn-off time, 1.35μs, just in case of any deviation occurs. Complete operation of the EPWM module configured in the system is illustated in Fig. 2-27.

Table 2-4 Turn-off time of the power switches

Turn-Off time	Delay time (t_{off})	1.0 μs
	Falling time (t_f)	0.35 μs

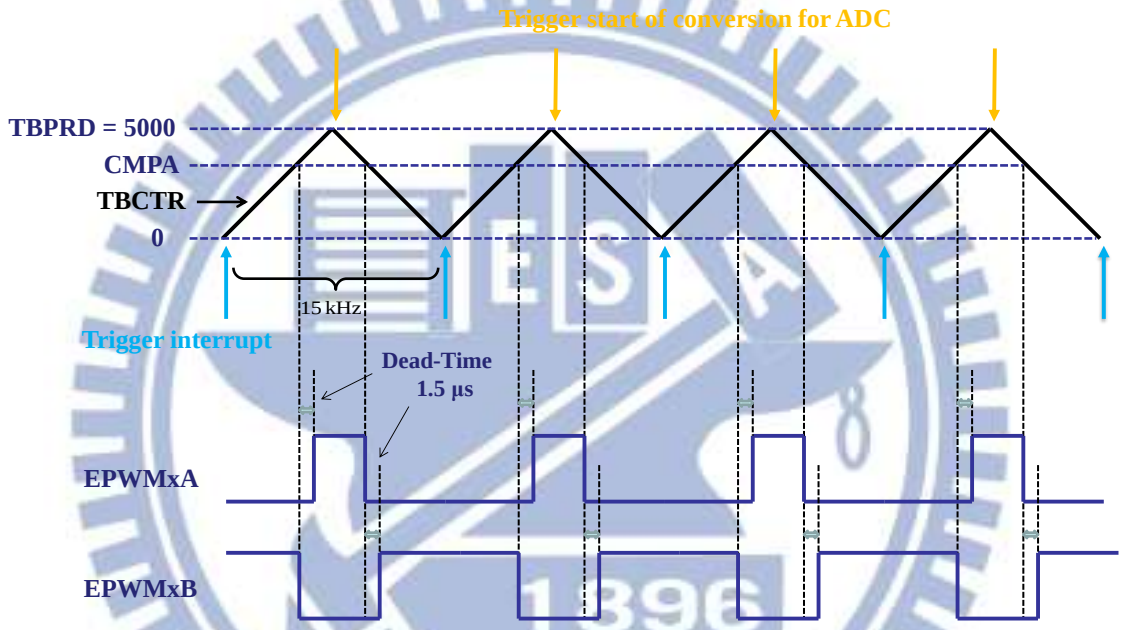

Fig. 2-27 Complete operation of the configured EPWM peripheral module

(2) ADC (Analog-to-Digital Converter) peripheral module [20]

The main features of the ADC peripheral module include:

- 16-channel, multiplexed inputs allow analog signal from 0 to 3 V
- 12-bit ADC core with built-in dual sample-and-hold (S/H)
- Fast conversion time runs at 12.5-MHz ADC clock
- 16 result registers storing converted digital value:

$$\text{Digital value} = 0, \qquad \text{if input} \le 0\,\text{V}$$

$$\text{Digital value} = 4096 \times \frac{\text{Input voltage} - \text{ADCLO}}{3}, \qquad \text{if } 0\,\text{V} \le \text{input} \le 3\,\text{V}$$

$$\text{Digital value} = 4095, \qquad \text{if input} \ge 3\,\text{V}$$

where ADCLO is the 43th pin of the DSP controller connected to a reference voltage, and it is grounded in the control system board.

Any one of the sixteen channels can be selected through analog MUXs for conversions. The module allows the user to convert the same channel multiple times, which means oversampling algorithm is available. Once the conversion is finished, the converted digital value of the selected channel is stored in its respective ADCRESULT register. The block diagram of the ADC module is shown in Fig. 2-28.

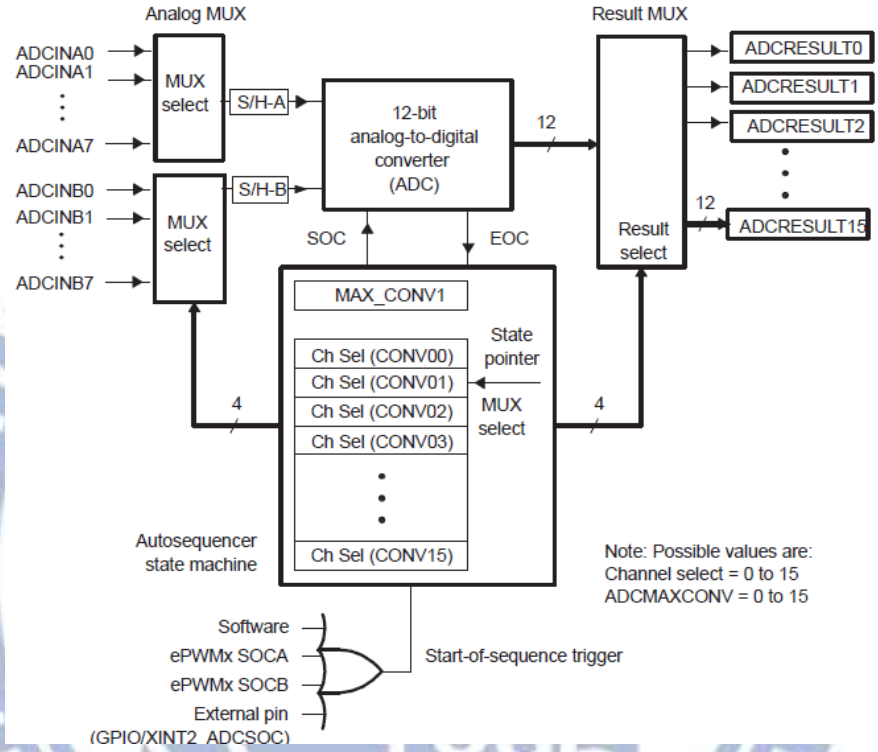

Fig. 2-28 Block diagram of the ADC peripheral module

The following table lists the signal sources of used channels in the control system board.

Table 2-5 ADC channels in the control system board

Channel	Signal source
ADCINA0	Phase U current sensor
ADCINA1	Phase V current sensor
ADCINA2	Phase W current sensor
ADCINA3	DC-Bus voltage sensor
ADCINA5	Terminal voltage of the variable resistor connected to the accelerator
ADCINA6	Backward driving voltage

The number of conversions in one sequence is determined as 15 for oversampling four times on each current sensor output and sampling once for the DC-bus voltage sensor output, once for the terminal voltage of the variable resistor, and once for the backward driving voltage. The conversion results will be stored in the ADCRESULT register by order, which is specified as follows:

ADCINA0 → ADCINA1 → ADCINA2 →
ADCINA0 → ADCINA1 → ADCINA2 →
ADCINA0 → ADCINA1 → ADCINA2 →
ADCINA0 → ADCINA1 → ADCINA2 →
ADCINA3 → ADCINA5 → ADCINA6

Note that the four-time oversampling on each current sensor is performed. Such arrangement can effectively filter out noises with a medium filter. The illustration is shown in Fig. 2-29.

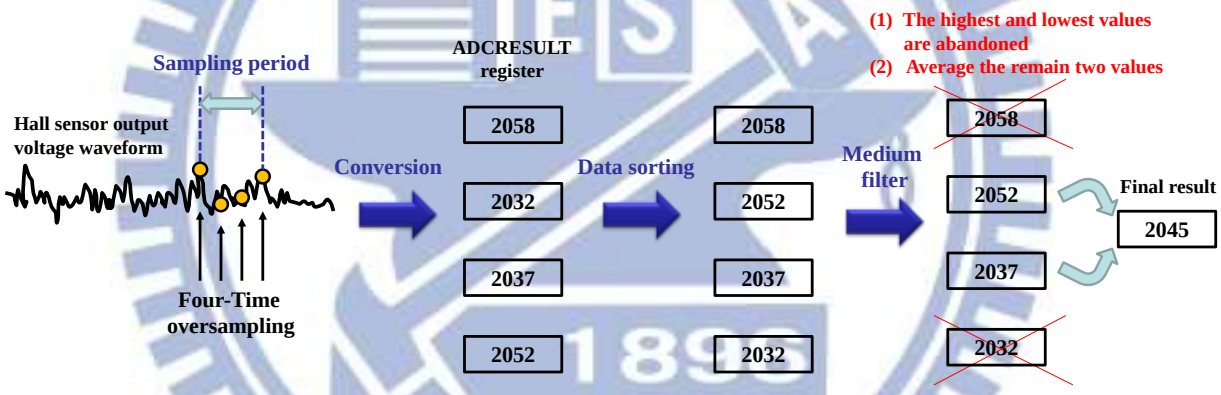

Fig. 2-29 An example of the oversampling and the medium filter processing

Once the converted digital value of the current sensor output voltage in one sampling period is obtained by the process as x, the actual current magnitude, y, corresponding to x can be recovered by

$$y = \frac{50}{8} \times \frac{12}{4095} \times (x - 2252) \quad , \tag{2-71}$$

which is derived from the numerical relationship based on the hardware design of the system shown in Fig. 2-30.

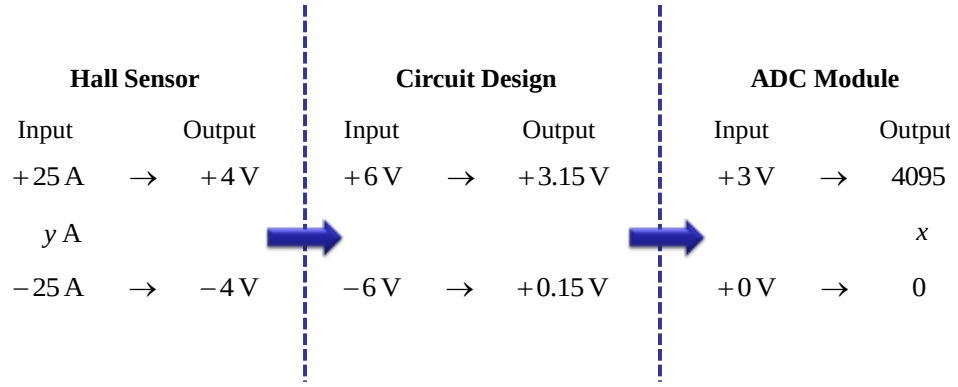

Fig. 2-30 Input-output relationship of the system hardware

Nevertheless, errors exist inevitably both in the resistance and the inductance of electrical components. Thus, the equation (2-71) must be tuned so that the calculated current magnitude y and its real value match. The final equation applied in the phase current recovery is

$$y = Gain \times (x - Offset) \tag{2-72}$$

where the term *Gain* and *Offset* are determined experimentally, with which y can be equal to the real current value measured by the oscilloscope as shown in Fig. 2-31. Similar manner is also applied to the DC-bus, accelerator, and backward driving voltage signal recovery in the program.

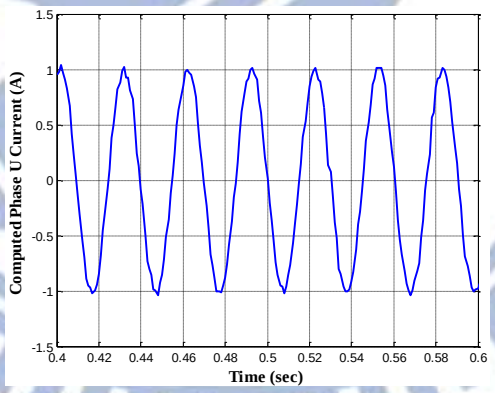

(a) Computed phase U current

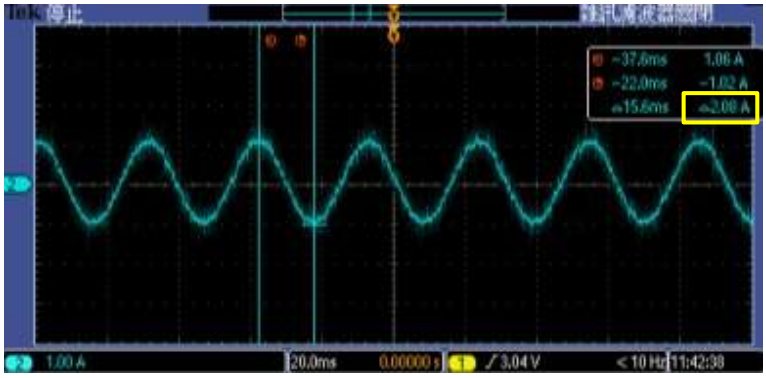

(b) Measured phase U current by the oscilloscope

Fig. 2-31 Experimental reults of phase current signal recovery

(3) EQEP (Enhanced Quadrature Encoder Pulse) peripheral module [21]

The EQEP peripheral module decodes the pulsed signals generated by an incremental position encoder mounted on the motor shaft. Fig. 2-32 shows the functional block diagram of the EQEP module.

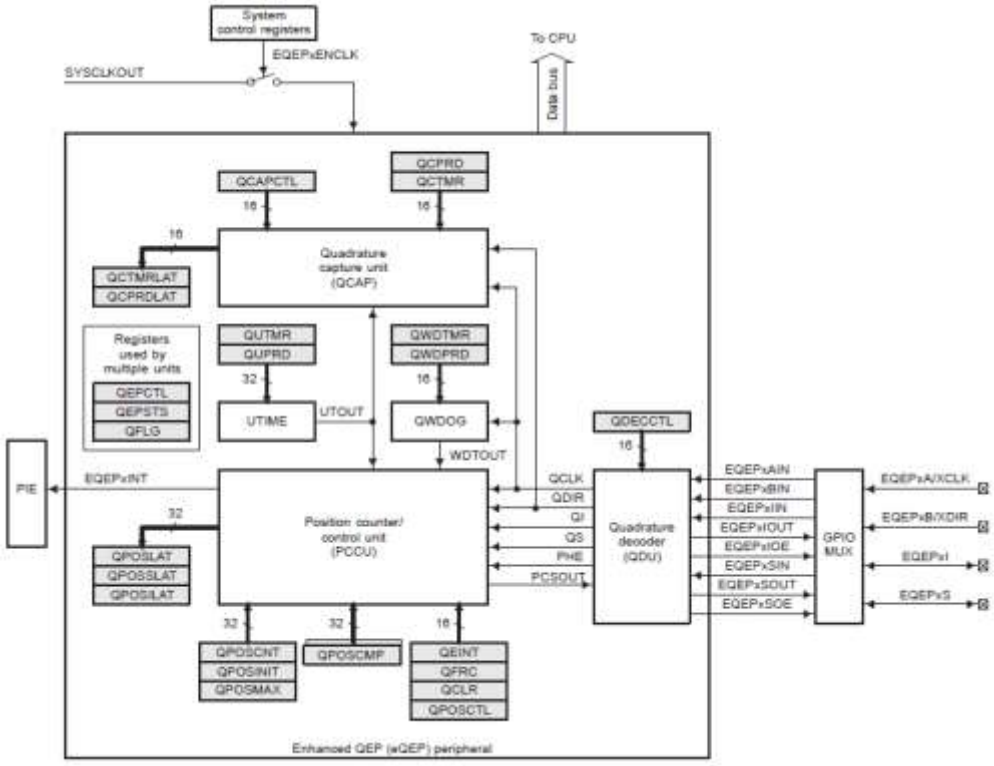

Fig. 2-32 Block diagram of the EQEP peripheral module

Basically, an incremental quadrature encoder provides two square wave signals (A and B) 90 degrees out of phase whose relationship is used to determine the rotational direction, and number of pulses from the absolute positional origin, indicated by an index signal (Z), is adopted to obtain the relative position information. For forward rotation, A signal leads B signal, and vice versa. Then, the quadrature-clock (QCLK) and direction signals (QDIR) are generated by the quadrature decoder according to these three types of signals. Typical signals with forward rotation generated by an encoder are shown in Fig. 2-33.

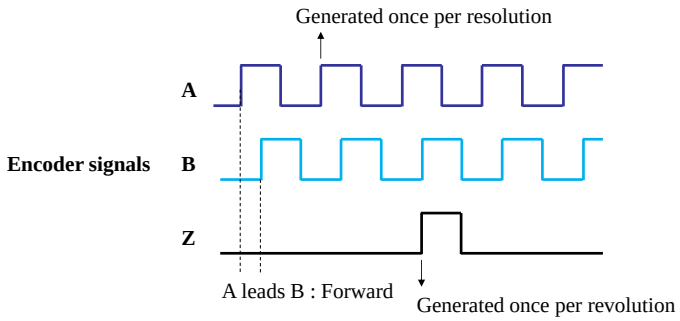

Fig. 2-33 Output signals of an encoder with forward rotation

Since a quadrature type of position encoder is installed in the induction motor, the EQEP module should be operated at the quadrature-count mode for decoding. Both edges of A and B signals are detected to generate counting pulses for the position counter (QPOSCNT). Therefore, the frequency of the generated clock of the EQEP logic, QCLK, is four times that of the input sequence. Since the resolution of the mounted encoder on the motor is 1024 ppr, the maximum counter value is set as 4095. An illustration of the quadrature counting is shown in Fig. 2-34.

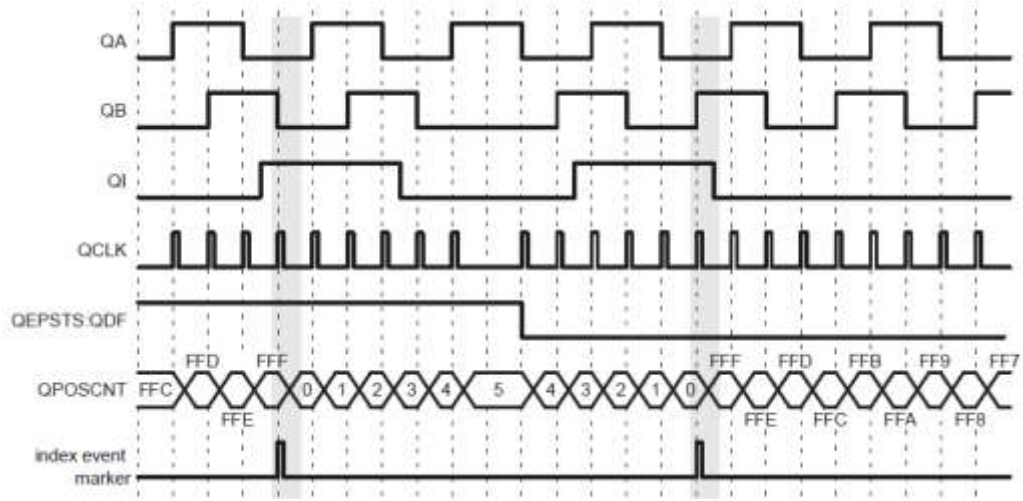

Fig. 2-34 Operation of the EQEP module in the quadrature-count mode

Once the positional information is decoded, the rotational speed of the machine can be obtained by (2-73) with the built-in capture unit of the module as

$$v(k) = \frac{C}{\Delta T} \tag{2-73}$$

where C is the specified unit position, and ΔT indicates the time interval within a unit position. In other words, the speed is calculated by measuring the elapsed time between sucessive quadrature pulse edges.

The configuration of the EQEP module is described as follows. The unit position event (UPEVNT) is specified as one resolution. Also, the capture clock (CAPCLK) is configured as SYSCLKOUT / 128 for the capture timer (QCTMR), where SYSCLKOUT is the operational clock of the DSP controller, and it is equal to 150 MHz. Then, the value of the timer is latched into the capture period register (QCPRD) on every unit position event and the capture timer is then reset automatically. Thus, $\Delta T = (\text{the period of CAPCLK}) \times \text{QCPRD}$ in (2-73), and an example of the capture unit operation is shown in Fig. 2-35.

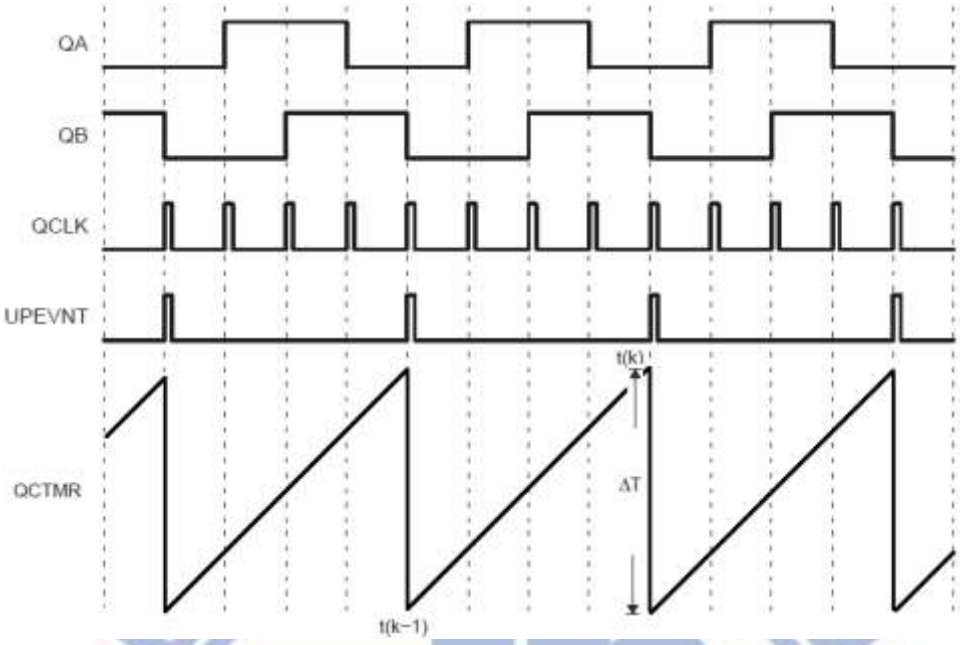

Fig. 2-35 Illustration of Capture unit operation

Finally, a first-order lowpass filter with 900-Hz cut-off frequency is applied after the speed estimation with (2-73) to reduce the noise effect.

Chapter 3

Servo Traction Control of the Electric Vehicle

In this chapter, high performance servo control of the induction machine with significant improvement of the acceleration ability and the operating efficiency has been developed, and it has been further implemented on the electric vehicle. An identification process of the rotor time costant is first developed to precisely obtain the parameter for implementation of the present indirect vector control. Then, the maximum torque per amperage control is realized for the machine to provide the maximum acceleration of the vehicle. Finally, the operation obtaining the highest efficiency, which can be fulfilled with correct setting of the flux-producing current, has been experimentally verified. Results show that performance of an electric vehicle can achieve better operations in real driving tests.

3.1 Identification Process of the Rotor Time Constant

In order to perform servo induction motor control with the indirect vector control scheme, the rotor time constant of the machine must be known for estimation of the synchronous angle as seen in Fig. 2-5. However, it is usually not precisely provided by the machine manufacturer, and conventional identification approaches are not suitable for electric-vehicled applications. Thus, an accurate and simple identification of the rotor time constant is desirable such that it can be directly performed on the vehicle without modifying the control scheme.

3.1.1 Effects of the rotor time constant

The slip frequency has been derived in Section 2.3.1 as

$$\omega_{slip} = \frac{1+p\tau_r}{\tau_r}\frac{i_{qs}}{i_{ds}} \tag{3-1}$$

where τ_r is the actual rotor time constant, and i_{qs} and i_{ds} are the actual q-axis and d-axis current flowing into the motor. Since the rotor time constant is much smaller than the mechanical constant of the vehicle, dynamics of (3-1) can be neglected as

referred to the mechanical system. Therefore, it can be rewritten by substituting $p = 0$ as

$$\omega_{slip} = \frac{1}{\tau_r}\frac{i_{qs}}{i_{ds}} \quad , \tag{3-2}$$

and the magnitude of the actual stator phase current is given by

$$i_s = \sqrt{i_{ds}^2 + i_{qs}^2} \tag{3-3}$$

In the indirect vector control, the slip frequency is estimated based on

$$\hat{\omega}_{slip} = \frac{1 + p\hat{\tau}_r}{\hat{\tau}_r}\frac{\hat{i}_{qs}}{\hat{i}_{ds}} \tag{3-4}$$

where parameters with the head notation stands for their estimated values in the controller. Similarly, the equation (3-4) can be simplified if referred to the mechanical system as

$$\hat{\omega}_{slip} = \frac{1}{\hat{\tau}_r}\frac{\hat{i}_{qs}}{\hat{i}_{ds}} \tag{3-5}$$

The magnitude of the estimated or feedback stator phase current can be represented as

$$\hat{i}_s = \sqrt{\hat{i}_{ds}^2 + \hat{i}_{qs}^2} \tag{3-6}$$

Under current closed-loop control, the constraints are given by [26]

$$\omega_{slip} = \hat{\omega}_{slip} \tag{3-7}$$

$$i_s = \hat{i}_s \tag{3-8}$$

Then, we define

$$\tan\alpha = \frac{\hat{i}_{qs}}{\hat{i}_{ds}} \tag{3-9}$$

$$\tan\beta = \frac{i_{qs}}{i_{ds}} \tag{3-10}$$

Hence, by (3-2), (3-5), (3-7), (3-9), and (3-10), we obtain

$$\tan\beta = \frac{\tau_r}{\hat{\tau}_r}\tan\alpha \tag{3-11}$$

Therefore, if the estimated rotor time constant is deviated from the actual value of the

machine, the actual *d-q* axis currents flowing into the induction machine are no longer equal to their estimated values as shown in Fig. 3-1.

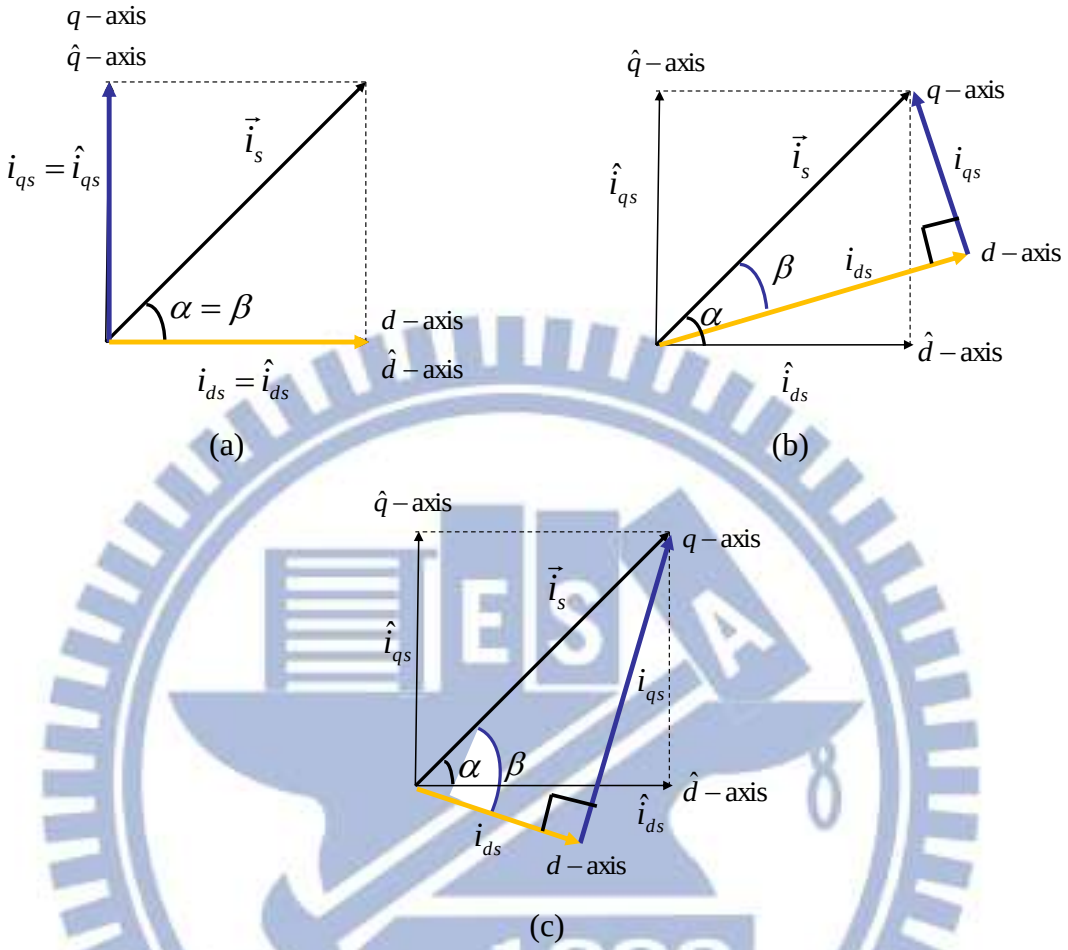

Fig. 3-1 Relationship between the estimated and actual *d-q* axis currents when (a) $\hat{\tau}_r = \tau_r$, (b) $\hat{\tau}_r > \tau_r$, and (c) $\hat{\tau}_r < \tau_r$

As seen from Fig. 3-1(a), when the estimated rotor time constant is equal to the actual value, the estimated *d-q* axes (estimated synchronous reference frame by the controller) and the actual *d-q* axes (actual synchronous reference frame of the induction machine) match perfectly. Under such conditions, it indicates that the actual *d-q* component currents are equal to their estimated or feedback value. Moreover, the flux and torque control can be completely decoupled in this condition, which is desirable in the indirect vector control scheme. However, if the estimated rotor time constant is larger than the actual value, the estimated *d-q* axes will move clockwise away from the actual ones. In this case, the actual flux component current is larger than the estimated value while the actual torque-producing current is smaller than the estimated one as shown in Fig. 3-1(b). On the other hand, if the estimated rotor time constant is smaller than the actual value, the estimated flux component current is

smaller than the actual one, but the estimated torque-producing current is larger than the actual value. The estimated *d*-*q* axes are counterclockwise away from the actual *d*-*q* axes under such circumstance. Both two cases actually are suffered from incomplete decoupled control of the flux and torque.

3.1.2 Identification of the rotor time constant

In effect, the developed torque of the induction motor is dependent on the product of the *d*-axis and *q*-axis currents as shown in (2-68). By (3-3), we can derive

$$i_{ds} = i_s \cos\beta \tag{3-12}$$

$$i_{qs} = i_s \sin\beta \tag{3-13}$$

Substitute the above equations into (2-68), and the produced torque is obtained as

$$T_e = \frac{3}{4}\frac{P}{2}\frac{L_m^2}{L_r} i_s^2 \sin 2\beta \tag{3-14}$$

Obviously, when $\beta = 45^\circ$, the maximum torque can be provided at given i_s, L_m, and L_r. Also, it can be recognized from (3-11) that $\alpha = \beta$ when the estimated rotor time constant is equal to its actual value. This concept can be further applied to develop an identification process of the rotor time constant carried out in the control scheme as shown in Fig. 3-2.

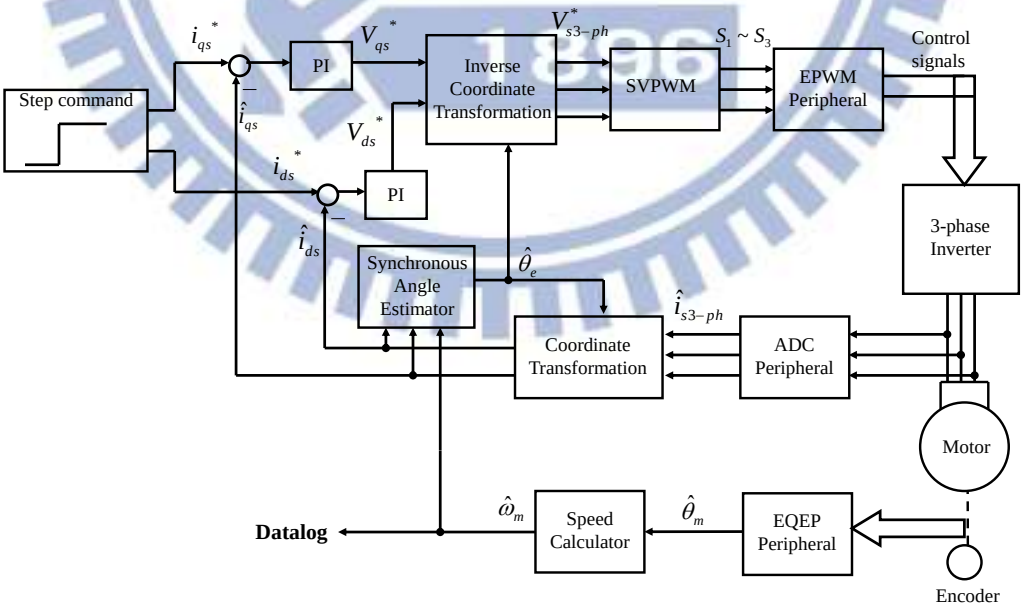

Fig. 3-2 Control diagram of the rotor time constant identification process

Procedures:

(a) Set *d*-*q* axis current command with an identical step pattern (implies $\alpha = 45^\circ$), and set $\hat{\tau}_r$ as an arbitrary value (normally smaller than 0.1) to perform the closed-loop control for the current loop. Then, record the corresponding speed response.

(b) Maintain the current command the same as in step (a), and adjust $\hat{\tau}_r$ in the program and then record the corresponding speed profile.

(c) Repeat step (b) and obtain all acceleration data with different settings of $\hat{\tau}_r$. When the maximum acceleration is obtained, the corresponding $\hat{\tau}_r$ is approximately the same as the actual value of the machine. This further shows that as $\beta = \alpha = 45^\circ$, the maximum torque can be obtained.

Here, the acceleration is recorded instead of the torque because no torque sensor is installed on the system. Such an alternative way is quite reasonable because at given load, the maximum torque will generate the maximum acceleration. Experimental results of an example with *d*-*q* axis current command = 0.4 pu and $\hat{\tau}_r$ = 0.08 s are shown in Fig. 3-3.

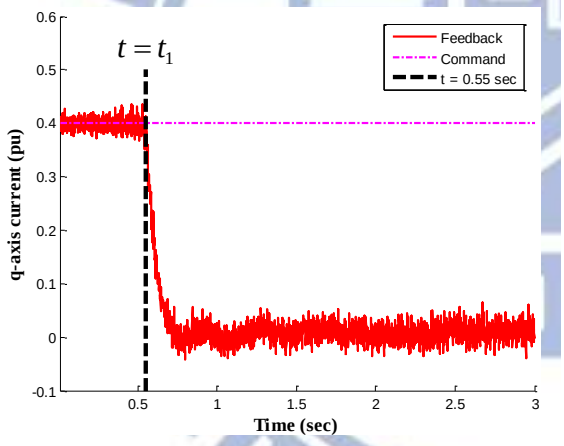

(a) *q*-axis current response

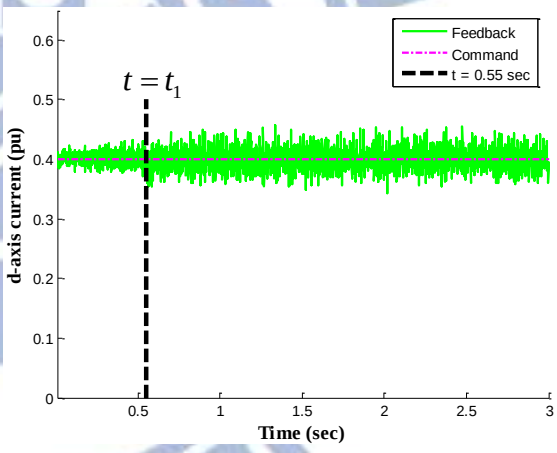

(b) *d*-axis current response

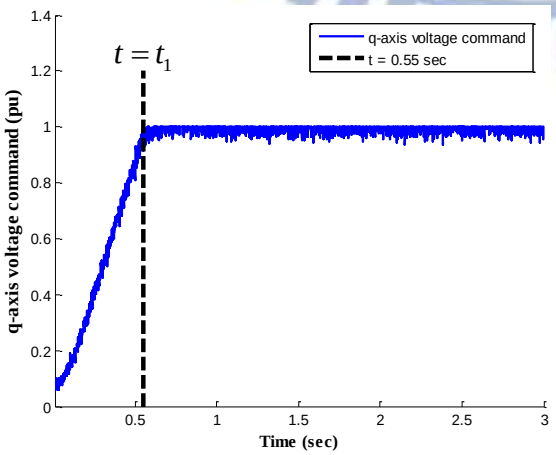

(c) *q*-axis voltage command

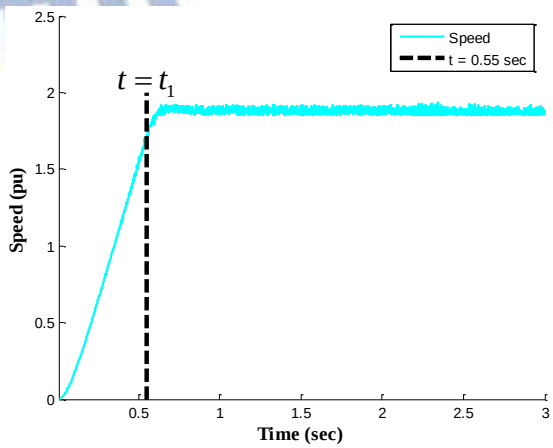

(d) speed response

Fig. 3-3 Responses with $\hat{\tau}_r = 0.08\,\text{s}$ and $i_{ds}^* = i_{qs}^* = 0.4\,\text{pu}$

As seen from Fig. 3-3, the q-axis current will decrease after a specific time instant, where the maximum supplied voltage level is reached as t_1. This is mainly caused by the growing back-emf term, $K_e\omega_m$, so that the controller cannot provide sufficient voltage on the q-axis for the i_{qs}-regulation as the speed continually increases. Therefore, the q-axis current will decrease until the developed torque is equal to the load torque where the equilibrium is obtained. This concept can be understood by observing (2-57) and Fig. 2-6.

Consequently, the acceleration obtained in the procedure (c) is the average value right before t_1, i.e. the time instant after which the q-axis current begins to decrease as shown in the following equation.

$$\bar{a} = \frac{\omega_m(t_1)}{t_1} \tag{3-15}$$

In order to verify the validity of the identification process of the rotor time constant, we first have performed four different sets of step current commands at no load as shown in Fig. 3-4, and experimental results are summarized as in Fig. 3-5.

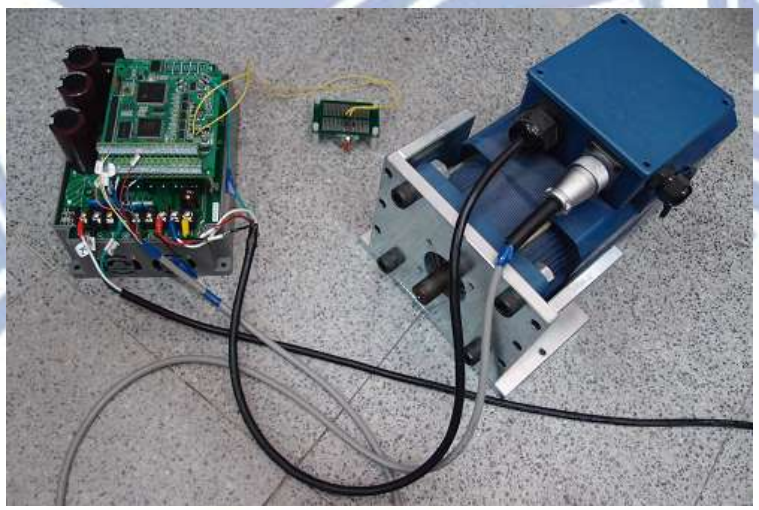

Fig. 3-4 Experimental setup of rotor time constant identification without load

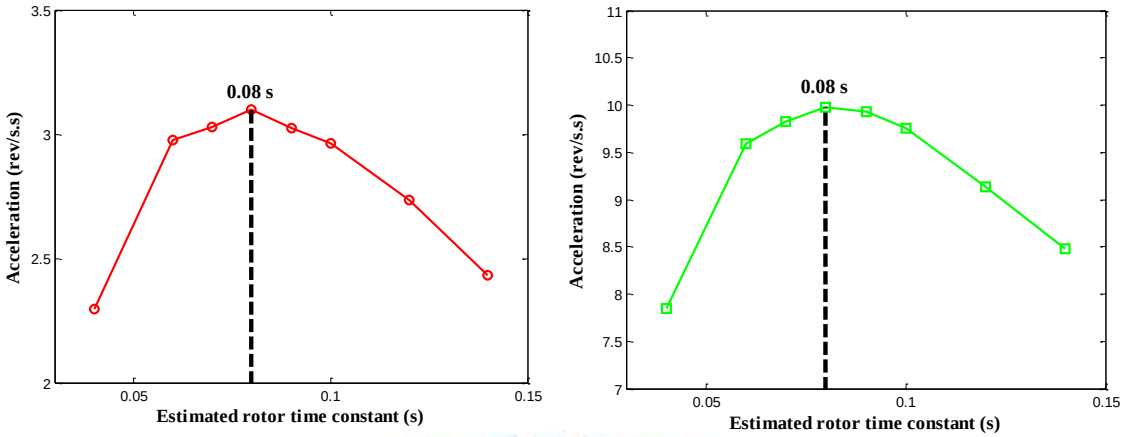

(a) $i_{ds}^{*} = i_{qs}^{*} = 0.1\,\text{pu}$ (b) $i_{ds}^{*} = i_{qs}^{*} = 0.15\,\text{pu}$

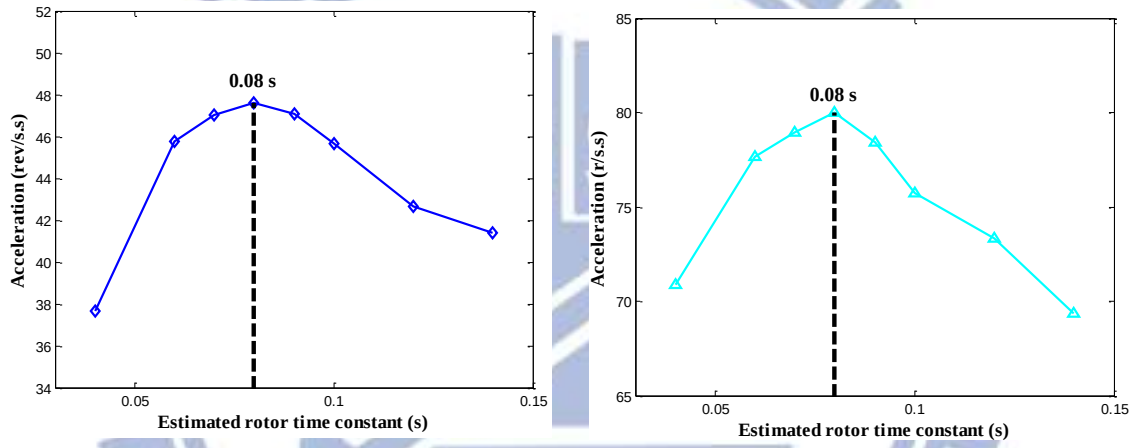

(c) $i_{ds}^{*} = i_{qs}^{*} = 0.3\,\text{pu}$ (d) $i_{ds}^{*} = i_{qs}^{*} = 0.4\,\text{pu}$

Fig. 3-5 Experimental results with different $\hat{\tau}_r$ at no-load condition

As seen from Fig. 3-5, the maximum acceleration is obtained when $\hat{\tau}_r$ is set as 0.08s regardless of four different sets of step current command magnitude. Apparently, the rotor time constant can be identified as approximately 0.08s based on the proposed approach. The result is fairly close to its nominal value 0.074s, as identified in [28].

Then, the identification process is directly performed on the vehicle placed on a supporting framework as shown in Fig. 3-6. The experimental results shown in Fig. 3-7 shows that the identified rotor time constant is also 0.08s, which is consistent with the results obtained in Fig. 3-5. Thus, the proposed identification approach is reasonably accurate and the rotor time constant can be directly identified when the machine is installed on the vehicle. Compared with the conventional identification process, the proposed method is much easier to implement.

Fig. 3-6 Experimental setup of rotor time constant identification performed directly on the vehicle

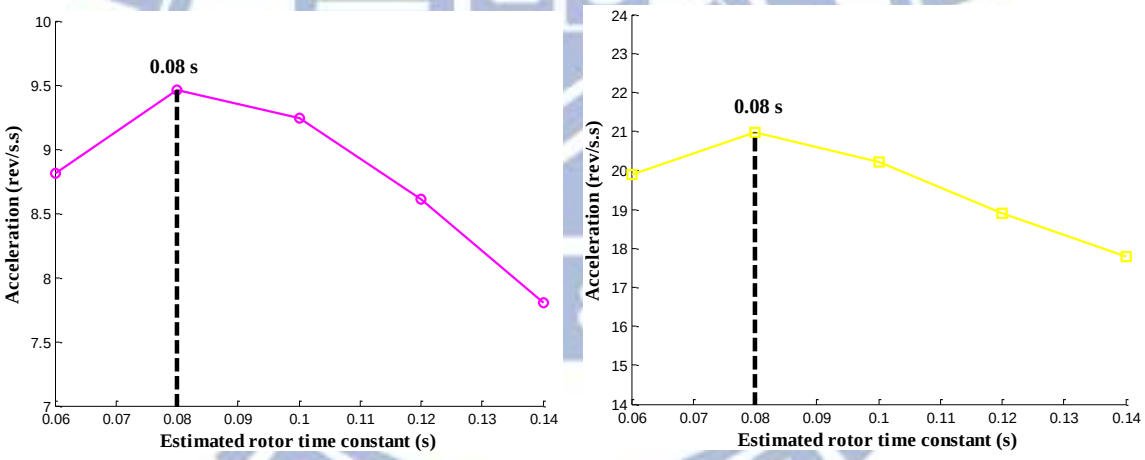

(a) $i_{ds}^{*} = i_{qs}^{*} = 0.3\,\mathrm{pu}$ (b) $i_{ds}^{*} = i_{qs}^{*} = 0.4\,\mathrm{pu}$

Fig. 3-7 Experimental results with different $\hat{\tau}_r$ performed on the vehicle

3.2 Maximum Torque per Amperage Control

3.2.1 Approach of the equal d-q current command

The maximum torque per amperage (MTPA) operation is considerably important because the developed torque is maximal at given stator current magnitude so that the

motor can provide satisfactory acceleration of the vehicle. It has been already recognized that the MTPA operation can be obtained by equally setting *d*-*q* axis current commands so that the developed torque is maximal at the given stator current magnitude as

$$i_{ds}^{*} = i_{qs}^{*} = \frac{1}{\sqrt{2}} i_{s}^{*} \tag{3-16}$$

However, such arrangement is not suitable for the real vehicle application in this study, because the torque magnitude should be larger than the rated value for propelling the vehicle with the 0.75-kW induction machine during the start-up period. As a result, the desirable operation is lost due to severe flux saturation. Speed responses of the system controlled by the method based on (3-16) with a 65-kg student seated on the vehicle when stator current command i_s^* = 1.623, 2.094, and 2.576 pu with the step pattern are shown in Fig. 3-8(b), (c), and (d), respectively, and the corresponding setup is illustrated in Fig. 3-8(a).

(a) Experimental setup of practical driving

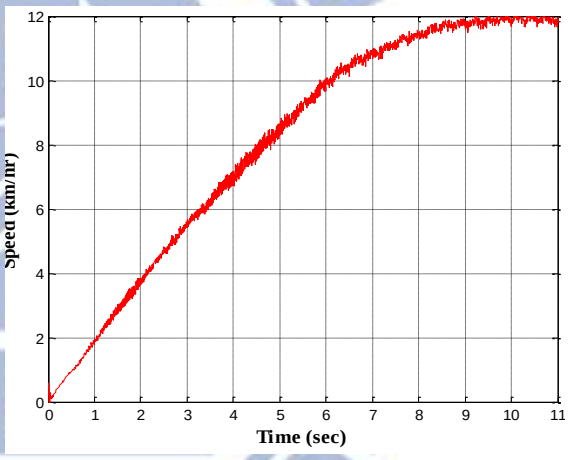

(b)

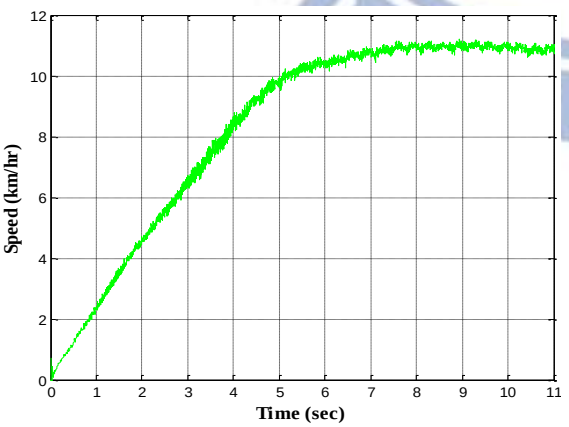

(c)

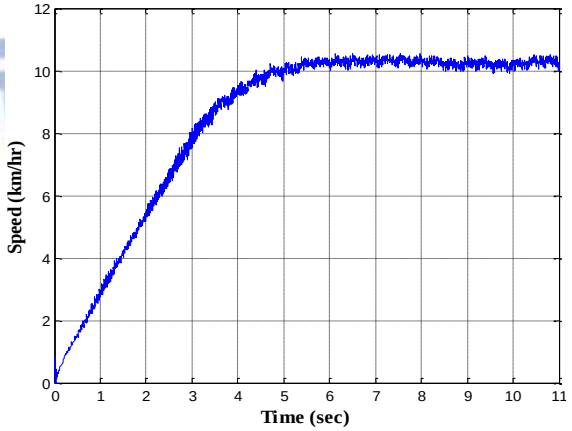

(d)

Fig. 3-8 Speed response of practical driving: (b) i_s^* = 1.623 pu (c) i_s^* = 2.094 pu (d) i_s^* = 2.576 pu

According to (3-16), the flux current command i_{ds}^* should be set as 1.1477, 1.4806, and 1.8213 pu when i_s^* = 1.623, 2.094, and 2.756 pu, respectively. As seen from Fig. 3-8, it takes quite a long time, more than 5s, accelerating from 0 to 10 km/hr. This can be explained by noting that flux saturation occurs if the flux current is operated at such high levels. Particularly, as the induction machine is saturated, a large amount of flux current can only develop a small flux gain, i.e. L_m shown in (2-54). Hence, more stator phase current should be contributed to the *q*-axis.

3.2.2 Approach of the rated flux excitation

To solve the problem caused by the approach of providing equal *d-q* current commands, it is suggested that the rotor flux linkage can be excited as its rated level with appropriate setting of i_{ds}^*, and its derivation is described as below.

From (2-39) and (2-40), the *d-q* rotor current can be represented as

$$i_{dr} = \frac{1}{L_r}(\lambda_{dr} - L_m i_{ds}) \tag{3-17}$$

$$i_{qr} = \frac{1}{L_r}(\lambda_{qr} - L_m i_{qs}) \tag{3-18}$$

By subsituting (3-17) and (3-18) into (2-37) and (2-38), respectively, the stator flux linkage can be rewritten in terms of the stator current and the rotor flux linkage as

$$\lambda_{ds} = \sigma L_s i_{ds} + \frac{L_m}{L_r}\lambda_{dr} \tag{3-19}$$

$$\lambda_{qs} = \sigma L_s i_{qs} + \frac{L_m}{L_r}\lambda_{qr} \tag{3-20}$$

Also, the rotor current terms in (2-35) and (2-36) can be eliminated by applying (3-17) and (3-18), and the equations become

$$\frac{d\lambda_{dr}}{dt} = R_r \frac{L_m}{L_r} i_{ds} - \frac{R_r}{L_r}\lambda_{dr} + (\omega_e - \omega_r)\lambda_{qr} \tag{3-21}$$

$$\frac{d\lambda_{qr}}{dt} = R_r \frac{L_m}{L_r} i_{qs} - \frac{R_r}{L_r}\lambda_{qr} - (\omega_e - \omega_r)\lambda_{dr} \tag{3-22}$$

Then, we substitute (3-19) and (3-21) into (2-33), and substitute (3-20) and (3-22) into (2-34) to obtain the following

$$V_{ds} = (R_s + R_r \frac{L_m^2}{L_r^2}) i_{ds} + \sigma L_s \frac{di_{ds}}{dt} - \omega_e \sigma L_s i_{qs} - R_r \frac{L_m}{L_r^2}\lambda_{dr} - \omega_r \frac{L_m}{L_r}\lambda_{qr} \tag{3-23}$$

$$V_{qs} = (R_s + R_r \frac{L_m^2}{L_r^2}) i_{qs} + \sigma L_s \frac{di_{qs}}{dt} + \omega_e \sigma L_s i_{ds} + \omega_r \frac{L_m}{L_r}\lambda_{dr} - R_r \frac{L_m}{L_r^2}\lambda_{qr} \tag{3-24}$$

Since the *q*-axis rotor flux linkage of the indirect vector-controlled induction machine is zero, (3-23) and (3-24) can be further simplified as

$$V_{ds} = (R_s + R_r \frac{L_m^2}{L_r^2}) i_{ds} + \sigma L_s \frac{di_{ds}}{dt} - \omega_e \sigma L_s i_{qs} - R_r \frac{L_m}{L_r^2} \lambda_{dr} \tag{3-25}$$

$$V_{qs} = (R_s + R_r \frac{L_m^2}{L_r^2}) i_{qs} + \sigma L_s \frac{di_{qs}}{dt} + \omega_e \sigma L_s i_{ds} + \omega_r \frac{L_m}{L_r} \lambda_{dr} \tag{3-26}$$

Because the stator and rotor leakage inductance are much smaller than the magnetizing inductance, the following equations hold:

$$\sigma L_s i_{ds} = (1 - \frac{L_m^2}{L_r L_s}) \cdot L_s \cdot (\frac{\lambda_{dr}}{L_m}) = (\frac{L_s}{L_m} - \frac{L_m}{L_r}) \lambda_{dr} \approx \frac{L_{lr} + L_{ls}}{L_m} \lambda_{dr} << \lambda_{dr} \tag{3-27}$$

$$\frac{L_m}{L_r} = \frac{1}{1 + (L_{lr} / L_m)} \approx 1 \tag{3-28}$$

When the motor is operated at no-load and rated-speed operation, we have

$$\omega_r \approx \omega_e \tag{3-29}$$

$$(R_s + R_r \frac{L_m^2}{L_r^2}) i_{qs} << \omega_r \frac{L_m}{L_r} \lambda_{dr} \tag{3-30}$$

$$V_{ds} << V_{qs} \tag{3-31}$$

The *q*-axis voltage in (3-26) can be approximated based on (3-27) ~ (3-30) as

$$V_{qs} \approx \omega_r \lambda_{dr} \tag{3-32}$$

Then, by (3-31) the peak of the phase voltage can be represented as

$$V_s = \sqrt{V_{ds}^2 + V_{qs}^2} \approx V_{qs} \tag{3-33}$$

Therefore, the approximated value of the rated flux linkage can be simply obtained as the peak of the rated phase voltage divided by the rated angular frequency as follows.

$$\lambda_{dr-\text{rated}} \approx \frac{V_{s-\text{rated}}}{\omega_{r-\text{rated}}} \tag{3-34}$$

where $V_{s\text{-rated}}$ and $\omega_{r\text{-rated}}$ can be easily obtained from the nameplate of the induction machine. Thus, the rated value of the rotor flux linkage can be approximated based on Table 2-3 as

$$\lambda_{dr-\text{rated}} \approx \frac{220 \times \sqrt{2}}{2\pi \times 51.5} \approx 0.9615 \,(\text{Wb}) \tag{3-35}$$

In the steady state, the equation (2-57) can be rewritten by subtituting $s = 0$ as

$$(R_s + \frac{L_s}{L_r} R_r) i_{qs} = V_{qs} - \frac{P}{2} \frac{L_s}{L_m} \omega_m \lambda_{dr} \tag{3-36}$$

In (3-36), $\frac{L_s}{L_m} = 1 + \frac{L_{ls}}{L_m} \approx 1$ holds for the induction motor as previously mentioned, and $i_{qs} \approx 0$ can be assumed at the no-load operation. Then, (3-36) can be simplified as

$$\lambda_{dr} \approx \frac{2V_{qs}}{P\omega_m} \tag{3-37}$$

Based on the above derivation, we may obtain the shaft speed to its rated value at no load by simply adding an outer speed control loop to the present control scheme as shown in Fig. 3-9. Then, by setting different reference of i_{ds}^* and recording q-axis voltage command value (i.e. the output of the PI controller of the q-axis current) with the corresponding rotor speed at the steady state, the value of the rotor flux linkage can thus be estimated by (3-37), and i_{ds}^* for rated flux excitation can finally be determined. Here, the experimental setup is identical to that shown in Fig. 3-4.

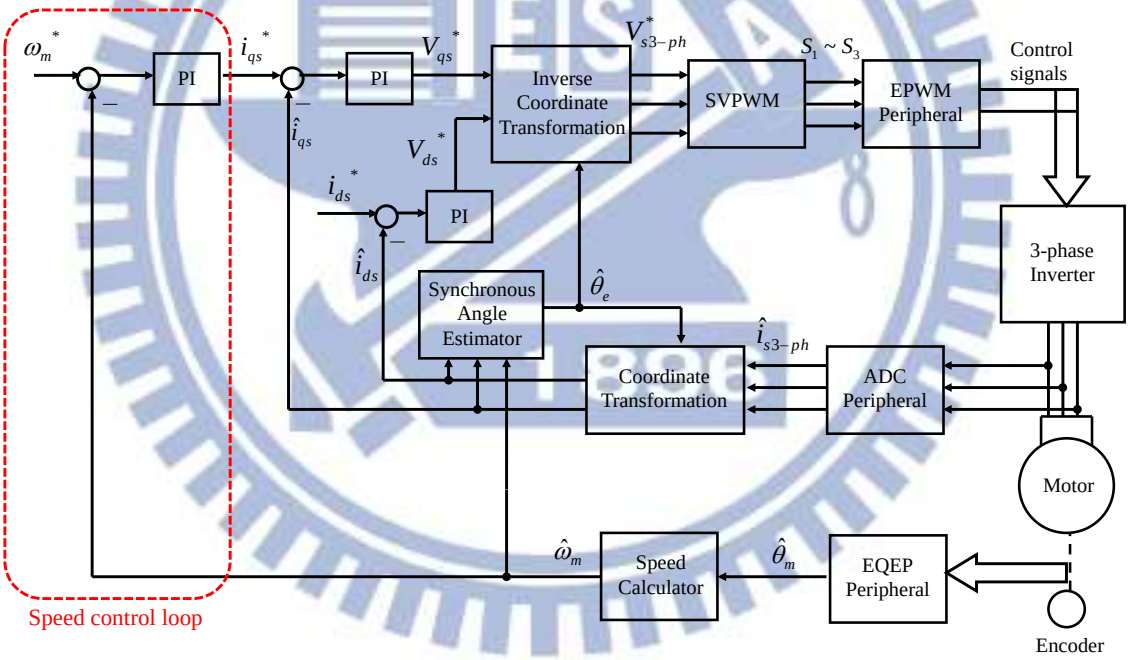

Fig. 3-9 Control diagram of obtaining the rotor flux linkage

Experimental results of the q-axis voltage command value and rotor speed when the d-axis current command value = 0.6 pu is shown in Fig. 3-10.

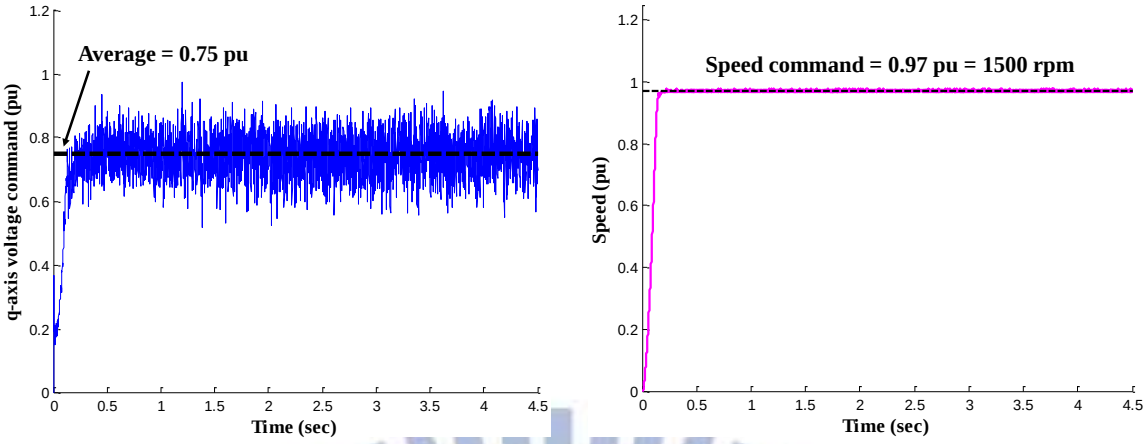

(a) *q*-axis voltage command (b) Speed response

Fig. 3-10 Experimental results of the *d*-axis current command 0.6 pu

In Fig. 3-10, the average value of the *q*-axis voltage command value is 0.75 pu and the rotor speed is equal to its rated value, 1500 rpm. The rotor flux linkage can be approximated by subsituting experimental data into (3-37) as

$$\lambda_1 = \frac{2 \times 0.75 \times 220 \times \sqrt{2}}{4 \times 1500 \times 2\pi / 60} \approx 0.7425 \,(\text{Wb}) \tag{3-38}$$

Note that the unit of ω_m in (3-37) is rad/s. Similarly, the rotor flux linkage under different *d*-axis current command values can be obtained by applying the same process. All experimental results are summarized in Table 3-1.

Table 3-1 Experimental results of obtaining the rotor flux linkage

i_{ds}^* (pu)	V_{qs}^* (pu)	ω_m (rpm)	Estimated rotor flux linkage (Wb)
0.2	0.263	1500	0.26
0.4	0.515	1500	0.51
0.6	0.75	1500	0.7425
0.7	0.86	1500	0.8514
0.8	0.947	1500	0.9375
0.9	1.0	1413.68	1.05
1.0	1.0	1354.2	1.0974
1.2	1.0	1234.15	1.2035
1.4	1.0	1160.45	1.28
1.6	1.0	1111	1.338
1.8	1.0	1068.52	1.39
2.0	1.0	1035.77	1.434

Obviously, when i_{ds}^* is larger than 0.9 pu, the motor can no longer be regulated at the rated speed due to V_{qs}^* reaches the maximum supplied voltage of the drive as seen from Table 3-1. However, the rotor flux linkage can still be obtained by (3-37). The curve of the rotor flux linkage versus the i_{ds}^* is depicted as Fig. 3-11 based on Table 3-1.

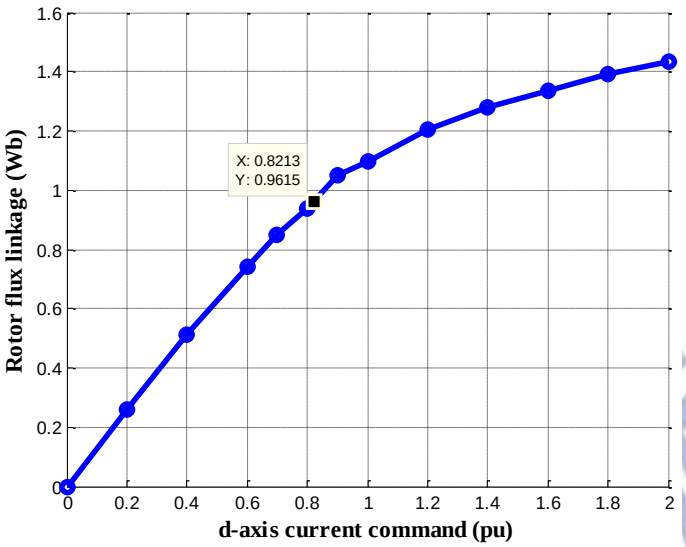

Fig. 3-11 Experimental results of obtaining the rotor flux linkage

Previously, we have already approximated the rated rotor flux linkage as 0.9615 Wb as (3-35). Hence, the command value of the *d*-axis current exciting rated rotor flux linkage can be obtained simply by applying the interpolation as 0.82 pu, as shown in Fig. 3-11. It can also be discovered that flux saturation becomes more significant if the *d*-axis current is larger than 0.82 pu. To compare speed response of the rated flux excitation with that of equal *d*-*q* current command based on (3-16), we again apply the experimental setup as shown in Fig. 3-8(a) and set i_s^* = 1.623, 2.094, and 2.576 pu, respectively. Results are plotted as in Fig. 3-12.

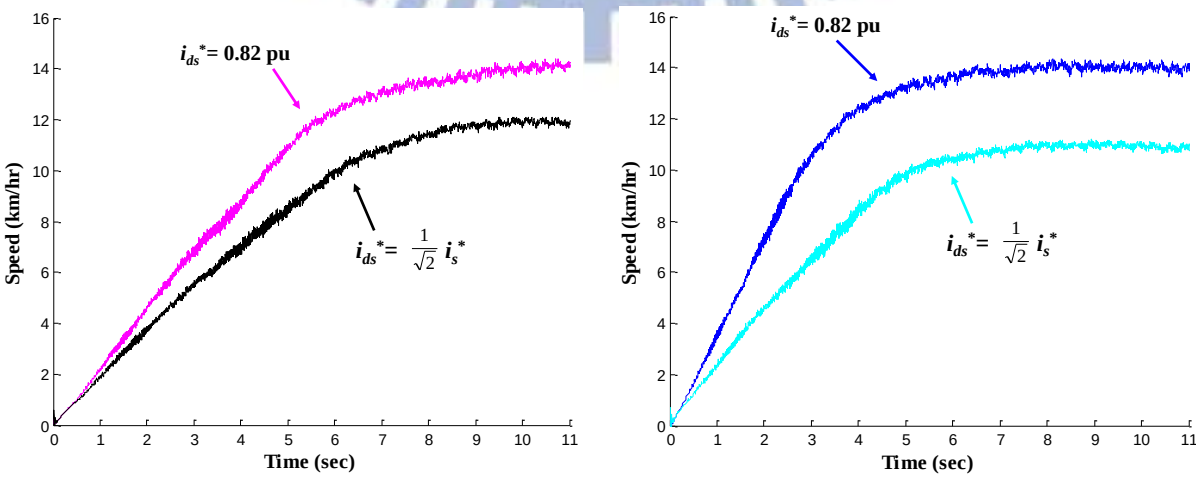

(a) (b)

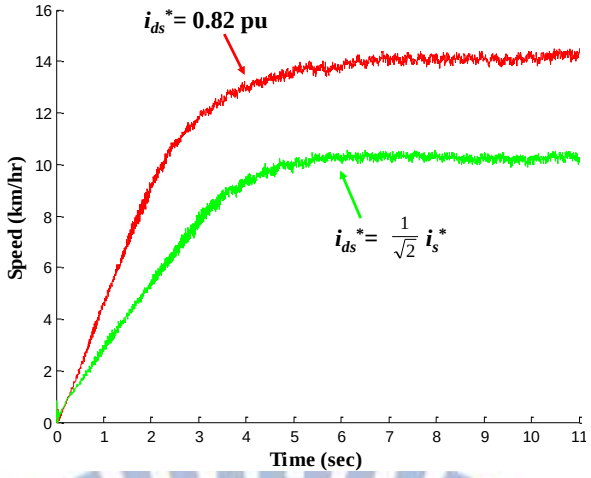

(c)

Fig. 3-12 Speed responses with the rated flux excitation: (a) i_s^* = 1.623 pu (b) i_s^* = 2.094 pu (c) i_s^* = 2.576 pu

As shown in Fig. 3-12, when the rotor flux linkage of the motor is operated at the rated value 0.82 pu, both the acceleration and final speed are significantly improved. Specifically, the acceleration time from 0 to 10 km/hr can be shortened by at least two seconds. Comparison of the acceleration of the induction machine based on these two approaches is shown in Fig. 3-13. The range of improvement becomes larger with increase of i_s^* due to severe flux saturation with the equal *d-q* current command setting.

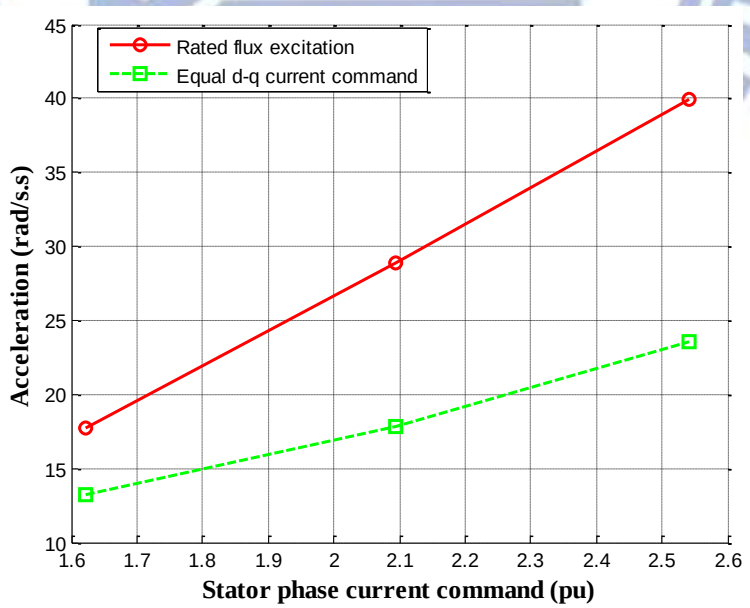

Fig. 3-13 Comparison of acceleration of the rated flux excitation and the equal *d-q* current command

3.2.3 Experimental verification of the MTPA

In order to verify the operation of MTPA, a standard experimental process as shown in Fig. 3-14 for testing acceleration of the induction machine on the vehicle is established as follows.

- A student with 65 kg is seated on the vehicle for driving. The total weight of the system is approximately 145 kg.
- The vehicle is driven along a 75-m straight path.
- The control scheme shown in Fig. 2-22 is utilized. However, the function of the accelerator is temporarily disabled and the stator current command, i_s^*, is step with 1.623, 2.094, and 2.576 pu, separately.
- Acceleration is calculated as the average value as the *q*-axis current begins to decrease as described in Section 3.1.2.
- Since the rotor time constant is sensitive to the temperature, three minutes for heat dissipation are applied between experiments.

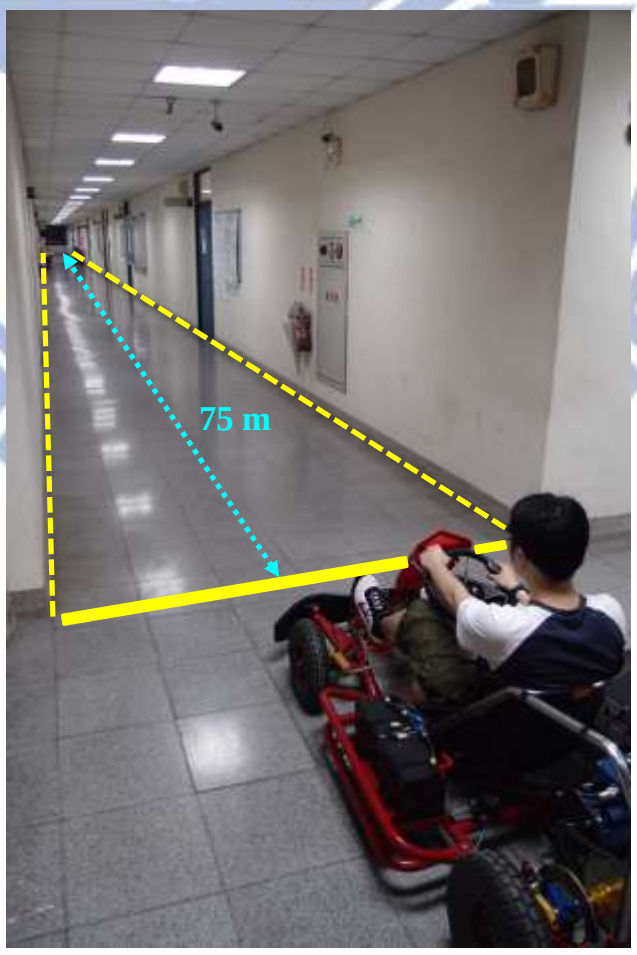

Fig. 3-14 Setup of the standard experimental process

Experimental results with different operating i_{ds}^* is shown in Fig. 3-15. Note that the maximum acceleration can be obtained by setting flux-producing current as 0.82 pu, so the actual MTPA operation is indeed achieved when the rotor flux linkage is excited at the rated value. On the other hand, the acceleration is quite low by equally setting *d*-*q* axis current as expected. Thus, 0.82 pu is chosen for i_{ds}^* to achieve the maximum acceleration of the vehicle at given i_s^*.

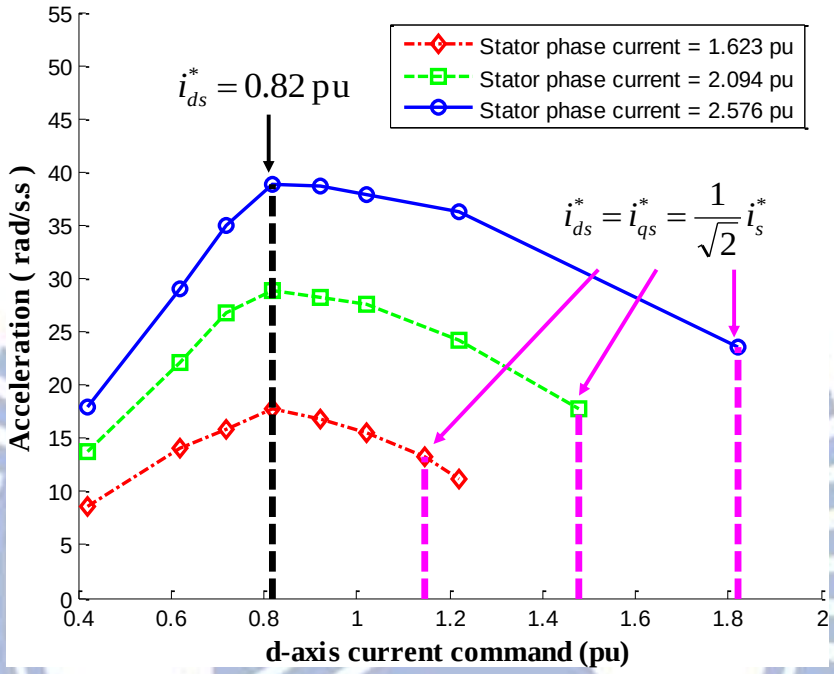

Fig. 3-15 Acceleration with different operated i_{ds}^*

3.3 The Highest Efficiency Operation

In addition to the maximal acceleration, issues of operating efficiency for the induction machine will also addressed in the electric vehicle application. The operating efficiency in this study is defined as

$$\eta = \frac{T_L \omega_m}{V_{dc} I_d} \times 100\% \tag{3-39}$$

The numerator of the equation is the mechanical output power of the motor, which is the rotational speed ω_m, multiplied by the load torque T_L. The denominator is the electrical input power of the inverter, formed by the product of the DC-bus voltage and the total supplied current amount to the power switches as shown in Fig. 3-16. Note that the efficiency is computed at steady-state, i.e. the system is operated at a constant speed ω_m.

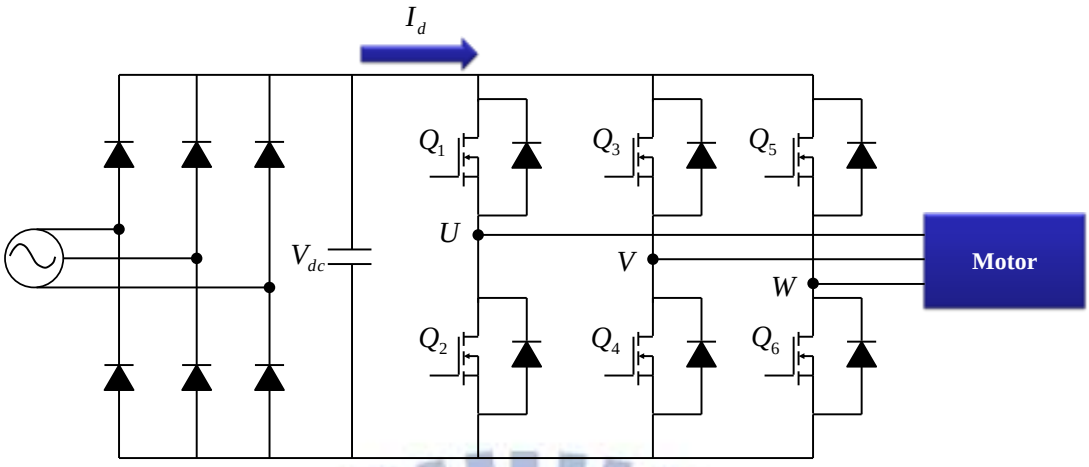

Fig. 3-16 Illustration of the input power of the inverter

Despite the terms ω_m, V_{dc}, and I_d can be obtained by reading their correpsonding sensors, T_L, which is basically composed of the rolling resistance of the wheels and the aerodynamic force, is unknown because of the absence of torque sensor in the system. However, T_L can be assumed as fixed due to the following two reasons [15].

(1) Experiments are carried out with the same conditions as shown in Fig. 3-14. Although the rolling resistance is influenced by the vehicle speed, the contribution of the speed-dependent term is negligibly small, i.e. the rolling resistance effect can be assumed as fixed.

(2) Vehicle speed is always kept less than 20 km/hr in the experiments, and the aerodynamic force in such condition is much smaller than the rolling resistance.

Besides, DC-bus voltage is well-regulated by the power stage module, and thus it can also be assumed as fixed. Therefore, we adopt an efficiency coefficient in place of the real efficiency specified by (3-39) as

$$\kappa = \frac{\omega_m}{I_d} \tag{3-40}$$

Similarly, evaluations of efficiency with different i_{ds}^* are launched based on (3-40) directly on practical driving conditions following the standard experimental process. Their results are shown in Fig. 3-17.

The maximum efficiency is not exacly known, because the corridor where the experiments were performed is not sufficiently long for observation of speed in steady-state when i_{ds}^* is less than 0.42 pu, and their efficiency coefficients cannot be accessed. However, the highest operating efficiency of the induction machine can be obtained when i_{ds}^* = 0.42 pu based on the present experiments. Table 3-2 summarizes the acceleration and efficiency coefficient when i_{ds}^* = 0.42 and 0.82 pu, separately.

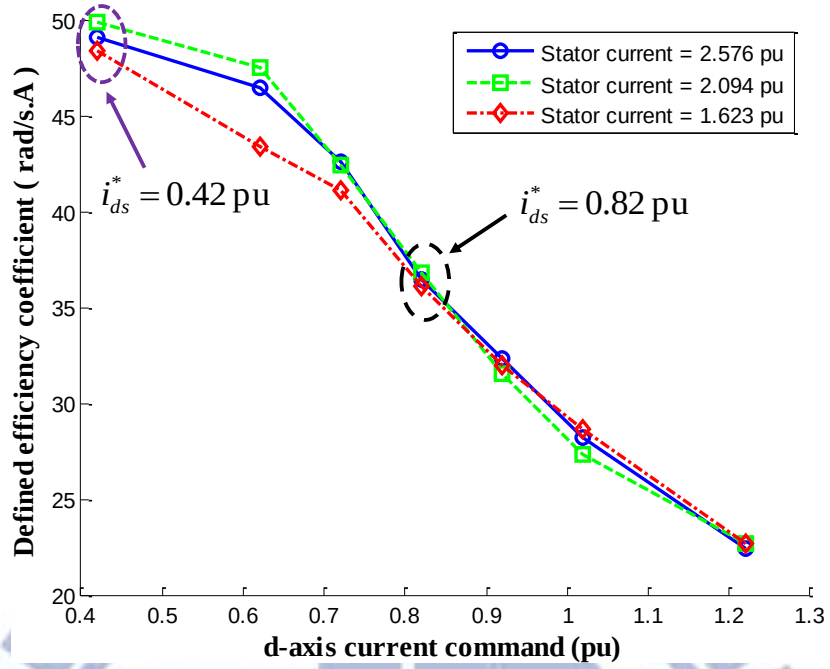

Fig. 3-17 Efficiency coefficient with different operated i_{ds}^*

Table 3-2 Comparison of operations with i_{ds}^* = 0.42 and 0.82 pu

	Acceleration (rad/s^2)		Efficiency coefficient (rad/s.A)		Final speed (km/hr)	
	$i_{ds}^* = 0.82$ pu	$i_{ds}^* = 0.42$ pu	$i_{ds}^* = 0.82$ pu	$i_{ds}^* = 0.42$ pu	$i_{ds}^* = 0.82$ pu	$i_{ds}^* = 0.42$ pu
$i_s^* = 1.623$ pu	17.69	8.54	36.13	49.12	14.2	21.42
$i_s^* = 2.094$ pu	28.88	13.77	36.82	49.84	13.98	21.55
$i_s^* = 2.576$ pu	38.92	17.95	36.47	48.4	14.12	21.4

Note that performance of the induction motor is determined by the operating flux current, which has been already described in Section 2.3.3. When i_{ds}^* is set as 0.82 pu, the maximum torque per amperage operation can be achieved, and thus the acceleration is maximal as shown in Fig. 3-15. However, its efficiency coefficient is merely around 36 rad/s.A, and the final speed of the vehicle is restricted to 14 km/hr. On the other hand, the highest operating efficiency is obtained when i_{ds}^* = 0.42 pu as indicated in Fig. 3-17, and meanwhile the final speed can reach more than 21 km/hr due to relatively low back-emf caused by lower flux excitation. However, acceleration of the vehicle in such condition is quite limited. Actual speed responses of the vehicle in these two cases are shown in Fig. 3-18.

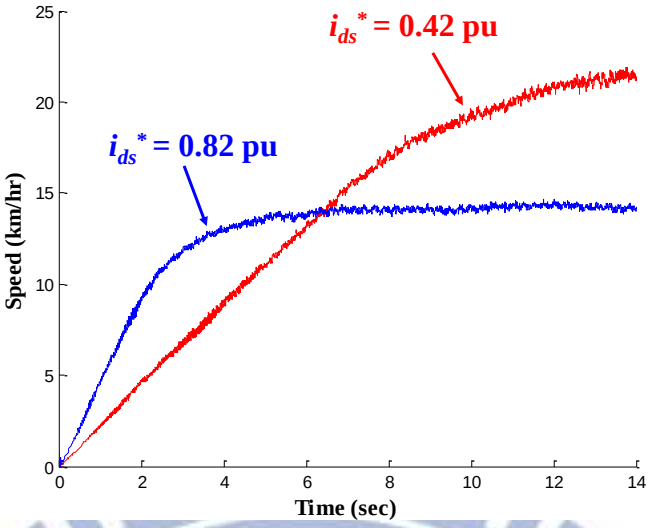

Fig. 3-18 Speed response of the vehicle when i_{ds}^* = 0.42 pu and 0.82 pu

Thus, the following control strategy is encouraged to accomplish both the maximum acceleration and the highest operating efficiency:

(1) During start-up period, where large torque is required to overcome the rolling resistance, the system is operated at the MTPA to provide suitable acceleration for the vehicle, i.e. i_{ds}^* can be set as 0.82 pu as shown in Fig. 3-15.

(2) As the speed has significantly increased, the system is then switched to the operation with the highest efficiency for energy saving, i.e. i_{ds}^* can be set as 0.42 pu as shown in Fig. 3-17.

As a result, a switching mechanism of the operating flux of the induction machine is necessary for the control requirement. Detailed design and verification will be demonstrated in the next chapter.

3.4 Summary

In this chapter, the high performance servo control of the induction machine implemented on the electric vehicle is developed to satisfy the maximum acceleration capability and the highest operating efficiency. Present achievements are summarized as follows.

(1) Successfully identify the rotor time constant of the induction machine

Rotor time constant is employed in the calculation of the synchronous angle estimator in the indirect vector control, and the traditional no-load test and locked-rotor test is not easy to implement on the vehicle. A precise identification process that can be directly performed on the vehicle is developed to obtain the

rotor time constant as 0.08 s.

(2) The maximum torque per amperage operation is obtained by applying the rated flux excitation

Conventional approach of equal *d-q* current command is unsuitable for the vehicle application in this study, in which severe flux saturation of the machine is caused and the MTPA operation is thus lost. Alternatively, the maximum torque can be obtained when the rotor flux linkage is exited at the rated value proved by the standard experimental process, and the acceleration of the machine can be improved by 65.5% with such arrangement when the maximal stator current is supplied (i_s^* = 2.576 pu) as shown in the following table.

Table 3-3 Comparison of the equal *d-q* current command and the rated flux excitation (i_s^* = 2.576 pu)

Control method	Acceleration (rad/s^2)	Efficiency coefficient (rad/s.A)	Final speed (km/hr)
Equal *d-q* current command	23.51	13.35	10.2
Rated flux excitation (i_{ds}^* = 0.82 pu)	38.92	36.47	14.7
Improvement	**65.5%**	**173.2%**	**44.1%**

(3) The highest efficiency is obtained with proper flux current setting

The highest operating efficiency of the machine is directly found by practical driving following the standard experimental process as i_{ds}^* = 0.42 pu. Despite of weaker acceleration ability, the efficiency coefficient at such operating point can be further increased to 48.4 rad/s.A when the maximal stator current is supplied as shown in Table 3-4.

Table 3-4 Comparison of the rated flux excitation and the highest efficiency operation (i_s^* = 2.576 pu)

Control method	Acceleration (rad/s^2)	Efficiency coefficient (rad/s.A)	Final speed (km/hr)
Rated flux excitation (i_{ds}^* = 0.82 pu)	38.92	36.47	14.7
The highest efficiency operation (i_{ds}^* = 0.42 pu)	17.95	48.4	21.4
Improvement		**32.7%**	**45.6%**

Chapter 4

Design of the Optimal Switching Mechanism

In this chapter, the idea of designing a switching mechanism of the operating flux of the induction machine for achieving both the maximum torque and the highest operating efficiency will be developed to meet control specifications of the electric vehicle. We first propose the slip factor adjustment, γ-adjustment, for a smooth characteristic of the vehicle application. Then, the switching strategy that automatically adjusts the operation accoring to the driving conditions to satisfy the requirement is designed based on the proposed γ-adjustment.

4.1 Slip Factor Adjustment (γ-Adjustment)

First of all, we define a slip factor, γ, in the slip frequency calculation such that

$$\hat{\omega}_{slip} = \frac{1}{\gamma}\frac{1+p\hat{\tau}_r}{\hat{\tau}_r}\frac{\hat{i}_{qs}}{\hat{i}_{ds}} \tag{4-1}$$

Note that the defined slip factor is unity in general indirect vector control as seen from (3-4). As stated in Section 3.1.1, the rotor time constant of the induction machine is much smaller than the mechanical constant of the vehicle. Hence, the equation (4-1) can be rewritten by substituting $p = 0$ as referred to the mechanical system as

$$\hat{\omega}_{slip} = \frac{1}{\gamma}\frac{1}{\hat{\tau}_r}\frac{\hat{i}_{qs}}{\hat{i}_{ds}} \tag{4-2}$$

By substituting (3-9) into (4-2) and substituting (3-10) into (3-2), we obtain

$$\hat{\omega}_{slip} = \frac{1}{\gamma}\frac{1}{\hat{\tau}_r}\tan\alpha \tag{4-3}$$

$$\omega_{slip} = \frac{1}{\tau_r}\tan\beta \tag{4-4}$$

Then, equate (4-3) and (4-4) with the constraint of current closed-loop control indicated in (3-7), and the following equation is derived:

$$\tan\beta = \frac{1}{\gamma}\frac{\tau_r}{\hat{\tau}_r}\tan\alpha \tag{4-5}$$

With the developed rotor time constant identification described in Section 3.1.2, the estimated rotor time constant $\hat{\tau}_r$ can be obtained as close to the actual value τ_r. Thus, the equation (4-5) can be simplified as

$$\tan\beta = \frac{1}{\gamma}\tan\alpha \tag{4-6}$$

Relationship between the feedback and actual *d*-*q* axis currents flowing into the induction machine can be depicted based on (4-6) as shown in Fig. 4-1.

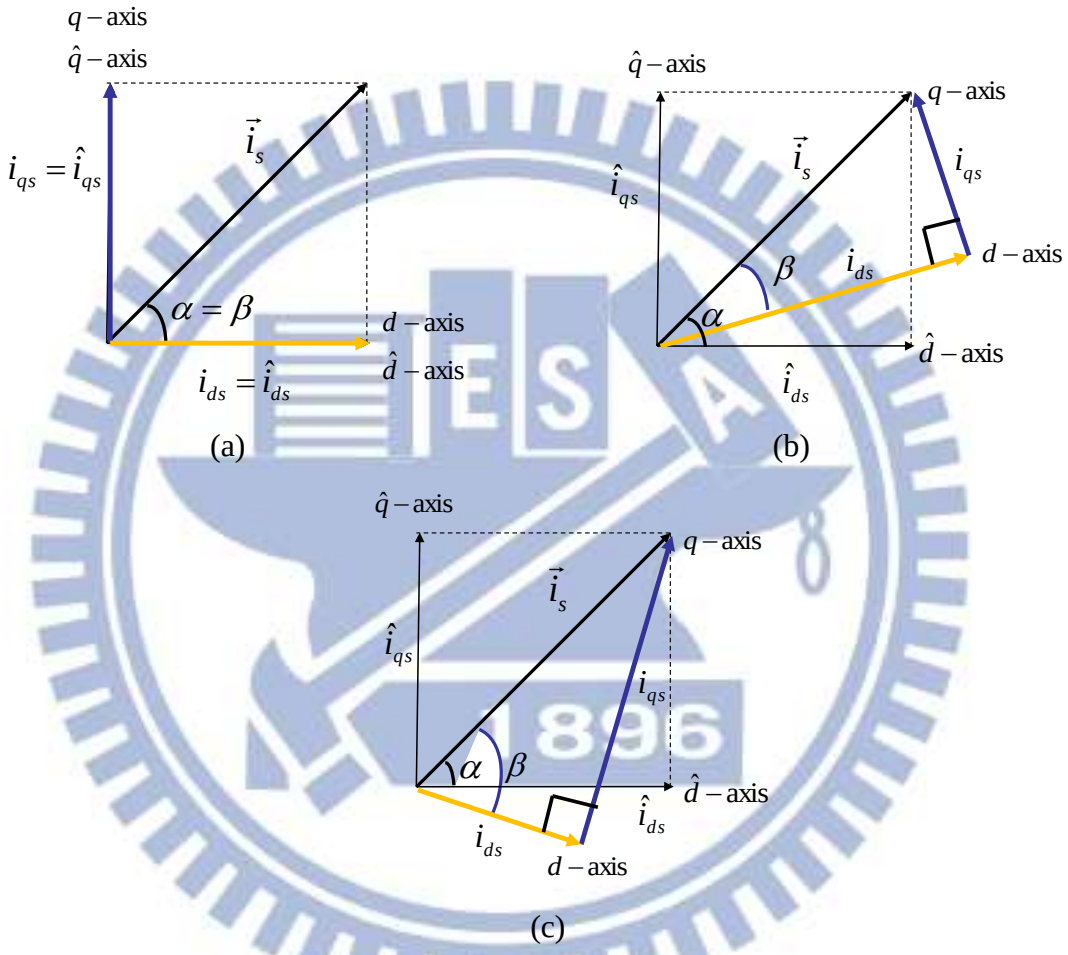

Fig. 4-1 Relationship between the estimated and actual d-q axis currents when (a) $\gamma = 1$, (b) $\gamma > 1$, and (c) $\gamma < 1$

When γ = 1, the actual current is equal to the estimated or feedback value on both axes. This is what general indirect vector control is applied. If γ > 1, β will be larger than α, and the actual *q*-axis current flowing into the motor is smaller than its feedback while the actual *d*-axis current is larger than the feedback one. On the other hand, β will be smaller than α when γ < 1. In this case, the actual *q*-axis current is larger than its feedback while the actual *d*-axis current is smaller than the feedback. Obviously, by adjusting γ while keeping the current commands as the same magnitude, the actual *d*-*q* axis current can also be altered.

The first merit of such adjustment is that the maximum torque per amperage and the highest efficiency operation can still be obtained by properly setting γ even if i_{ds}^* is not originally set at both optimal operating points. To verify its validity, we intentionally set i_{ds}^* as 0.62 pu, which is neither the operation of the maximum torque per amperage nor the operation of the highest efficiency, and obtain γ correpsonding to these two operations through the standard experimental process developed in Section 3.2.3 and 3.2.4. Experimantal results are shown in Fig. 4-2 and 4-3.

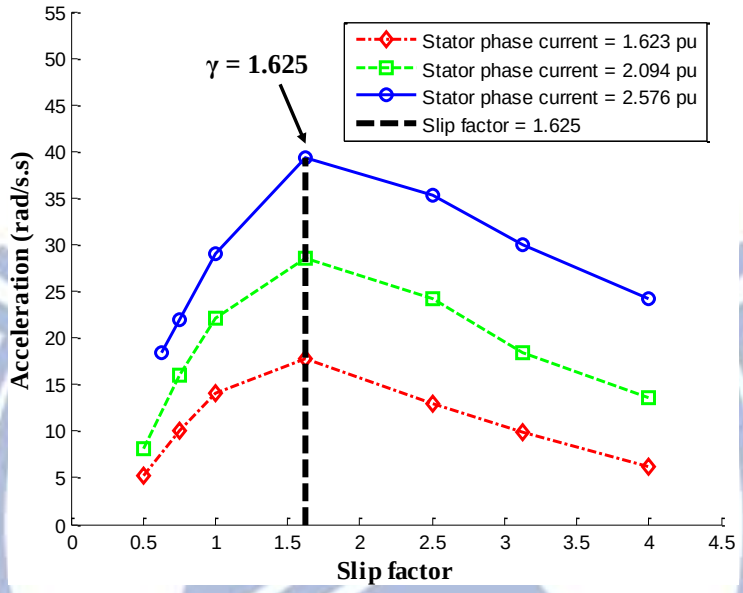

Fig. 4-2 Acceleration with different γ (i_{ds}^* = 0.62 pu)

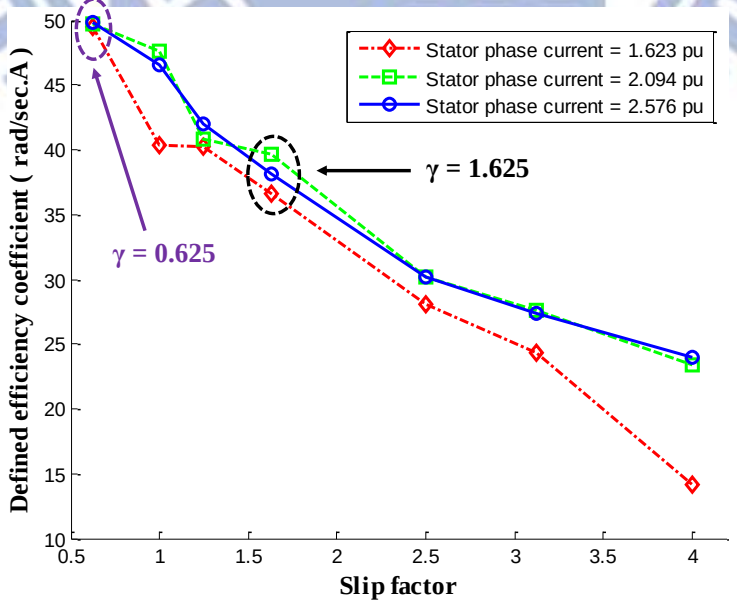

Fig. 4-3 Efficiency coefficient with different γ (i_{ds}^* = 0.62 pu)

From the above experimental results, it can be identified that the system has the maximum acceleration when γ = 1.625 to achieve the maximum torque per amperage operation. Additionally, the highest efficiency operation can be obtained with γ = 0.625. Data of the acceleration and efficiency coefficient when γ = 1.625 and 0.625 are summarized in Table 4-1.

Table 4-1 Comparison of acceleration and efficiency

	Acceleration (rad/s^2)		Efficiency coefficient (rad/sec.A)	
	$\gamma = 1.625$	$\gamma = 0.625$	$\gamma = 1.625$	$\gamma = 0.625$
$i_s^* = 1.623\,\text{pu}$	17.61	7.638	36.63	49.47
$i_s^* = 2.094\,\text{pu}$	28.71	12.08	39.66	49.7
$i_s^* = 2.576\,\text{pu}$	39.27	18.36	38.11	49.88

Therefore, even though the flux current is not correctly operated at the maximum torque per amperage (i_{ds}^* = 0.82 pu with γ = 1) and the highest efficiency operation (i_{ds}^* = 0.42 pu with γ = 1), both of them can still be obtained by setting γ as 1.625 and 0.625 when i_{ds}^* = 0.62 pu, respectively, as shown in Table 4-1.

The approach that sets i_{ds}^* = 0.82 pu to obtain the maximum torque per amperage operation and sets i_{ds}^* = 0.42 pu to obtain the highest efficiency operation with γ = 1 is performed by different settings of i_{ds}^*. To distinguish this approach from the proposed γ-adjustment, we specifically denominate it as i_{ds}^*-adjustment. Speed responses of the vehicle with the maximum torque per amperage (MTPA) operation obtained by the i_{ds}^*-adjustment and the γ-adjustment are compared in Fig. 4-4(a), and comparison between the highest efficiency (HE) operation obtained by the i_{ds}^*-adjustment and the γ-adjustment is shown in Fig. 4-4(b). Both two figures are obtained with the maximum supplied stator current, i.e. i_s^* is 2.576 pu. Their acceleration and efficiency coefficient are listed in Table 4-2.

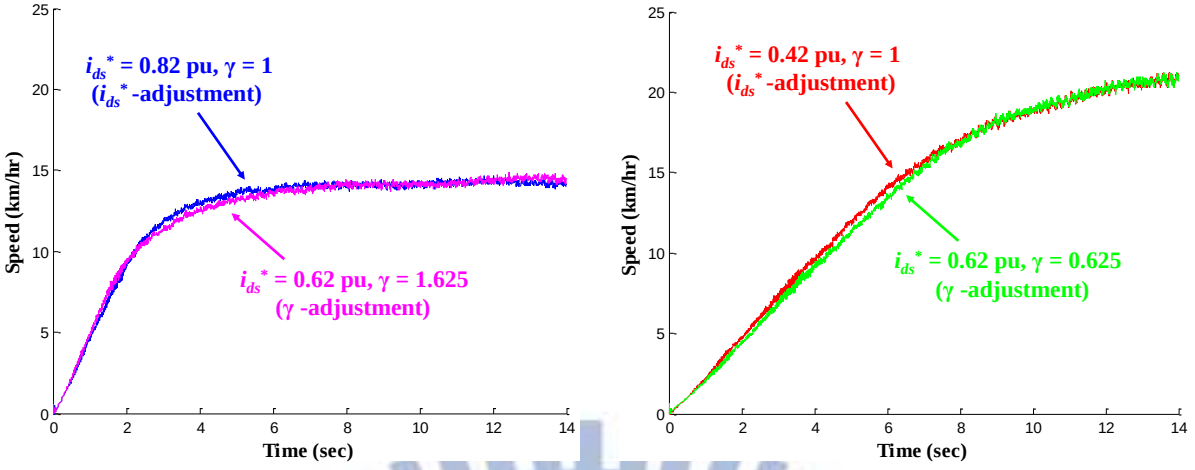

(a) MTPA operation (b) HE operation

Fig. 4-4 Comparison of the speed response obtained by the i_{ds}^*-adjustment and the γ-adjustment

Table 4-2 Comparison of the i_{ds}^*-adjustment and the γ-adjustment (i_s^* = 2.576 pu)

Operation	Approach	Operating Condition	Acceleration (rad/s^2)	Efficiency coefficient (rad/s.A)
MTPA	i_{ds}^*-adjustment	$i_{ds}^* = 0.82\,\text{pu}$ and $\gamma = 1$	38.92	36.47
	γ-adjustment	$i_{ds}^* = 0.62\,\text{pu}$ and $\gamma = 1.625$	39.27	38.11
HE	i_{ds}^*-adjustment	$i_{ds}^* = 0.42\,\text{pu}$ and $\gamma = 1$	17.95	48.4
	γ-adjustment	$i_{ds}^* = 0.62\,\text{pu}$ and $\gamma = 0.625$	18.36	49.88

Consequently, we can conclude that among the following four operating points:

- i_{ds}^*-adjustment
  (1) i_{ds}^* = 0.82 pu with γ = 1
  (2) i_{ds}^* = 0.42 pu with γ = 1
- γ-adjustment
  (3) i_{ds}^* = 0.62 pu with γ = 1.625
  (4) i_{ds}^* = 0.62 pu with γ = 0.625

(1) and (3) obtains equivalent maximum torque per amperage operation, while (2) and (4) obtains the identical operation of the highet efficiency.

4.2 Comparison between the γ-Adjustment and the i_{ds}^*-Adjustment

It can be recognized that the decoupled control will be modified by the γ-adjustment as seen from Fig. 4-1, which indicates that the operating flux will no longer be constant while changing the *q*-axis current, and torque ripples may be generated due to varied flux as stated in [26]. However, the ripples can be filtered out in the vehicle application because the mechanical time contant is far larger than the rotor time constant. In order to verify it, we have launched three sets of experiments in which ramp stator current commands with different slopes are fed into the system. Fig. 4-5 shows the patterns of the ramp stator current commands as:

(1) Slope1 = 2.576 pu/s

(2) Slope2 = 1.0304 pu/s

(3) Slope3 = 0.5752 pu/s

Vehicle speed response corresponding to (1) ~ (3) operated at the maximum torque per amperage by the i_{ds}^*-adjustment (i_{ds}^* = 0.82 pu with γ = 1), and the γ-adjustment (i_{ds}^* = 0.62 pu with γ = 1.625) are compared in Fig. 4-6(a) ~ (c), respectively.

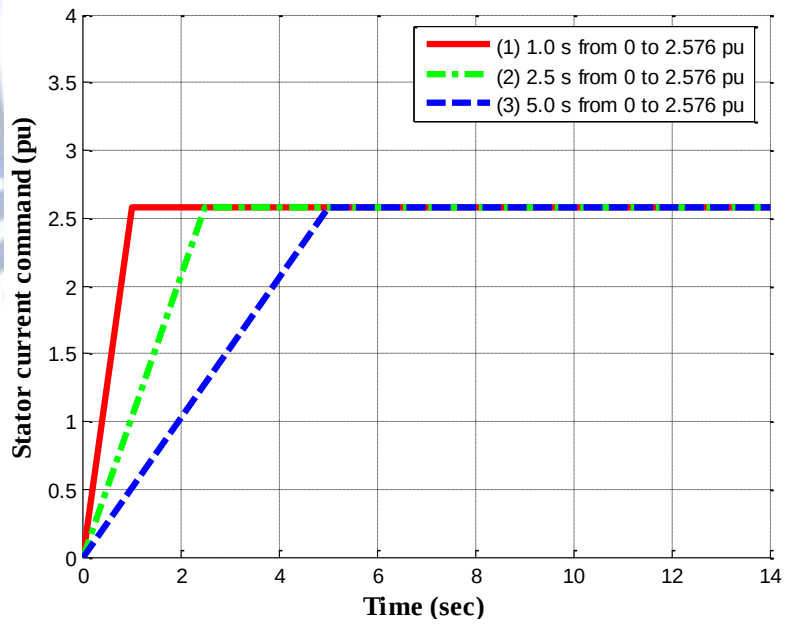

Fig. 4-5 Three stator current commands applied for the verification of torque ripples

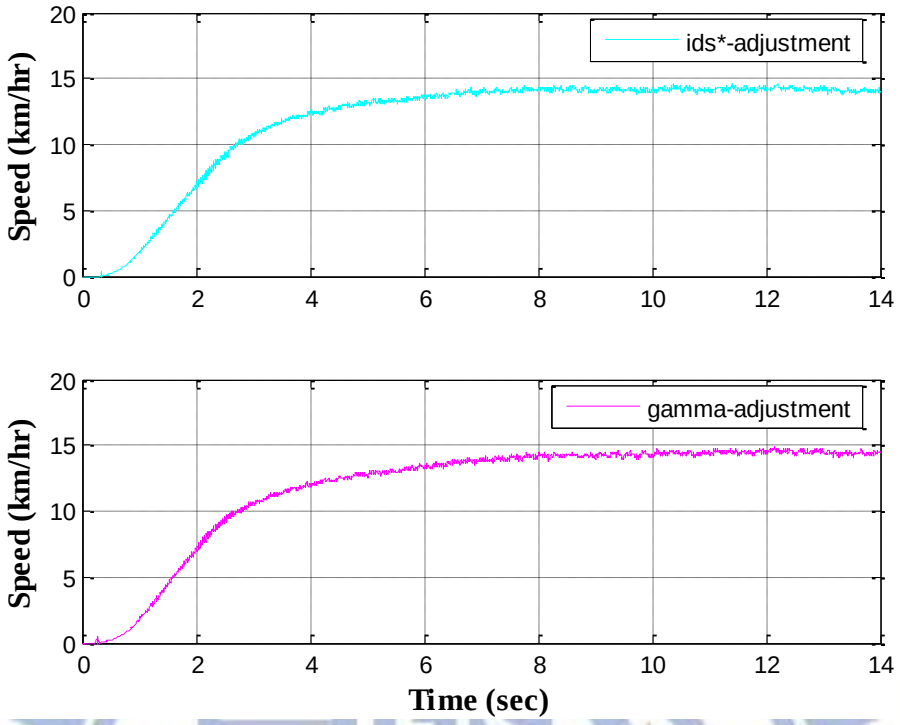

(a) The ramp stator current command with slope 1

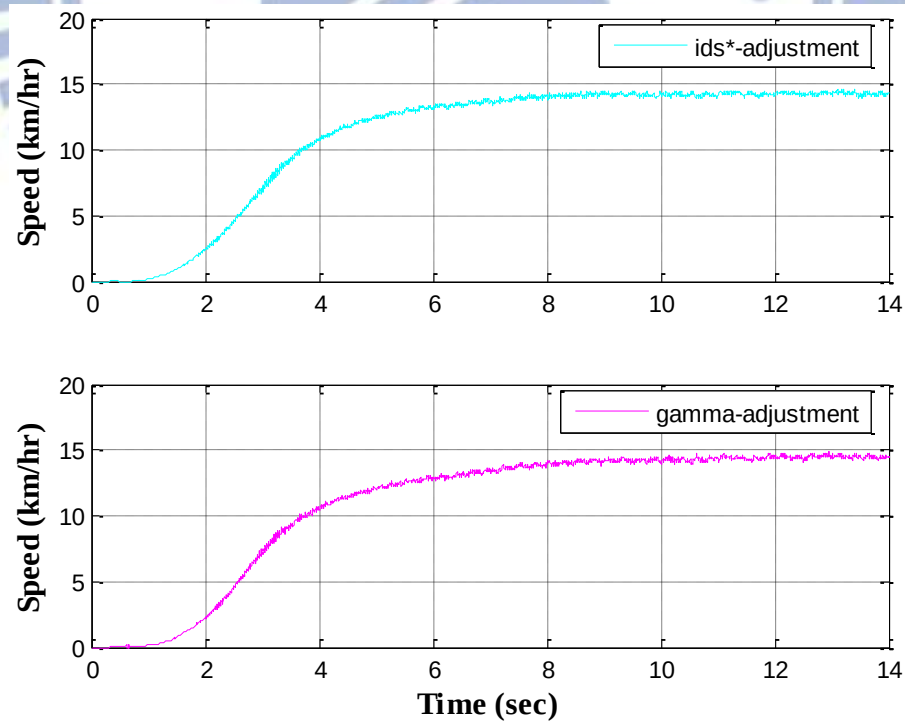

(b) The ramp stator current command with slope 2

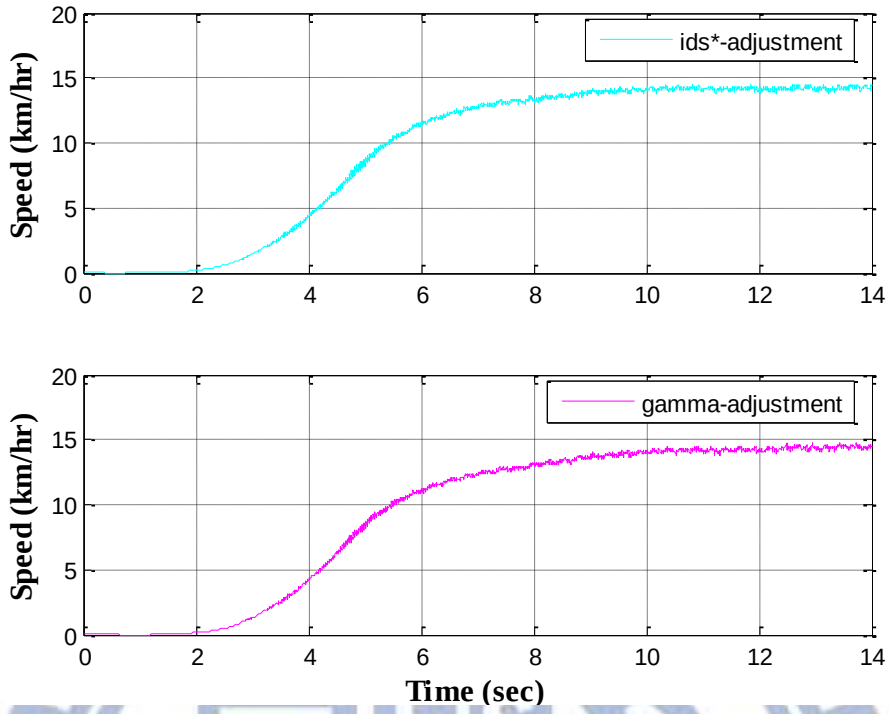

(c) The ramp stator current command with slope 3

Fig. 4-6 Comparison of the vehicular speed response operated at the maximum torque per amperage by the ids*-adjustment and the γ-adjustment

As seen from Fig. 4-6, torque ripples are eliminated by the system with large mechanical time constant in the experiments, since no ripples are present in the practical speed response with the γ-adjustment. In fact, with the results shown in Fig. 4-6 we can also prove that the operation with i_{ds}^{*} = 0.82 pu and γ = 1 and the operation with i_{ds}^{*} = 0.62 pu with γ = 1.625 are equivalent to each other once again.

Then, to further investigate the difference between the i_{ds}^{*}-adjustment and the γ-adjustment, operation with the maximum toruqe per amperage and that with the highest efficiency are switched back and forth with i_{s}^{*} = 2.576 pu step command for testing. The patterns of the testing switching process between these two operations for the i_{ds}^{*}-adjustment and the γ-adjustment are shown in Fig. 4-7. Note that γ is kept as unity and i_{ds}^{*} is switched between 0.42 pu and 0.82 pu when the i_{ds}^{*}-adjustment is applied, while i_{ds}^{*} is kept as 0.62 pu and γ is switched between 1.625 and 0.625 when the γ-adjustment is applied in the testing process. Experimental results are shown in Fig. 4-8.

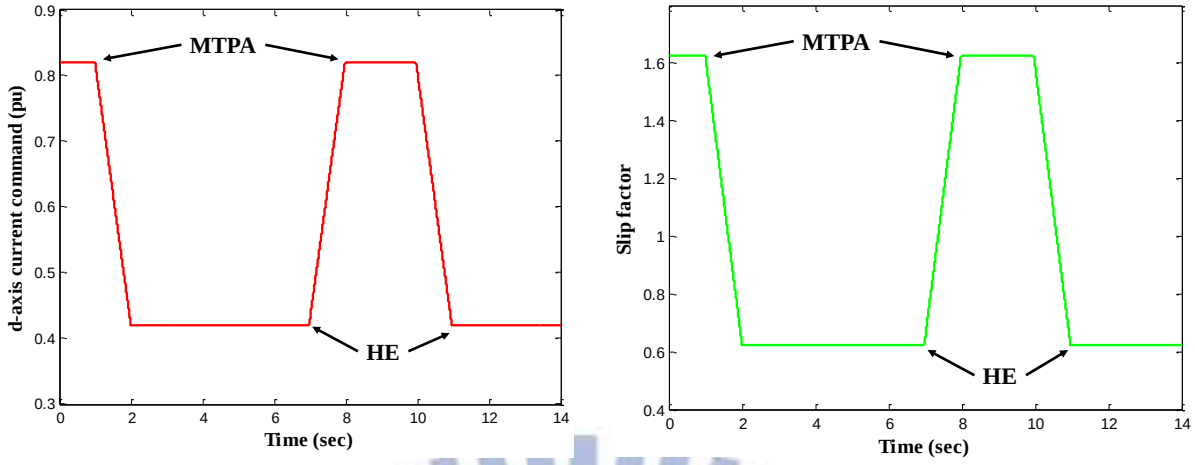

(a) (b)

Fig. 4-7 Patterns of the testing switching process between the MTPA and the HE: (a) i_{ds}^{*}-adjustment and (b) γ-adjustment

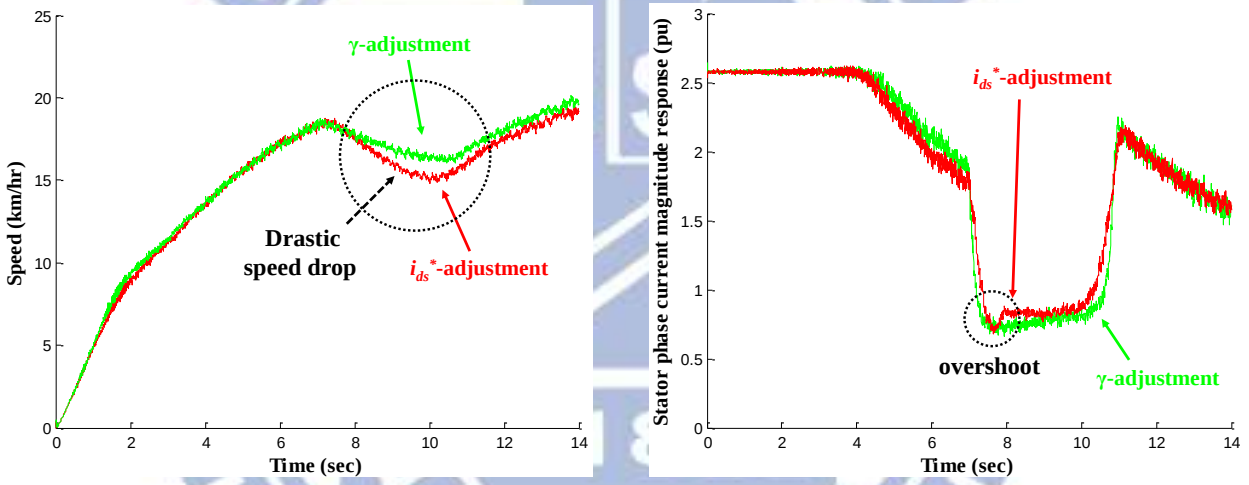

(a) Speed response (b) Stator current magnitude response

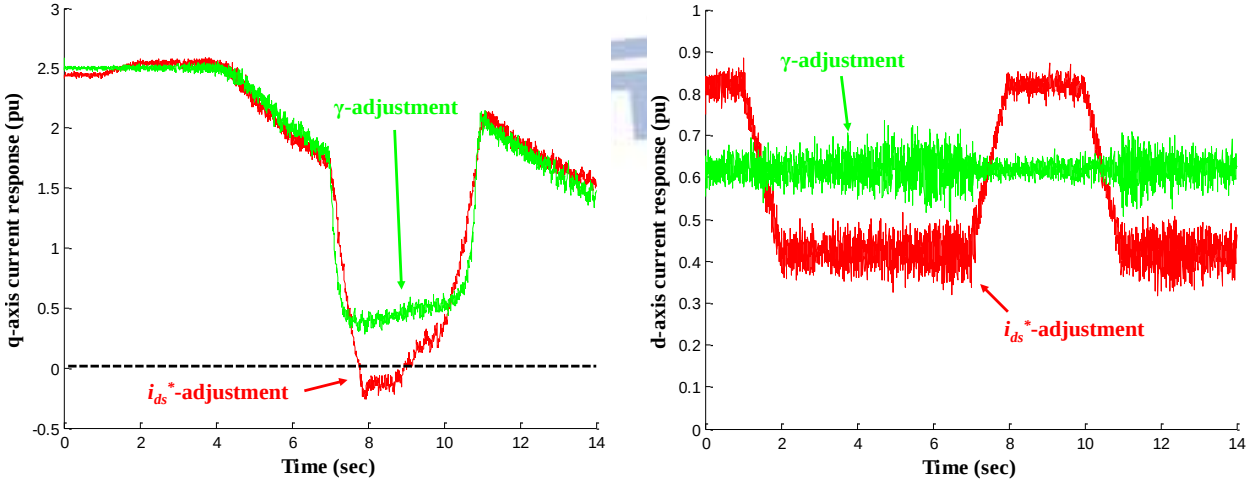

(c) *q*-axis current response (d) *d*-axis current response

Fig. 4-8 Results of the testing switching process obtained by the i_{ds}^{*}-adjustment and the γ-adjustment

As seen from Fig. 4-8, the operation of the currents of the γ-adjustment is smoother than that of the i_{ds}^*-adjustment with the given switching process. Particularly in the time interval between the 7th second and the 10th second, the *q*-axis currents of both approaches decrease significantly since the rotor flux linkage and thus the back-emf constant becomes stronger when the operation is switched from the HE to the MTPA. It can be noticed that the *q*-axis current response of the i_{ds}^*-adjustment instaneously drops to negative values, indicating torque with the opposite direction is developed. This phenomenon can be detected as well from its own speed response, where drastic speed drop occurs and causes more uncomfortable driving experience, as shown in Fig. 4-8(a). On the other hand, the *q*-axis current value of the γ-adjustment is always positive regardless of the varied operations, and the torque will always be of the forward direction. Accordingly, the γ-adjustment yields smoother operating performance that is more applicable to traction control of the electric vehicle when the switching machanism is applied. This is the second merit of the γ-adjustment approach.

4.3 Switching Strategy for Both the MTPA and the HE Operation

4.3.1 Design of the switching strategy

It has been already verified in the previous section that the γ-adjustment possesses relatively smooth driving performance with the switching machanism. Therefore, the γ-adjustment is applied as the basis of the switching strategy designed for obtaining both the maximum acceleration and the highest efficiency.

As far as the traction control of electric vehicle is concerned, it is desirable to meet the following two characteritics:

(1) High torque for starting and at low speeds

(2) High efficiency for high-speed cruising

Based on the fact, we can first determine speed thresholds for the operations. Fig. 4-9 shows the speed response obtained by the γ-adjustment with the maximum supplied stator current when the induction machine is operated at the MTPA and the HE. The designed switching strategy that can automatically adjust γ according to driving conditions is also illustrated in the figure. The definitions of three operations specified based on two speed threshold values, 10 and 15 km/hr, in the strategy are shown in Table 4-3.

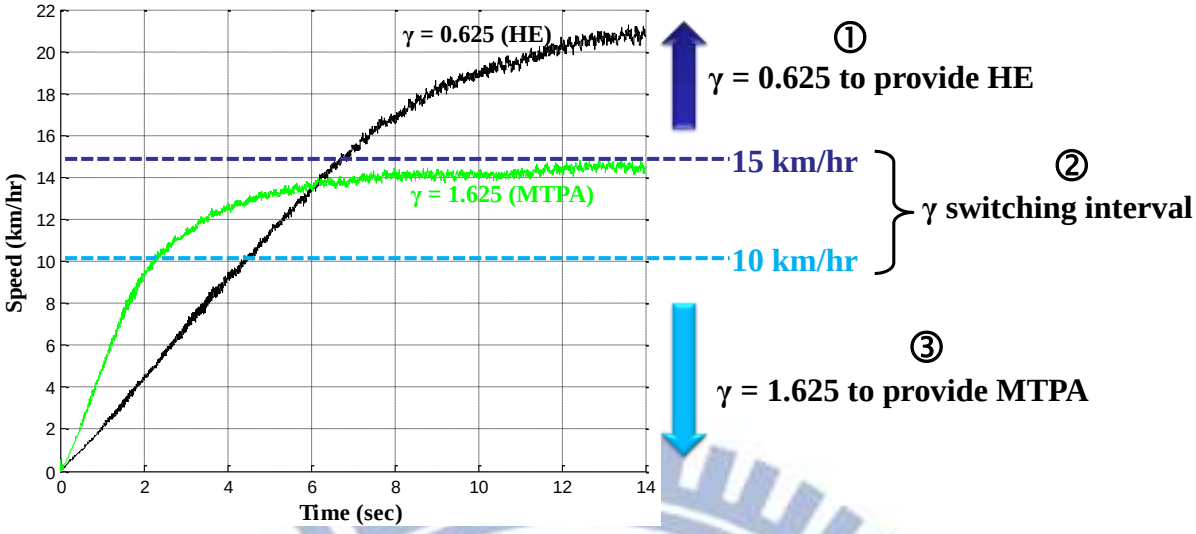

Fig. 4-9 Illustration of the designed switching strategy for γ

Table 4-3 Definition of three operations in the switching strategy

Specified operation	Definition	Description	Setting
Operation 1	High speed	Speed > 15 km/hr	γ = 0.625
Operation 2	Medium speed	Speed = 10~15 km/hr	γ = 0.625~1.625
Operation 3	Low speed	Speed < 10 km/hr	γ = 1.625

In practical driving, the supplied stator current magnitude is determined by the accelerator in the system, and thus the *q*-axis current command may intensely vary. Nonetheless, the mechanical time constant of the system is very large so that the variation of the vehicle speed acts much slower than that of the current. As a result, it is quite sufficient to check driving conditions just every second for the switching strategy as shown in Fig. 4-10.

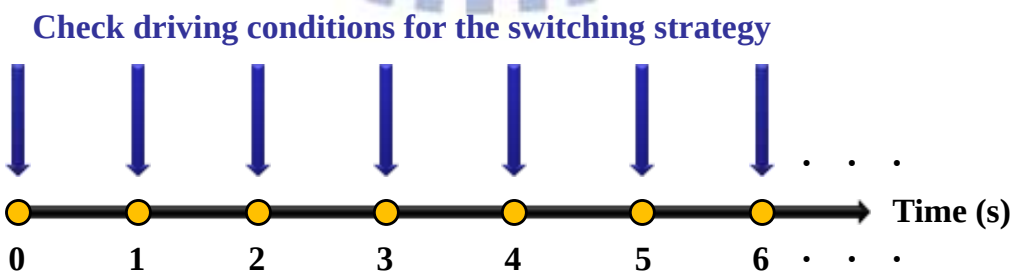

Fig. 4-10 Illustration of driving-condition checking of the switching strategy

When γ = 1.625, it is obvious that the increasing rate of the speed response becomes smaller and smaller if the speed continues to increase after reaching 10 km/hr, and the speed will gradually converge to a final cruising speed value. Thus, the first speed threshold is set at 10 km/hr. When the speed is smaller than this value, it is defined as the low-speed operation (operation 3). During this operation, γ is always kept as 1.625 for providing the maximum torque.

Furthermore, 15 km/hr is determined as the second speed threshold such that operation with speed larger than 15 km/hr is defined as the high-speed operation (operation 1) while operation with speed lying between 10 and 15 km/hr is specified as the medium speed operation (operation 2). In operation 1, γ will be kept as 0.625 to obtain the highest efficiency.

Finally, there are four possibilities for the behavior of γ in the defined γ-switching interval, i.e. operation 2:

(1) γ is switched from 1.625 to 0.625 within 1 s
(2) γ is switched from 0.625 to 1.625 within 1 s
(3) γ is 0.625
(4) γ is 1.625

The notion of the strategy design for this operation is descriped as follows: In general, the driver will keep stepping on the accelerator pedal deeply in an attempt for acceleration if one senses that the vehicle is currently slow. Contrarily, if the driver considers that the present vehicle speed is too high, the accelerator will be shallowly stepped on so that the speed is going to slow down. The vehicle tends to operate at a high speed in the former case while it tends to be operated at a low speed in the latter case. Hence, the driving commands set by the accelerator, i.e. the commands of the supplied stator current magnitude, i_s^*, can be employed for a criterion to determine which action among (1) ~ (4) will be applied as shown in Fig. 4-11.

In the present implementation, we specify 1.5 pu as the theshold value of i_s^*. After operation 2 is confirmed, the system will check if i_s^* is larger than the threshold. If it is true, γ will be switched from 1.625 to 0.625 within 1 s when γ is currently not 0.625; otherwise γ will be maintained as 0.625. If i_s^* is smaller than the threshold, γ will be switched from 0.625 to 1.625 within 1s when γ is not 1.625 at present, or γ will be maintained as 1.625. The flow chart and the block diagram of overall control program of the system including the switching strategy implemented on the DSP controller are shown in Fig. 4-12 and 4-13, respectively.

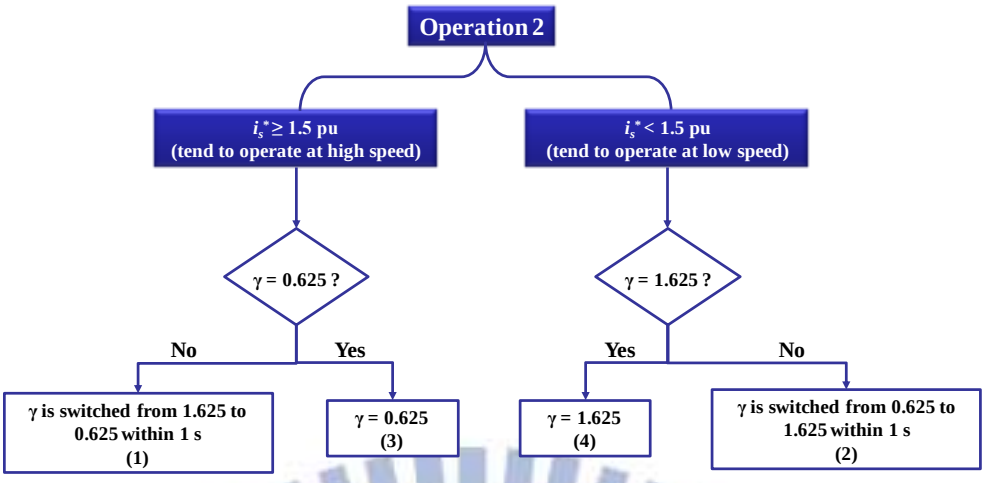

Fig. 4-11 Classification of actions applied in operation 2

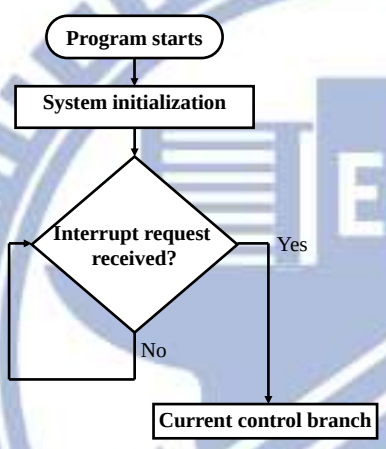

(a) Main program

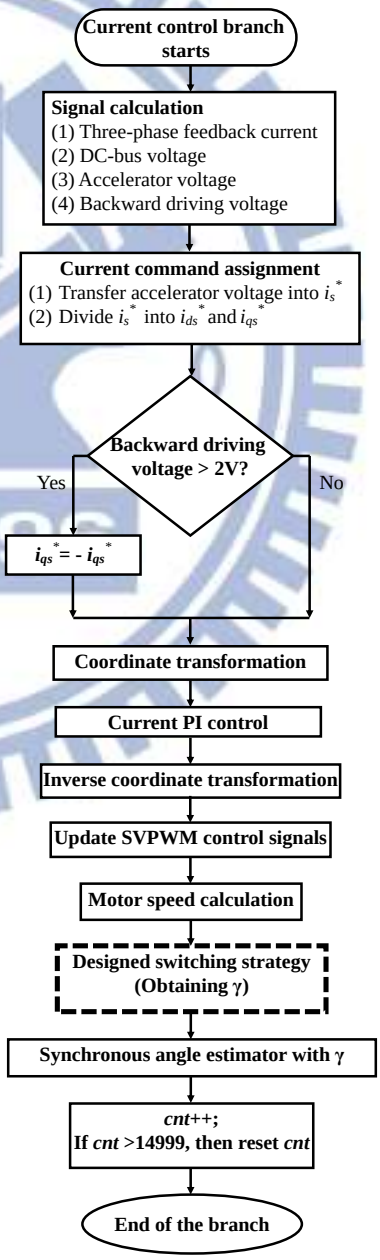

(b) Current control branch

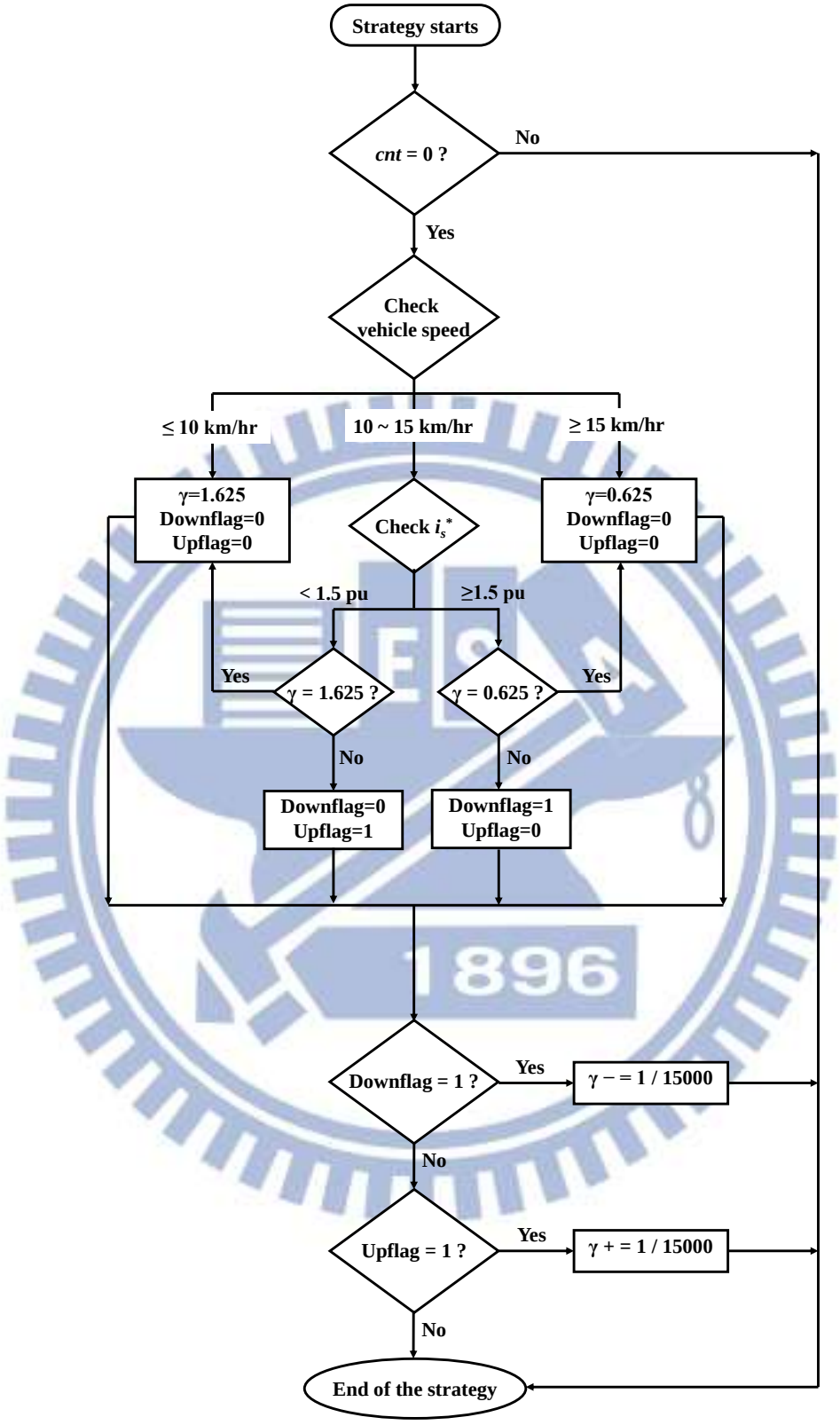

(c) Designed switching strategy for obtaining γ

Fig. 4-12 Flow chart of overall control program including the switching strategy

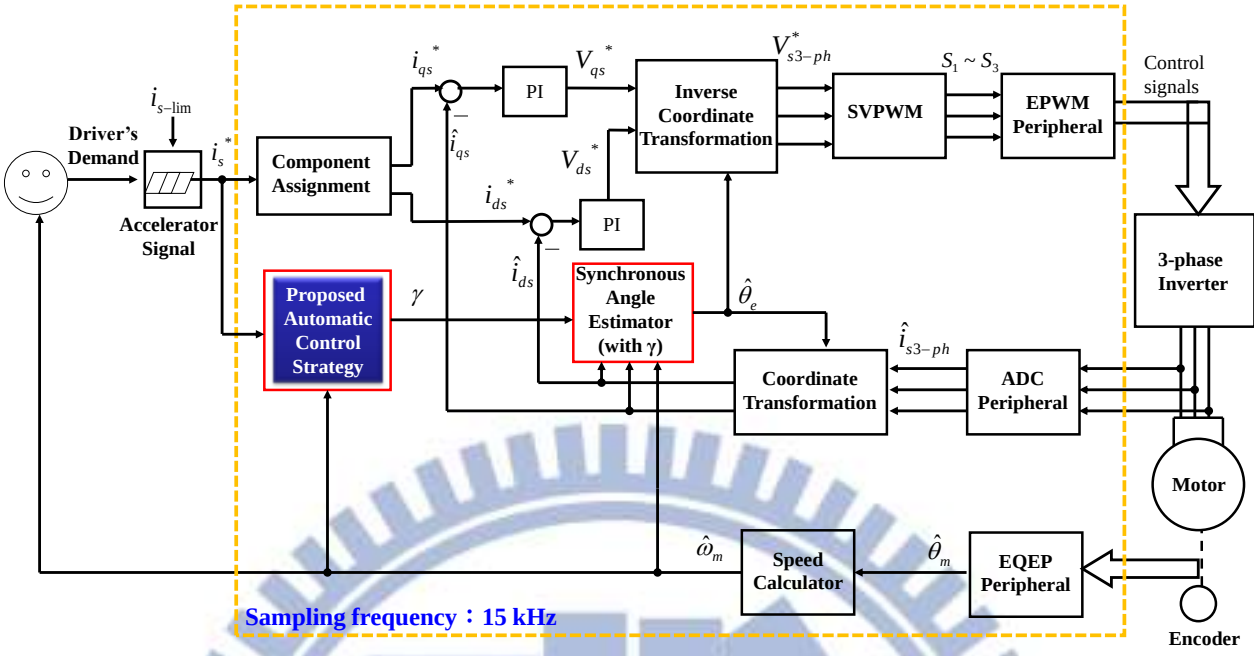

Fig. 4-13 Block diagram of overall control program implemented on the DSP controller

As shown in Fig. 4-12(b), a counter, *cnt*, is plus one every time when the current control branch is executed, and it will be reset to zero as long as its value is larger than 14999. Since the interrupt frequency of the system is 15 kHz, the conditional statement evaluating whether *cnt* is equal to zero, as illustrated in Fig. 4-12(c), is used to implement condition checking every second of the switching strategy. Besides, the actions where γ −= 1/15000 and γ += 1/15000 indicate that γ is switched from 1.625 to 0.625 within 1 s and γ is switched from 0.625 to 1.625 within 1 s, respectively.

4.3.2 Experimental verification of the designed strategy

To verify that the designed switching strategy is effective, we have performed various experiments with practical driving conditions. The first one was carried out with step 2.576 pu of i_s^*, and operation with MTPA only, HE only, and the designed switching strategy are compared in Fig. 4-14 and Table 4-4.

As seen from Fig. 4-14 and Table 4-4, operation with the switching strategy possesses both charateristics of MTPA (γ = 1.625) and HE (γ = 0.625) as: At start-up of the vehicle, the system is operated at the MTPA so that the maximum acceleration can be obtained. Then, the system is switched to the HE operation for higher efficiency and final speed as the speed increases until it exceeds 10 km/hr.

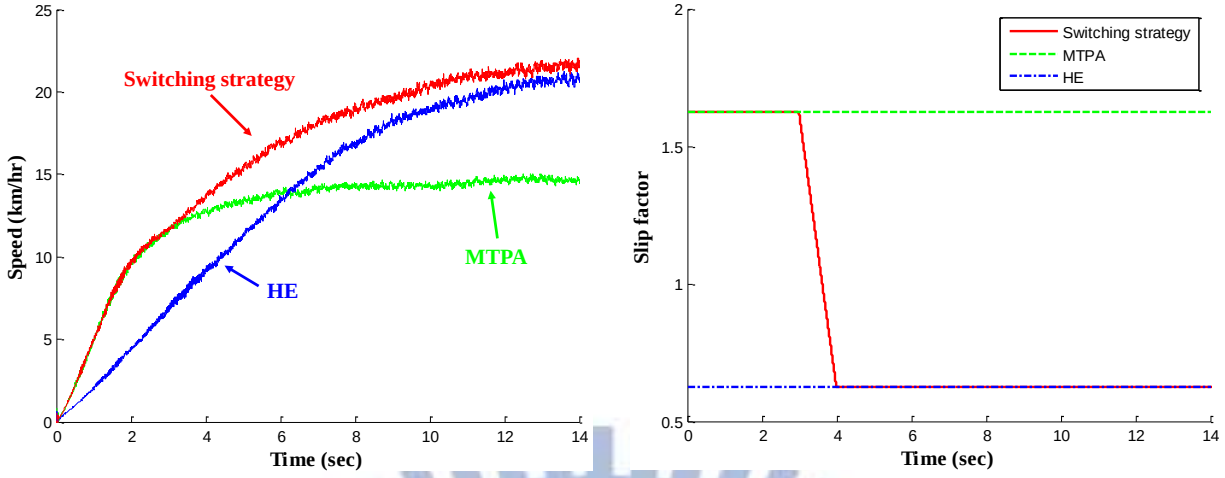

(a) Speed response (b) γ

Fig. 4-14 Experimental results of operation with the MTPA, the HE, and the switching strategy

Table 4-4 Comparison of with the MTPA, the HE, and the switching strategy

Operation	Operating Condition	Acceleration (rad/s^2)	Efficiency coefficient (rad/s.A)	Final speed (km/hr)
MTPA only	γ = 1.625	39.27	38.11	14.7
HE only	γ = 0.625	18.36	49.88	21.6
Switching strategy	γ is automatically adjusted	**39.27**	**49.88**	**21.6**

The second experiment for the verification was launched such that the driver can step on the pedal as one wants to control the vehicle. Results of control schemes with and without the switching strategy are shown in Fig. 4-16 and 4-15, respectively. When the vehicle is driven without the switching strategy, the maximum acceleration can be obtained since γ is set as 1.625 to provide the MTPA. However, Fig. 4-15 (c), (d), (i), and (j) exhibit that the vehicle speed is limited to approximately 14.7 km/hr no matter how large the command i_s^* is fed. The reason is that strong rotor flux linkage is excited when the system is operated at the MTPA and it causes large back-emf. From the results shown in Fig. 4-3 we also know that the efficiency at such an operation is not desirable.

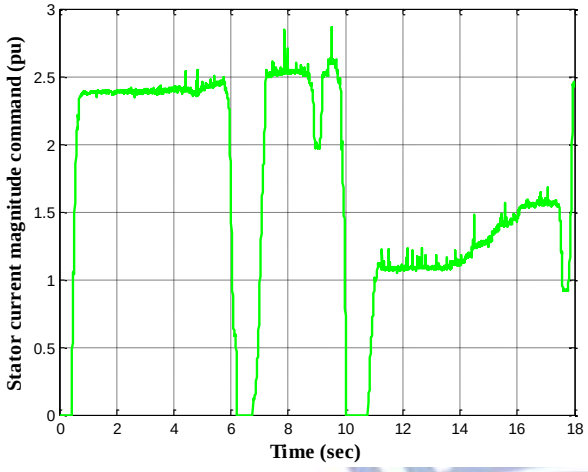

(a) i_{s1}^*

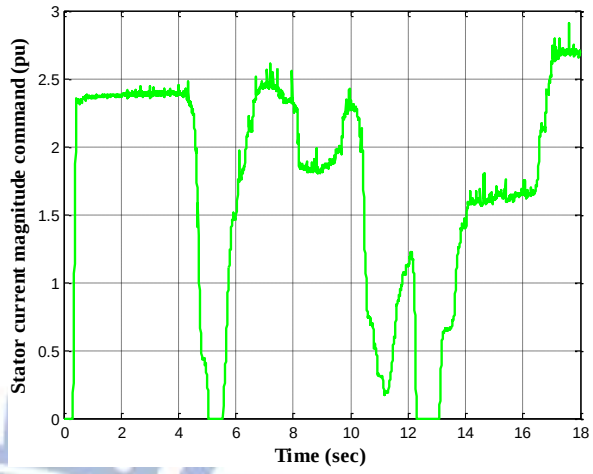

(b) i_{s2}^*

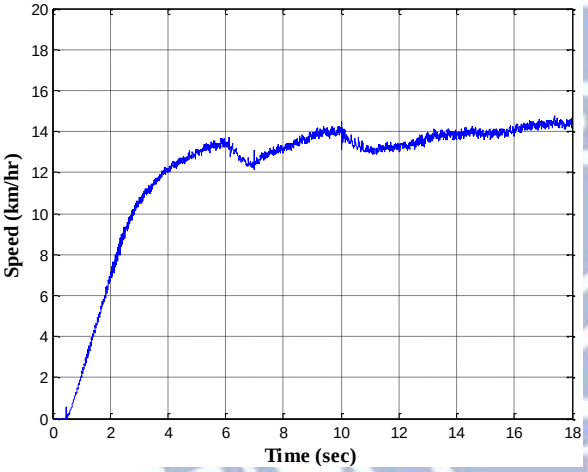

(c) Speed response with i_{s1}^*

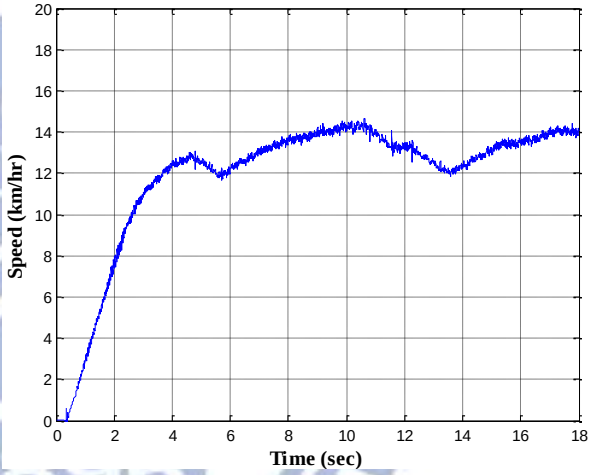

(d) Speed response with i_{s2}^*

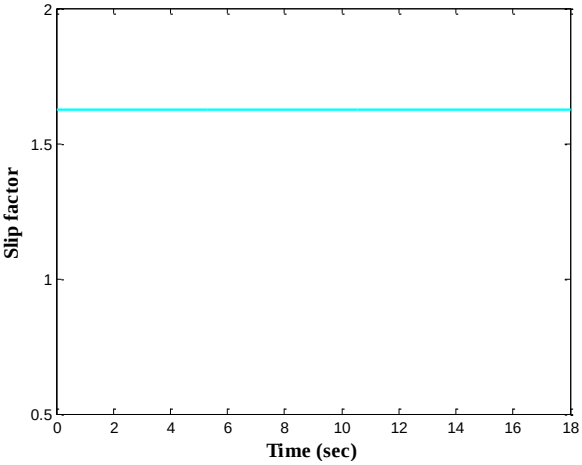

(e) γ with i_{s1}^*

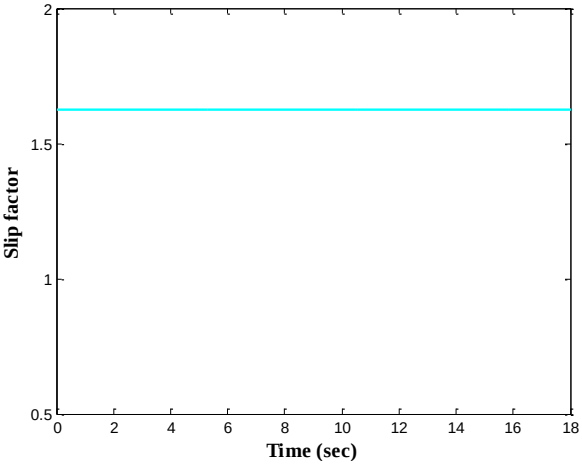

(f) γ with i_{s2}^*

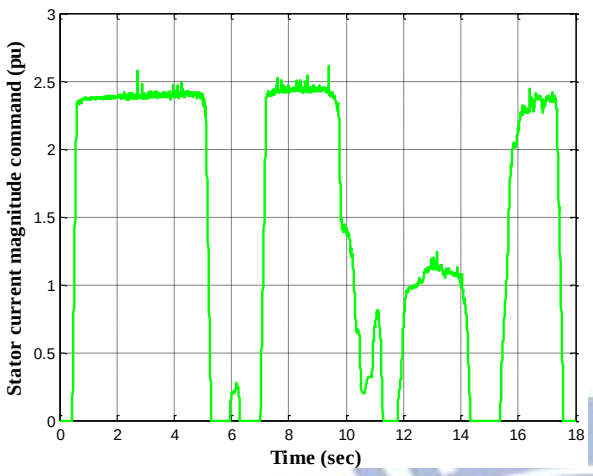

(g) i_{s3}^{*}

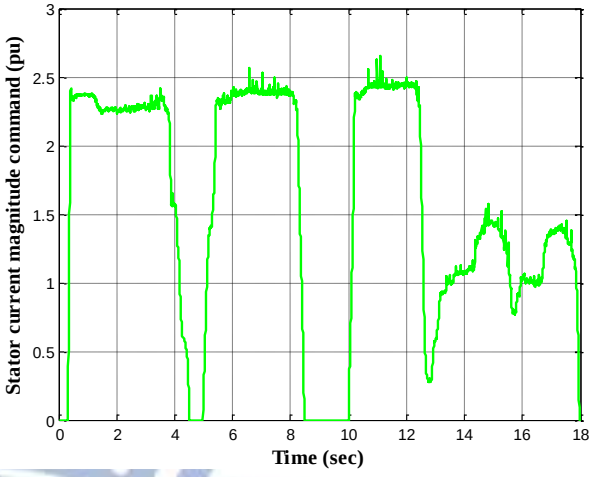

(h) i_{s4}^{*}

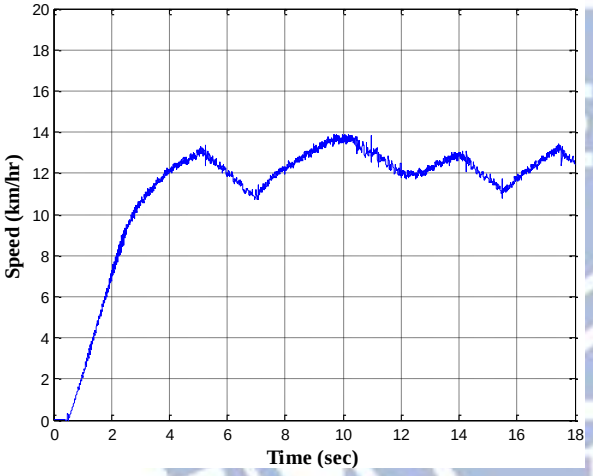

(i) Speed response with i_{s3}^{*}

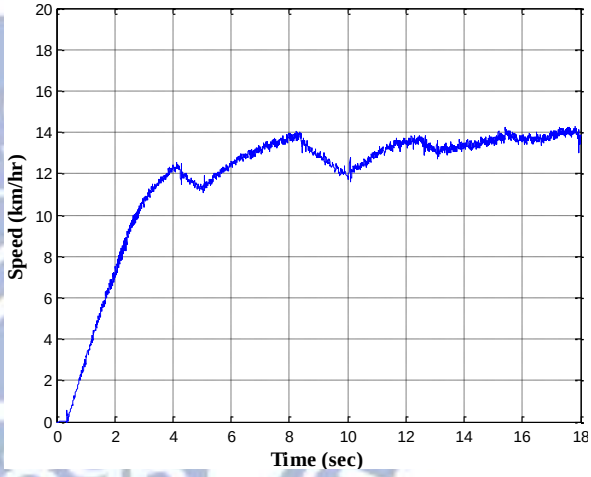

(j) Speed response with i_{s4}^{*}

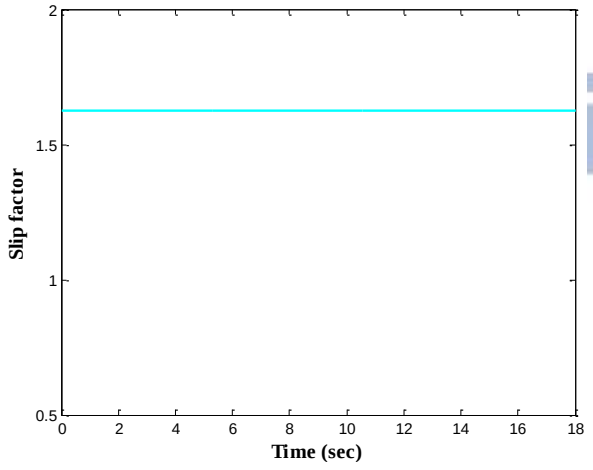

(k) γ with i_{s3}^{*}

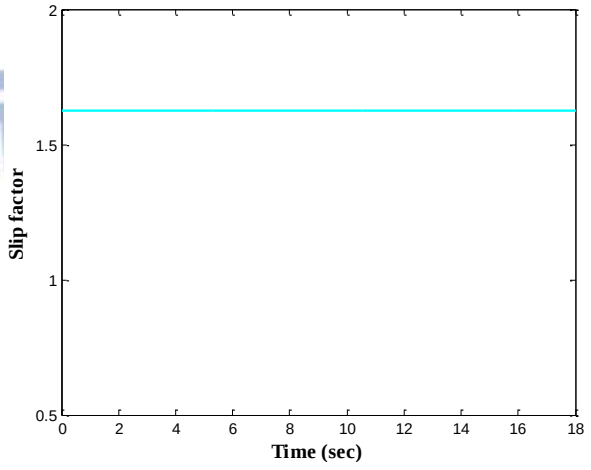

(l) γ with i_{s4}^{*}

Fig. 4-15 Experimental results of control schemes without the switching strategy

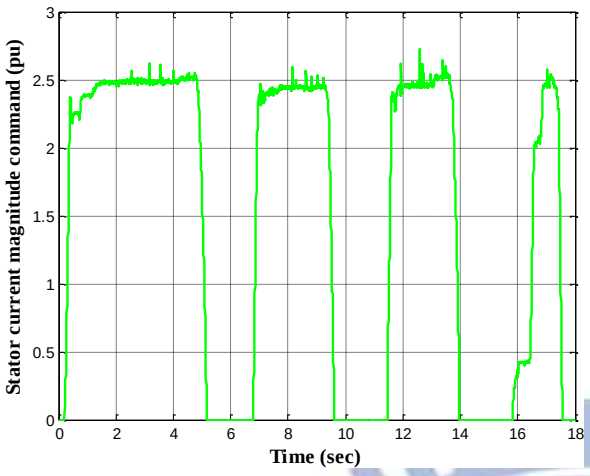

(a) i_{s5}^{*}

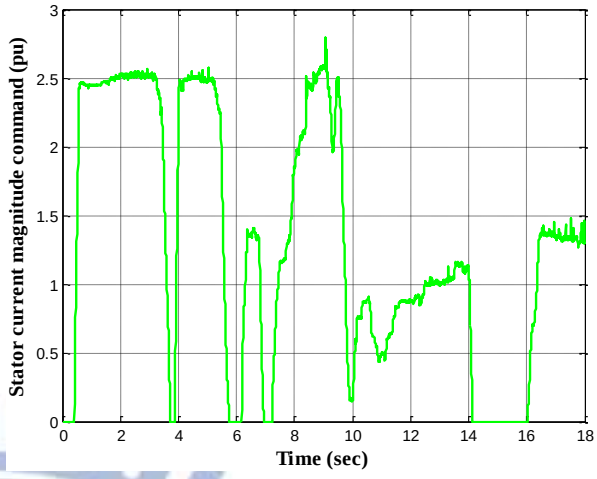

(b) i_{s6}^{*}

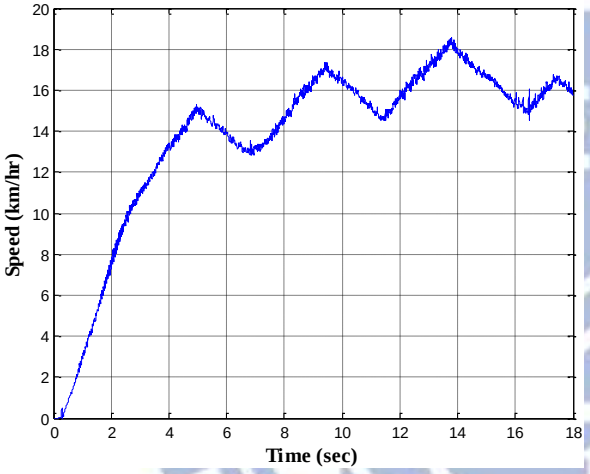

(c) Speed response with i_{s5}^{*}

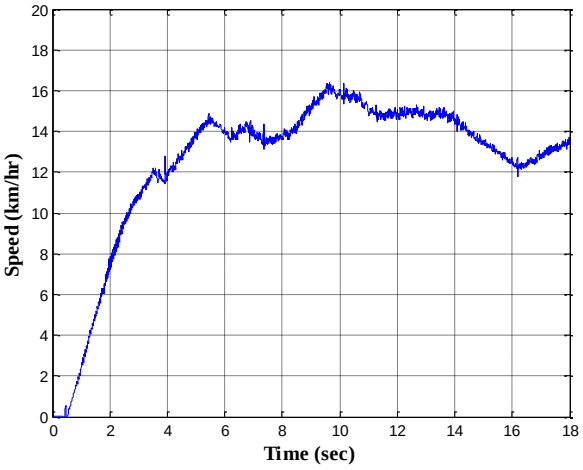

(d) Speed response with i_{s6}^{*}

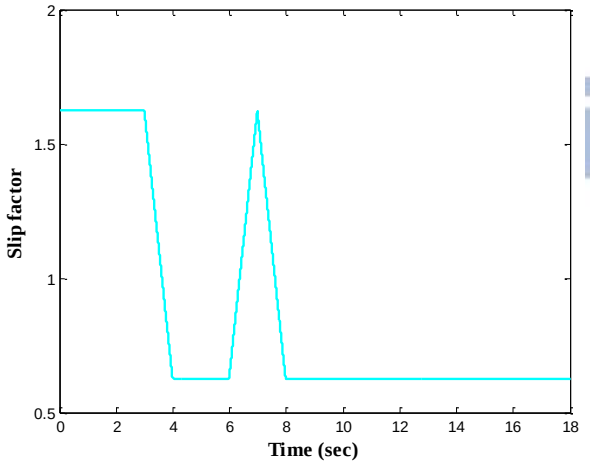

(e) γ with i_{s5}^{*}

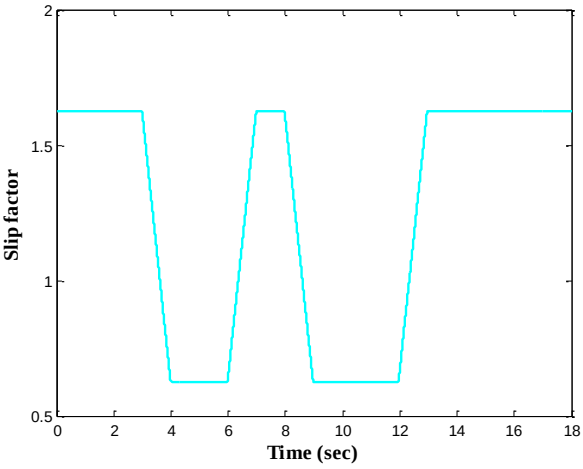

(f) γ with i_{s6}^{*}

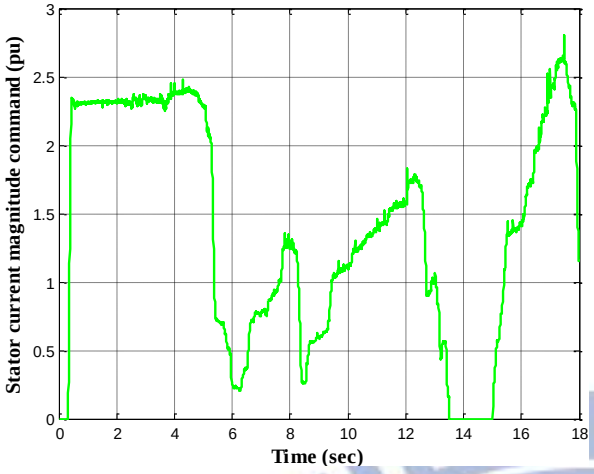

(g) i_{s7}^{*}

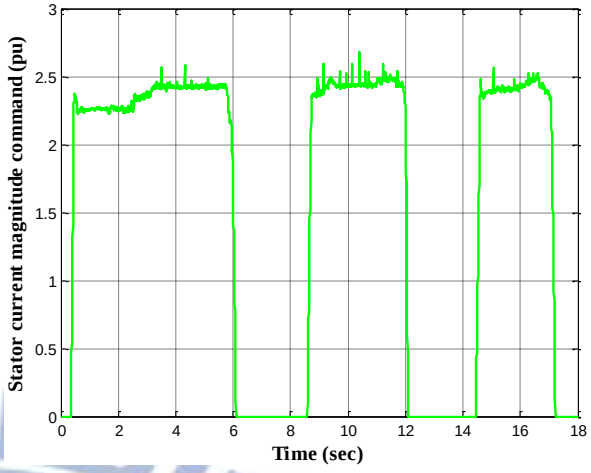

(h) i_{s8}^{*}

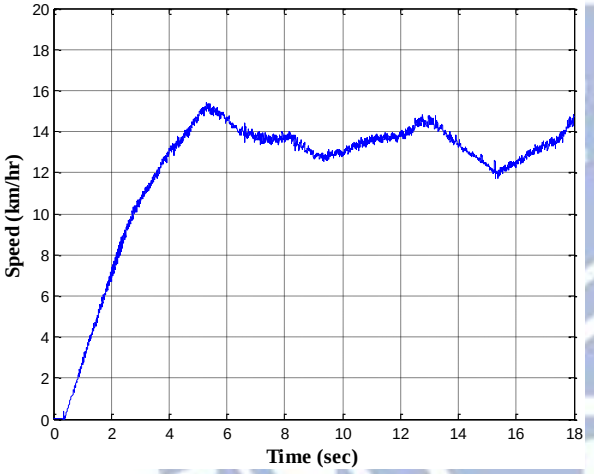

(i) Speed response with i_{s7}^{*}

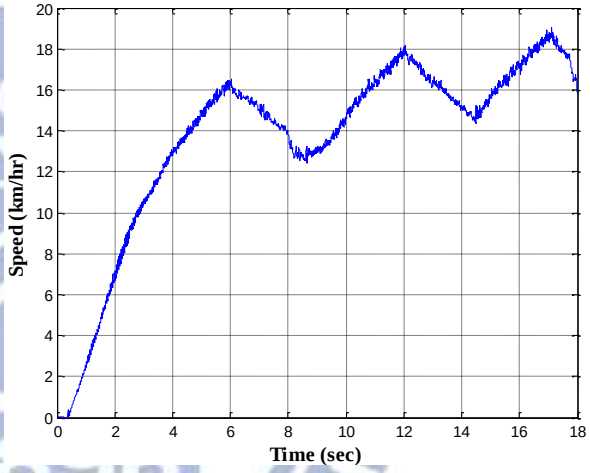

(j) Speed response with i_{s8}^{*}

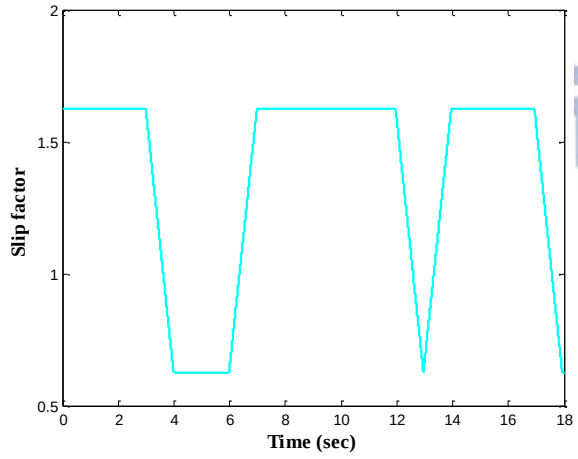

(k) γ with i_{s7}^{*}

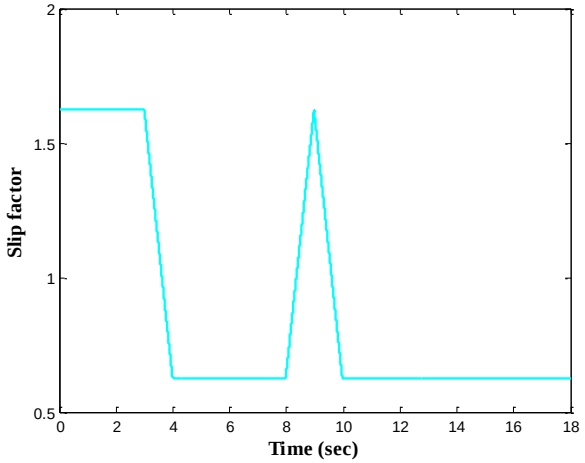

(l) γ with i_{s8}^{*}

Fig. 4-16 Experimental results of control schemes with the switching strategy

After the switching strategy is added to the control scheme, γ can be automatically adjusted as shown in Fig.4-16(e), (f), (k), and (l) according to the driving conditions such as the vehicle speed and the stator current magnitude command controlled by the accelerator in order to obtain both the MTPA and the HE operations. Also, the vehicle speed is no longer restricted to 14.7 km/hr. The highest vehicle speed that can be obtained with the switching strategy is 21.6 km/hr as shown in Table 4-4.

In Chaper 3, we have already verified that the approach of equal *d-q* current command is not suitable for the real vehicle application, since the desirable MTPA operation is lost due to severe flux saturation. When the electric vehicle is driven along the 75-m straight path fed by the maximum stator current 2.576 pu, we notice that the operation with the switching strategy is the best among three operations as shown in Fig. 4-17. It can also be recognized from Table 4-5 that vehicle performance is signicantly improved by the desgined switching strategy.

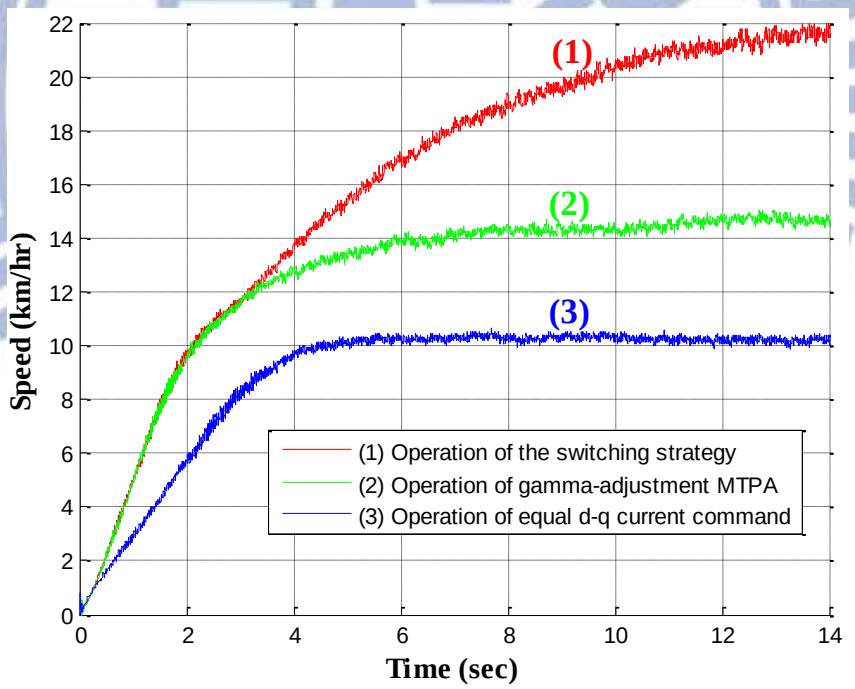

Fig. 4-17 Speed responses obtained with different control strategies

Table 4-5 Summary of performance obtained by different approaches

Operation	Acceleration (rad/s^2)	Efficiency coefficient (rad/s.A)	Final speed (km/hr)	Finish time of 75-m moving (s)
Equal *d-q* current command	23.51	13.35	10.2	25
γ-adjustment MTPA	39.27	38.11	14.7	18
Switching strategy	**39.27**	**49.88**	**21.6**	**15**
Improvement	67%	273.6%	111.8%	40%

To prove that the MTPA obtained by the proposed γ-adjustment and the switching strategy is better than the operation of the equal *d-q* current command, we also have performed an experiment on an inclined road locating at the campus for testing the capability of uphill climbing, where the system was fed by the maximum stator current as shown in Fig. 4-18.

It is obvious that the operation of the equal *d-q* current command cannot produce adequate torque to overcome the rolling resistance so that the vehicle gets stuck on the way and fails to climb the inclined road as seen from the experimental results shown in Fig. 4-19. On the other hand, the operation of the switching strategy does provide sufficiently large torque for uphill climbing, and the vehicle can steadily climb the road with around 10 km/hr. Note that γ is not switched to 0.625 since the condition for the switching where the speed is larger than 10 km/hr is not satisfied.

(a) in front of the vehicle (b) behind the vehicle

Fig. 4-18 View of the inclined road for testing uphill climbing ability

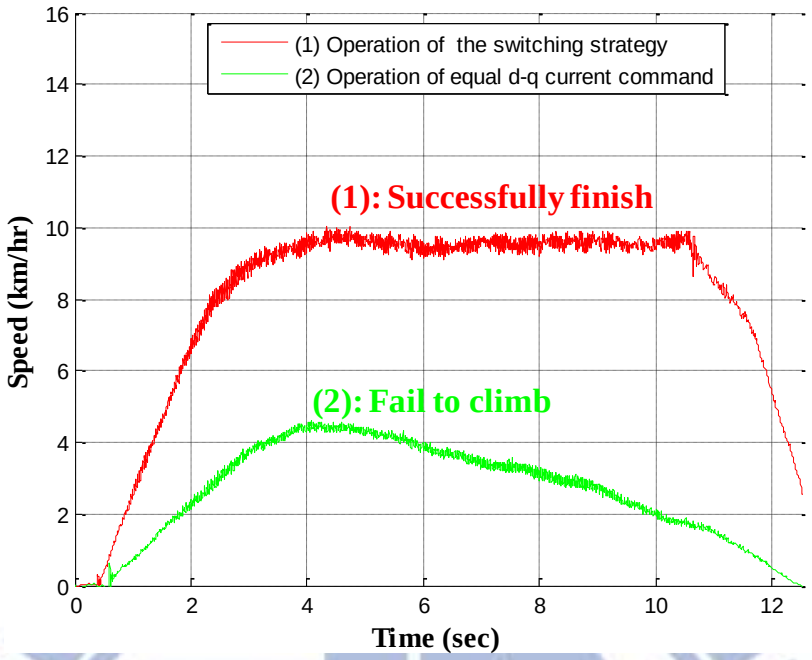

Fig. 4-19 Experimental results of the uphill climbing test

4.4 Summary

In this chapter, the development of a switching control strategy designed for obtaining both the maxmium torque and the highest efficiency operation of the electric vehicle is presented. Some important results are reviewed as follows.

(1) The γ-adjustment control approach that is proposed for a smooth driving characteritic possesses the following two merits:

- The maximum torque per amperage (MTPA) and the highest efficiency (HE) operation can still be obtained by properly setting γ even though i_{ds}^* is set as 0.62 pu which is not at both optimal operating points as 0.82 pu for the MTPA and 0.42 pu for the HE:

Operation	Slip factor setting
MTPA	$\gamma = 1.625$
HE	$\gamma = 0.625$

- It provides smoother operating performance than the i_{ds}^*-adjustment when the switching machanism is applied so that it is more suitable to traction control of the electric vehicle

(2) Switching strategy which can be automatically adjusted according to the driving conditions is properly designed with significant improvement on both developed torque and operating efficiency as follows:

- When the vehicle is driven along the 75-m straight path fed by the maximum stator current, all the acceleration, efficiency coefficient, and final speed can respectively be improved by 67%, 273.6%, and 111.8% if the switching strategy is applied compared with the operation of equal *d*-*q* current command. Finish time of 75-m moving can also be shortened from 25 seconds to 15 seconds.
- When the vehicle is driven along the inclined road fed by the maximum stator current, it can successfully climb the road with 10 km/hr if the switching strategy is applied while the operation of equal *d*-*q* current command is not able to provide sufficient torque for uphill climbing.

Chapter 5

Conclusion

In this research work, the high performance servo traction control of the 0.75-kW IM has been successfully implemented on the TMS320F28335 DSP micro-controller, and it is further improved by the designed automatic switching control strategy to obtain both the maxmium torque and the highest efficiency operation to provide satisfactory performance of the electric vehicle.

Accomplishments and contributions of this Thesis are summarized as follows.

1. High performance servo control of the IM is realized for the traction application

   (1) The rotor time constant of the IM is precisely identified

   An acceleration-based identification process which can be directly performed on the vehicle with reasonable accuracy is developed to obtain the rotor time constant. The identified result is 0.08s, which is close to its nominal value 0.074s.

   (2) The maximum torque per amperage (MTPA) operation is obtained by the rated flux excitation

   The conventional approach of equal *d-q* current command is verified unreliable for the vehicle application in this study, since the desirable MTPA operation is lost owing to severe flux saturation of the IM. By the standard experimental process, it can be proved that MTPA operation can be obtained when the rotor flux linkage is exited at the rated value. With such arrangement, all the acceleration, efficiency coefficient, and the final vehicle speed can be improved by 65.5%, 173.2%, and 44.1%, respectively, when the maximum stator current is applied.

   (3) The highest efficiency (HE) operation is obtained by setting proper flux current

   In spite of the maximum torque produced with the MTPA operation, its operating efficiency and vehicle speed are quite limited. Therefore, the HE operation is found by the standard experimental process for the improvement of the efficiency and the vehicle speed obtained by the MTPA

operation. The former one is improved by 32.7% while the latter one is increased by 45.6%, but the price is the degraded acceleration performance obtained.

2. A switching control strategy which can be automatically adjusted based on the driving conditions is designed to obtain both the maximum acceleration and the highest operating efficiency of the electric vehicle.

A novel control method called the γ-adjustment control is developed for a smooth driving characteritic. Its merits are described as follows.

- The MTPA and HE operation can still be obtained by properly setting γ even though i_{ds}^{*} is originally not set at both optimal operating points as 0.82 pu for the MTPA and 0.42 pu for the HE.
- It provides smoother operating performance when the switching machanism is applied, and thus it becomes more reliable in traction control of the electric vehicle. Then, a switching strategy with which the MTPA operation is applied at a low speed for the maximum acceleration while the HE operation is applied at a high speed for improved operating efficiency and vehicle speed is designed based on the γ-adjustment.

Two experimetal testings have been applied to verify validity of the present control strategy to indicate the following improvements.

- The first experiment is performed for testing vehicle performance with the maximum supplied stator current along a 75-m straight path. When the switching strategy is applied, all the acceleration, efficiency coefficient, and final speed can respectively be improved by 67%, 273.6%, and 111.8%, compared with the operation obtained by the equal *d-q* current command. The time of 75-m driving can also be shortened from 25 seconds to 15 seconds.
- The second experiment is launched for testing vehicle performance with the maximum supplied stator current along an inclined road. Results show that it can steadily climb the road with 10 km/hr if the switching strategy is applied while the operation of equal *d-q* current command is not able to provide sufficient torque for uphill climbing.

References

[1] C. C. Chan, "The State of the Art of Electric, Hybrid, and Fuel Cell Vehicles," *Proc. of the IEEE*, Vol. 95, No. 4, pp. 704–718, 2007.

[2] M. Ehsani, K. M. Rahman, and H. A. Toliyat, "Propulsion System Design of Electric and Hybrid Vehicles," *IEEE Trans. Industrial Electronics*, Vol. 44, No. 1, pp. 19–27, 1997.

[3] A. Emadi, Y. J. Lee, and K. Rajashekara, "Power Electronics and Motor Drives in Electric, Hybrid Electric, and Plug-In Hybrid Electric Vehicles," *IEEE Trans. Industrial Electronics*, Vol. 55, No. 6, pp. 2237–2245, 2008.

[4] Z. Q. Zhu and D. Howe, "Electric Machines and Drives for Electric, Hybrid, and Fuel Cell Vehicles," *Proc. of the IEEE*, Vol. 95, No. 4, pp. 746–765, 2007.

[5] M. Finken, M. Felden, and K. Hameyer, "Comparison and design of different electrical machine types regarding their applicability in hybrid electrical vehicles," *Proc. of the international conference on electrical machines*, pp. 1–5, 2008.

[6] W. Xu, J. Zhu, Y. Guo, S. Wang, Y. Wang, and Z. Shi, "Survey on Electrical Machines in Electrical Vehicles," *Proc. of the international conference on Applied Superconductivity and Electromagnetic Devices*, pp. 167–170, 2009.

[7] N. Hashemnia, and B. Asaei "Comparative Study of Using Different Electric Motors in Electric Vehicles," *Proc. of the international conference on electrical machines*, pp. 1–5, 2008.

[8] I. Husain, "*Electric and Hybrid Vehicles: Design Fundamentals.*" Boca Raton, FL: CRC, 2003.

[9] C. C. Chan, "An Overview of Electric Vehicle Technology," *Proc. of the IEEE*, Vol. 81, No.9, pp. 1202–1213, 1993.

[10] S. K. Sul, "*Control of Electric Machine Drive System*," Hoboken, N.J.: Wiley-IEEE, 2011.

[11] B. K. Bose, "*Power Electronics and Motor Drives: Advances and Trends*," Amsterdam: Elsevier/Academic Press, 2006.

[12] S. J. Chapman, "*Electric Machinery and Power System Fundamentals*," Boston: Mcgraw-Hill, 2002.

[13] O. Wasynczuk, S. D. Sudhoff, K. A. Corzine, J. L. Tichenor, P. C. Krause, I. G. Hansen, and L. M. Taylor, "A Maximum Torque per Amperage Control Strategy for Induction Motor Drives," *IEEE Trans.Energy Conversion*, Vol. 13, No. 2, pp. 163-169, 1998.

[14] J. B. Wang and C. M. Liaw, “Indirect field-oriented induction motor drive with fuzzy detuning correction and efficiency optimisation controls,” *IEE Proc.-Electr. Power Appl.*, Vol. 144, No. 1, pp. 37-45, 1997.

[15] K. H. Nam, *AC Motor Control and Electric Vehicle Applications*, New York: CRC, 2010.

[16] C. Chakraborty and Y. Hori, “Fast Efficiency Optimization Techniques for the Indirect Vector-Controlled Induction Motor Drives,” *IEEE Trans. Industry Applications*, Vol. 39, No. 4, pp. 1070-1076, 2003.

[17] H. Rehman, L. Xu, "Alternative Energy Vehicles Drive System: Control, Flux and Torque Estimation, and Efficieny Optimization," *IEEE Trans. Vehicular Technology*, Vol. 60, No. 8, pp. 3625-3634, 2011.

[18] “TMS320F28335, TMS320F28334, TMS320F28332, TMS320F28235, TMS320F28234, TMS320F28232 Digital Signal Controllers (DSCs) Data Manual,” *Texas Instruments*, 2010.

[19] “TMS320x2833x, 2823x Enhanced Pulse Width Modulator (ePWM) Module Reference Guide,” *Texas Instruments*, 2009.

[20] “TMS320x2833x, 2823x Analog-to-Digital Converter (ADC) Module Reference Guide,” *Texas Instruments*, 2007.

[21] “TMS320x2833x, 2823x Enhanced Quadrature Encoder Pulse (eQEP) Module Reference Guide,” *Texas Instruments*, 2008.

[22] 黃樑傑, “環保節能車關鍵車電展分析,” *財團法人車輛研究測試中心*, 中華民國 100 年.

[23] 張鴻喜, “我國輕型電動車輛產業發展現況與趨勢,” *馬達科技研究中心*, *Motor Express*, 第八十七期, 中華民國93年.

[24] 侯貫智, “稀土金屬,” *金屬中心*, 金屬材料月報, 中華民國 100 年.

[25] 薛乃綺, 侯貫智, “開發不使用稀土材料的馬達日益重要,” *金屬中心*, 中華民國 100 年.

[26] R. Krishnan and F. C. Doran, “Study of Parameter Sensitivity in High-Performance Inverter-Fed Induction Motor Drive Systems,” *IEEE Trans. Industry Applications*, Vol. IA-23, No. 4, pp. 623-635, 1987.

[27] R. Krishnan, A. S. Bharadwaj, "A Review of Parameter Sensitivity and Adaption in Indirect Vector Controlled Induction Motor Drive Systems," *IEEE Trans. Power Electronics*, Vol.6, No.4, pp. 695-703, 1991.

[28] 葉釗甫, “CNC 剛性攻牙製程之先進運動控制器設計,” *國立交通大學*, 碩士論文, 中華民國 100 年.